Black Hole Exhaust and Ventilation in Galaxies, Groups, and Clusters: Interaction of AGN Jets with the Environments

By

Yi-Hao Chen

A dissertation submitted in partial fulfillment of

the requirements for the degree of

Doctor of Philosophy

(Astronomy)

at the

UNIVERSITY OF WISCONSIN–MADISON

2019

Date of final oral examination: August 23, 2019

The dissertation is approved by the following members of the Final Oral Committee:
Sebastian Heinz, Professor, Astronomy
Keith Bechtol, Assistant Professor, Physics
Rich Townsend, Associate Professor, Astronomy
Eric Wilcots, Professor, Astronomy

Abstract

The purpose of this work is to use numerical tools to study extragalactic jets and their interaction with the gas in their host galaxies, galaxy groups, and galaxy clusters.

I present a series of three-dimensional magneto-hydrodynamic simulations to model active galactic nuclei (AGN) jets. To follow the evolution of the synchrotron emitting plasma, I implement a framework based on tracer particles to track the cooling of relativistic particles. I discuss how different topology of magnetic fields in the jets affects the propagation of jets and the morphology of radio lobes. Synthesized radio maps are presented and discussed. Derived from the results of the simulation, a potential observational signature of the reversal of spectral index gradient might be visible after the jet turns off and the bubble buoyantly rises.

Furthermore, I extend the simulation to different jet powers and environments and show how the environment influences the radio morphology and spectral index. The relation between the jet power and the radio luminosity from the simulations is compared with data from observations. Additionally, the dependence of this relationship on the environment and time is discussed.

Finally, I introduce a new heating mechanism in the context of the cooling flow problem in galaxy clusters. The long-term evolution of the jet-inflated bubble drives the uplift of a significant amount of low-entropy gas to large radii. For reasonable assumptions about the thermal conduction rate, the substantial heat exchange between the uplifted

gas and the hot cluster gas implies that the AGN may act like a geothermal *heat pump* to facilitate an additional channel of heating. The maximum efficiency and potential additional energy gain of this mechanism are discussed. In this scenario, the AGN could heat the inner cluster more than its total energy allows and in a much gentle and enduring way than impulsive models of heat injection.

Acknowledgments

I am indebted to my advisor Sebastian Heinz for the mentorship and support during my time in Madison and throughout numerous challenges in the research projects. Thank you for always having faith in me. Your tireless spirit and enthusiasm offered a great role model as a passionate scientist. I am grateful to have DooSoo Yoon in our group, who kindly guided me in the early stage of my research. Special thanks to Gandhari Wattal for the various discussions and initiatives all the time.

I am thankful to Marsha Wolf, Eric Hooper, and Eric Wilcots, whose feedback greatly improved my work. I am particularly grateful to Andrea Vang, with whom I have been working together on the radio project and having helpful discussions.

I feel very privileged that I could spend my time in Madison working with passionate, smart, and kindhearted people. To all faculty members, thank you for the teaching, leading, and caring through my graduate study. To staff of the Astronomy Department, thank you for solving my many administrative and technical problems. Particular thanks go to fellow graduate students, who made this department especially welcoming and supportive.

I am obliged to my parents for their continuous support, even from thousands of miles away. And lastly, I owe my deepest gratitude to my love, Wan-Jun Lu, who unconditionally supports and encourages me through all the ups and downs in our journey. I would not be able to complete the work without you.

Contents

List of Tables

List of Figures

Chapter 1

Introduction

1.1 A Brief History of AGN

It has been less than 100 years since humanity realized that the Milky Way is merely one of many many galaxies in the universe. In 1925, less than five years after the "Great Debate" between Shapley & Curtis (1921) (see also Trimble 1995, for a modern review), Hubble (1925) published the distance to the "spiral nebulae," M31 and M33, based on the luminosity-period relation of Cepheid variables discovered by Leavitt (1908) and Leavitt & Pickering (1912). The derived distance, 285,000 parsecs[1], settled the issue of *island universes*.[2] We now know that the universe is full of galaxies.

Ever since the initial studies of those "spiral nebulae", it had been noticed that emission lines co-exist with the stellar-like absorption lines in them (Slipher 1917; Hubble 1926). Seyfert (1943) collected a sample of 6 galaxies with high-excitation nuclear emission lines. However, the nature of these objects was not investigated until Burbidge et al. (1959), who interpreted the broad emission feature as a result of gas being ejected from the nuclei of the galaxies.

On the other hand, the *invisible* universe in radio wavelengths began to reveal itself after communication radio antennae were turned to the sky. After Jansky (1933) realized that there was radio emission coming from outside of our solar system, Reber (1942) measured the radio sky at 160 MHz and found several local maxima, including one in

[1]The distance to M31 measured by Hubble is a factor of 3 smaller than recent measurements (e.g. McConnachie et al. 2005).

[2]The original paper, which was as read on January 1, 1925, during the American Astronomical Society Meeting at Washington, DC., appeared to be lost (Berendzen & Hoskin 1971). A peer-reviewed paper was published in 1929 (Hubble 1929).

Cygnus which would later prove important in radio AGN studies. Bolton & Stanley (1948) later used an interferometer to suggest the source in Cygnus is discrete (size less than 8') and it is unlikely to originate from thermal radiation. Jennison & Das Gupta (1953) identified two regions of radio emission in the Cygnus radio source. However, they found that the optical object does not overlap with the two components but sits in the middle. The misalignment between optical and radio sources had caused considerable confusion about whether the optical galaxy and the radio emission have any direct correlation.

In the years after, various types of extragalactic objects were discovered, including BL Lac objects, blazers, flat-spectrum radio quasars (FSRQ), steep-spectrum radio quasars (SSRQ), Fanaroff-Riley I/II radio sources, broad/narrow lines galaxies, quasi-stellar objects (QSOs), optically violently variable quasars (OVVs), low ionization nuclear emission region (LINER), among others. Those objects with strong nuclear activities were collectively called active galactic nuclei (AGNs). The diversity of the objects posed a great mystery for AGNs, and various attempts were made to explain that the different types are caused by viewing orientations, rather than intrinsic properties, as shown by the schematic illustration in Fig. 1.1.

A key element in these unification models is the bipolar jets that are escaping at a relativistic speed perpendicular to the accretion disk around the central compact object. The orientation relative to the observer determines the visibility of different components. Extended radio galaxies, especially those with double lobes, are fully visible jets when they are perpendicular to the line of sight. On the other hand, jets are not easily distinguishable when they are seen head-on. However, in this case, their radiation is relativistically Doppler boosted in frequency and luminosity as in blazars (Antonucci 1993; Urry & Padovani 1995; Ferrari 1998). A review on the history of AGN can be found in Shields (1999), and a comprehensive introduction of the subject can be found in the book by Beckmann & Shrader

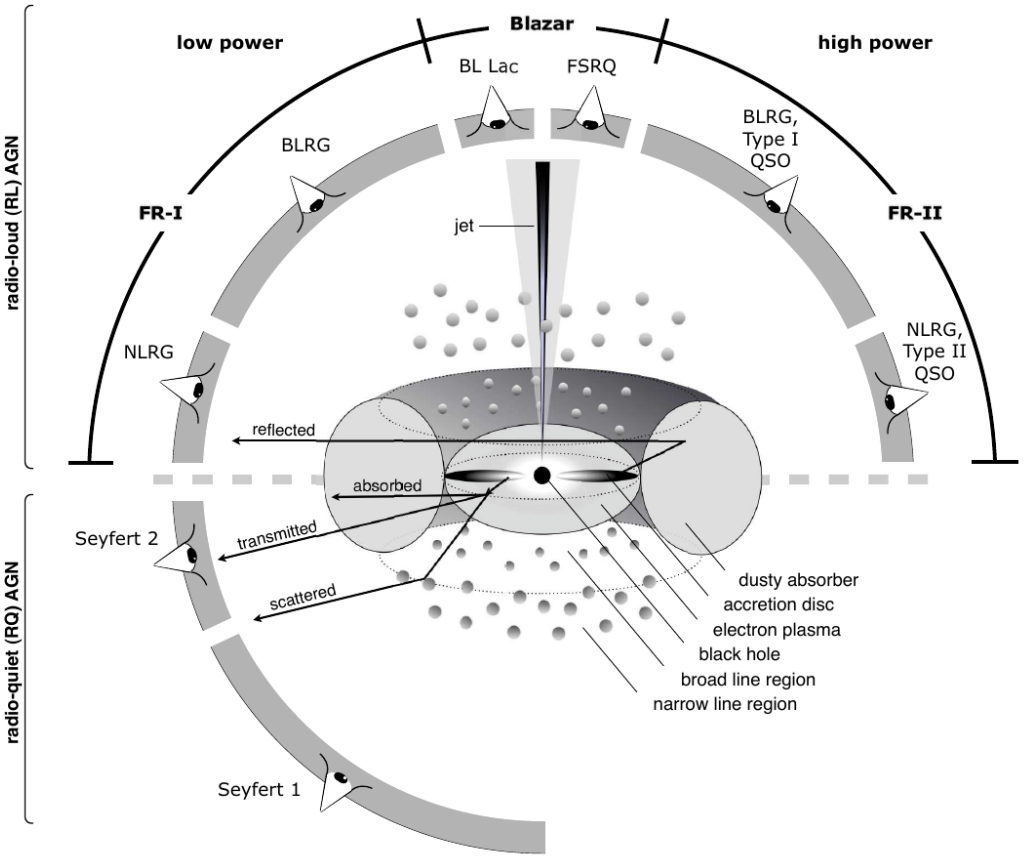

Figure 1.1 : The canonical understanding of AGN phenomena in the unified scheme. The type of objects we observe depends on the orientation of our viewing angle. Graphic by Marie-Luise Menzel in Beckmann & Shrader (2012).

(2012).

The initial classification of radio-loud and radio-quiet AGNs has been challenged by more sensitive observations that showed radio emission might be present in all cases (White et al. 2000; Cirasuolo et al. 2003), and whether there is *dichotomy* of radio loudness has been up for debate. The bimodality might depend on how the samples are selected and whether only the core luminosity or the total radio emission are used.

1.2 Astrophysical Jets

Only a year after the (at the time) large redshift (z=0.158) of 3C 273 was revealed by Schmidt (1963), the idea of energy production by accretion onto a black hole was advanced (Salpeter 1964; Hoyle et al. 1964). The accretion can release the gravitational energy of the infalling material at a much higher efficiency than ordinary stellar nuclear fusion. Highly collimated streams of plasma were quickly used to explain various features of radio AGN (Scheuer 1974; Blandford & Konigl 1979; Begelman et al. 1984). Those jets are thought to be launched from the central compact object or the accretion disk. Now we have observed astrophysical jets at vastly different scales, from protostars, X-ray binaries to active galactic nuclei.

In the case of AGN jets, they are composed of a relativistic stream of particles that are powered by supermassive black holes at galactic nuclei (see Blandford et al. 2018, for a recent review). The composition of the jets is still under debate and might vary across different types of objects (Croston et al. 2018). We know there must be leptons in the jets since radio sources are emitting synchrotron radiation from electrons or positions spiraling around magnetic fields (Reynolds et al. 1996), but see also The IceCube Collaboration et al. (2018), detection of high-energy neutrinos from blazar that must be produced by high energy protons.

Jets are considered an important mechanism to extract energy from the central objects and transfer angular momentum outward. The removal of angular momentum is vital for accretion to take place, and magnetic fields play an important role in these processes (Hawley et al. 2015). I will discuss how magnetic fields in the jets could affect the propagation of jets and the large-scale radio lobes in Chapter 2.

Jets are thought to be launched by extracting the rotational energy from the black

hole (Blandford & Znajek 1977, hereafter BZ) or the accretion disk (Blandford & Payne 1982) through the threading of magnetic fields into the event horizon or the disk. The jet power of the BZ mechanism depends on the magnetic flux and spin of the black hole, which both remain largely unknown. Large-scale poloidal fields, which could be advected by the accretion flow from larger radius (Beckwith et al. 2009) or generated through a dynamo around the compact object (Tout & Pringle 1996; Bugli et al. 2014), are necessary to accelerate the jets. It is thought that around the vicinity of the black hole, the flow could be dominated by Poynting flux (Li et al. 2006; Guan et al. 2014; Tchekhovskoy 2015), which means the magnetic energy density is much larger than kinetic and thermal energy. If the magnetic energy is transferred to the matter within the jets, the matter can be accelerated to highly relativistic velocity through a large range of scales (Lyubarsky & Yuri 2009). Collimation could come from the magnetohydrodynamical structure of the jets (Nakamura et al. 2007; McKinney & Blandford 2009) or from external pressure such as disk winds (Porth & Fendt 2010).

In this thesis, I focus on the interaction of the jets with ambient gas on scales much larger than the acceleration zone, assuming most of the magnetic energy has been converted to kinetic energy at the boundaries of our injection nozzle roughly about 100 pc from the black hole. Indeed, Sikora et al. (2005) argue that, from observational data, the conversion of Poynting flux to kinetic energy happens mostly within 10^3 gravitational radii at parsec scale, which is consistent with our assumptions. Although the energy flux is dominated by the kinetic energy in our simulations, magnetic fields are still dynamically important at larger scales.

1.3 Impact of AGN Jets on Their Environments

The active galactic nuclei and the jets were initially viewed as exotic events in the universe and were studied as a high-energy laboratory to probe the particle acceleration, radiation, and accretion (see Shields 1999, for a historical review). Most of the discussion focused on the AGNs themselves, or occasionally on how the environment affects the AGN. Although the correlation between star formation and AGN activity have long been suggested (Sanders et al. 1988), it was not until the 1990s that *feedback* from AGN started to come into focus. Among the first were Ciotti & Ostriker (1997); Silk & Rees (1998); Fabian (1999), who considered how strong radiation and winds could affect the host galaxies, particularly the most massive galaxies residing at the center of galaxy clusters. The relationship between X-rays in massive cooling flow galaxies and the radio emission have long been investigated and hinted that AGN jets might be energetic enough to counteract cooling flow (e.g. Burns 1990; Pedlar et al. 1990; Baum & O'Dea 1991).

1.3.1 Cooling Flow Problem in Galaxy Clusters

The cores of galaxy clusters often exhibit strong X-ray emission, which should lead to strong radiative cooling and the formation of a *cooling flow* (Fabian 1994). The lack of such flows in observations motivates the study of feedback processes that could counteract the cooling. Mechanical energy deposited by the jets could be one of the important mechanisms in galaxy clusters (McNamara & Nulsen 2012). X-ray observations of galaxy clusters often show radio-emission-filled cavities that are inflated by jets from the supermassive black holes in the central galaxy (see e.g. Bîrzan et al. 2004, 2008). In some cases, multiple cavities caused by episodic jet activities are observed. The most detailed observation of this kind is of the Perseus Galaxy Cluster (Fabian et al. 2000, 2003, 2006, 2011), in which a pair of X-ray cavities are distinctly visible in the core. Another pair of "ghost" cavities

with much weaker radio emission is also observed, as shown in Fig. 1.2.. It is worth noting that, despite showing vibrant jet activity, recent X-ray spectral observations show that the atmosphere of the Perseus Cluster is surprisingly quiescent and agrees with the hydrostatic equilibrium assumption (Aharonian et al. 2016).

In Chapter 2 and 4, I tune the background profile in the simulation to mimic the conditions in Perseus Cluster. A thorough investigation of the interaction between jets and the cluster medium could help us understand the dynamics of galaxy clusters' baryonic content which dominates in the central regions. I will discuss a new heating mechanism by AGN jets in the context of the cooling flow problem in Chapter 4, in which additional energy might be drawn from the hot cluster atmosphere.

1.3.2 Coevolution of Supermassive Black Holes and Host Galaxies

A full review of the evolution of galaxies is beyond the scope of this introduction. However, it is noted by Heckman & Best (2014) that the studies of galaxies and active galactic nuclei (AGNs) remained mostly disconnected for the past five decades. AGNs were studied primarily in the context of the theory of relativity and exotic high-energy processes.

The vastly different scale of the black hole and the galaxy can likely explain some of the disconnection. The radius of the sphere of influence around a supermassive black hole (SMBH) can be calculated by

$$r = \frac{GM_{\rm BH}}{\sigma^2} \tag{1.1}$$

where $M_{\rm BH}$ is the mass of the black hole, σ is the stellar velocity dispersion of the host bulge, and G is the gravitational constant. This is the radius within which the gravitational potential of the black hole dominates the gravitational potential of the host galaxy. For a $10^9 M_\odot$ black hole, and 300 km/s velocity dispersion, the radius is about 48 pc. Comparing

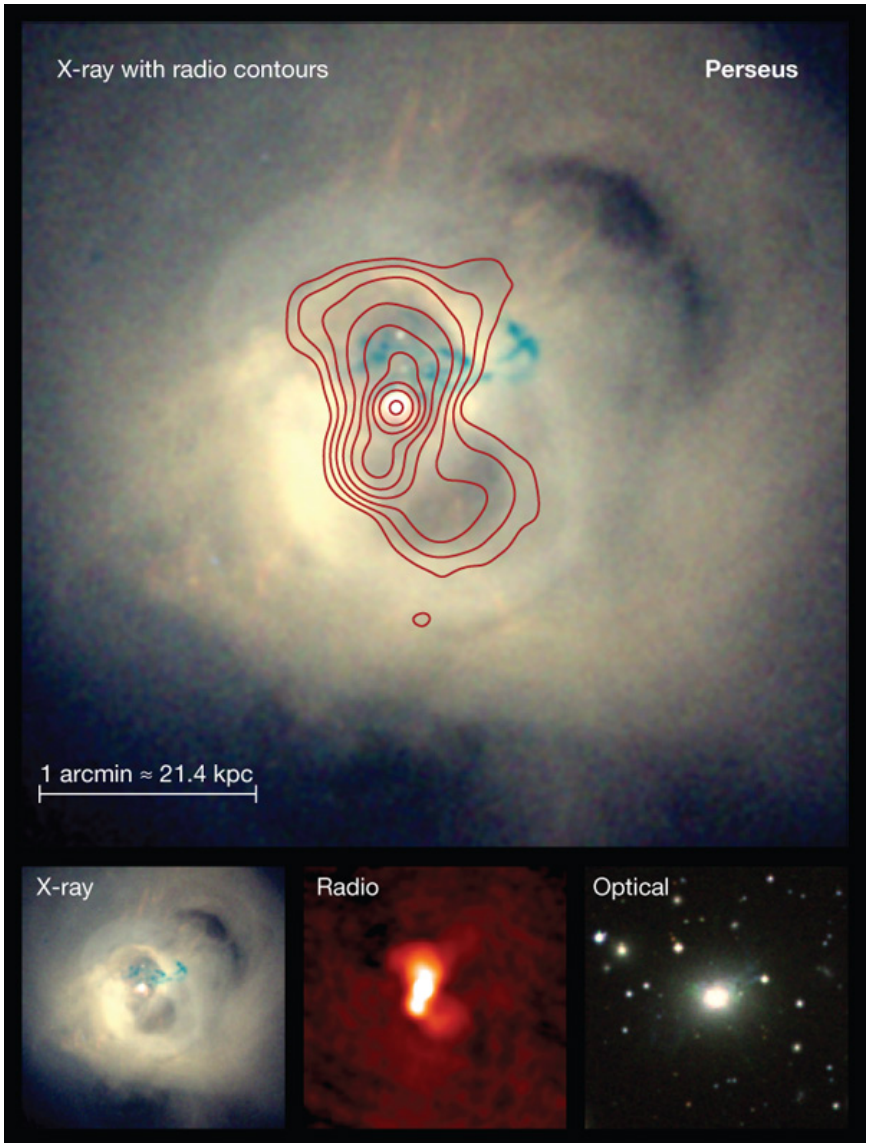

Figure 1.2 : The composite image of the central region of the Perseus cluster. X-ray cavities coincide with radio emission indicate the lobes of relativistic synchrotron plasma injected by the jets. The image is from Cattaneo et al. (2009), which is derived from Fabian et al. (2006).

that to the few kpc sizes of the bulge and the host galaxy, it is no wonder that the interaction between the SMBHs and the galaxies are not immediately obvious.

The realization of the tight correlation between the mass of BH and the velocity dispersion by (Ferrarese & Merritt 2000; Gebhardt et al. 2000) provided greater confidence that the two must evolve together or must be coupled through some interactions.

Bower et al. (2006); Croton et al. (2006) proposed an AGN *feedback* model to quench star formation by maintaining hot gas halos in massive galaxies, in contrast to the supernova or starburst feedback in less massive galaxies.

Two mechanisms are often invoked to couple the energy from the AGN to the host galaxies: radiative, or sometimes referred to quasar-mode, and mechanical, or radio-mode Fabian (2012). The accretion disks formed around the SMBH naturally release a large amount of energy in the form of radiation or winds (King & Pounds 2014). The jets, launched by the magnetic fields threading the black hole or the accretion disk, provide directional mechanical energy. How this pointed energy release has an impact on the host galaxy has long been a question of many researchers. The purpose of this work is to explore how the environments affect AGN jets as well as how AGN jets change the environments.

1.4 Numerical Simulations of Jets and Recent Works

Due to the highly non-linear physics, analytic works are limited to one-dimensional or axisymmetric two-dimensional solutions in steady-state (see Ferrari 1998, for a review). Many of the works focused on the acceleration of jets from disks and magnetospheres around black holes. Numerical works are thus necessary to investigate the time-dependent three-dimensional analysis and perform experiments.

1.4.1 Numerical Methods

Hydrodynamic simulations usually involve one of two popular methods: Lagrangian smoothed particle hydrodynamics (SPH, e.g. Springel 2005), or Eulerian decomposition of spatial domains (grid). The latter could be either fixed mesh (e.g. Stone et al. 1992) or adaptive mesh refinement (AMR, e.g. Fryxell et al. 2000; Dubey et al. 2009; Bryan et al. 2014), in which new sub-cells are created or destroyed on demand during the simulation.

A remarkable effort was made to compare the difference between the two methods (e.g. O'Shea et al. 2005; Agertz et al. 2007; Kim et al. 2016). I will briefly describe the advantage and drawbacks of each and motivate the choice of AMR code in this work.

In SPH methods, Lagrangian mass elements are followed with a kernel to smooth their spatial distribution. This approach works easily with N-body gravitational simulations and is often used in cosmological and galaxy evolution. The main problem of SPH is the smoothing, which suppresses instabilities and erases shocks and discontinuities.

On the other hand, the grid-based methods discretize volume into cells. They are well developed and well tested in computational fluid dynamics for decades. The discontinuous nature of the methods provides good shock capture, which is essential in the jet simulations. However, the fluid moving across surfaces has large advection errors and generates excessive mixing. The angular momentum is not conserved in the grid-based methods, but this is not a concern in this work. In AMR, the refinement boundaries cause effectively lower accuracy and could induce spurious effects along the boundaries. The refinement criteria in AMR also have a direct impact on the results of the simulations.

The combination of magnetohydrodynamics (MHD) and AMR in 3D poses a significant challenge in code development. Lee (2013) developed a full 3D MHD solver with unsplit staggered mesh scheme (USM). The implementation in FLASH allows us to per-

form high-resolution simulations of magnetized jets with decent accuracy and reasonable computational cost.

It should be noted that new methods were recently proposed and implemented to alleviate the drawbacks of SPH and grid-based methods. Examples of these new approaches include the unstructured moving mesh by Springel (2010) and meshless finite-mass/finite-volume by Hopkins (2015). Although they are promising in solving existing problems in traditional methods, each still comes with its own limitations and issues.

1.4.2 Early Simulations of Jets

Norman et al. (1982) began numerical experiments to understand supersonic jets in two dimensions and investigated the instabilities during the propagation, setting the stage for jet simulations. Marti et al. (1994) conducted 2d relativistic hydrodynamic simulations of jets and found them to be more stable compared to Newtonian simulations. With the increasing power of supercomputers, 3D simulations in uniform grids became within reach in the 1990s (e.g. Cox et al. 1991; Marti et al. 1997; Bodo et al. 1998). In the 2000s, magnetic fields came into focus in the jet simulations (e.g. Li et al. 2006; Nakamura et al. 2006).

The physical launching radius of the jets is a few gravitational radii ($r_g = 2GM/c^2 = 10^{-4}$ pc for a $10^9 M_\odot$ black hole). The largest radio lobes can, however, extend to several Mpc (J1420-0545 and 3C 236, Machalski et al. 2008; Tremblay et al. 2010). It is currently impossible to simulate the formation of jets and the lobes together, which span over 10 orders of magnitude in spatial scales. Thus, studies of jets can be categorized into several regimes: (a) jet launching, (b) collimation, and (c) propagation, jet-ambient interaction. I will review relevant works in all three categories, but the works in this thesis focus on simulations that model regimes (b) and (c).

1.4.3 Jet Launching

The radial dynamical ranges of the inflow/outflow simulations are very limited, usually up to 2 orders of magnitude. The limitation comes from both the computational power and the boundary condition effects. Simulation results are usually not reliable close to the boundary, casting doubts on radial profiles of the physical quantities. MHD simulations suffer from this effect even more than hydrodynamic ones, since the Alfvén speed is very large in regions of low density and strong magnetic field. However, since the outflow might rejoin the accretion flow, the radial dynamical range must be large enough for this phenomenon to be observed.

Tchekhovskoy et al. (2011) described a magnetically arrested accretion and studied the outflow to inflow ratio for different spinning parameters (a_*). For slowly spinning black holes ($a_* = 0.5$) the outflow rate is smaller than the accretion rate ($\sim 30\%$), but it is still more efficient than what is found in the previous studies. For rapidly spinning black holes ($a_* = 0.99$)), they found powerful outflows with efficiency greater than 100%. The energy is extracted from the spin energy of the black hole through the BZ mechanism.

Liska et al. (2018) used 3D general relativistic magnetohydrodynamics (GRMHD) simulations to show that precessing jets are formed by a tilted accretion disk rather than the spin of the black hole. This could provide an explanation of rapid changes of the jet direction as seen in observations.

1.4.4 Jet Propagation and Instabilities

Cielo et al. (2014) investigated the interaction of jets with the surrounding interstellar medium in the context of AGN. They focused on the early evolutionary stages of the jets, which are divided into three major phases: (1) cocoon and hot spot formation, (2) forward propagation, and (3) lobe expansion. Energy budget, geometry, thermodynamics, and

backflows of the jet are described in detail in this paper.

Backflows are spatially coherent flows directed opposite to the jet, which were already seen in early simulations (Antonuccio-Delogu & Silk 2008; Rossi et al. 2008; Mizuta et al. 2010). Cielo et al. (2014) observed the damping of the backflows and proposed that the 3D dynamics (large-scale vorticity) is the reason that these backflows stopped, rather than Kelvin-Helmholtz (hydrodynamic) instabilities. They argued that the backflow might be an important positive feedback mechanism of the accretion disk, since the gas is replenished by the backflow. However, no further examination of this feedback is discussed.

Guan et al. (2014) used RMHD simulations to study the current-driven instabilities (CDIs) of Poynting-flux-driven jets. They injected continuous and constant magnetic flux, which has poloidal and dominant toroidal field components. The initial jet velocity of $\sim$0.5c is being accelerated by the magnetic gradient pressure in the z-direction to Lorentz factor $\gamma \sim 3$. The jet stays collimated despite the development of CDIs and subsequent strong dissipation. They suggest that the stability of the jet comes from both the rapid jet propagation and fast evolution of the associated magnetic structure. The CDIs developed in the simulations are convective and do not disrupt the jet. As supported by O'Neill et al. (2012), they found that the development of CDIs is able to convert magnetic energy into kinetic and thermal energy.

Tchekhovskoy & Bromberg (2016) proposed that the magnetic kink instability is key to the Fanaroff-Riley dichotomy of radio jets. They calculated a critical power, below which jets become unstable, based on the profile of the galaxy.

1.4.5 Jet-Environment Interaction

Perucho & Bosch-Ramon (2012) conducted a hydrodynamic study on the interplay between jets from microquasars and the clumpy stellar winds. The winds from the high

mass companion are thought to be clumpy rather than homogeneous. They used 3D relativistic hydrodynamic code to simulate the later stage of the jet interacting with the clumpy winds. They found that clumps entering the jet are compressed and heated during the sound crossing time. The shock wave induced by the entering of the clump propagates inside the jet, disrupting and bending the jet. The mass loading decelerates the jet very efficiently due to the high density of the clumps. Only a moderate wind clumpiness (filling factor $f \sim 0.1$) already makes a substantial difference with the homogeneous case. They didn't give a quantitative description of the observables but argued that the effect could be observationally seen by very long baseline interferometry.

Morsony et al. (2010) performed pure hydrodynamic simulations of well-resolved jets in dynamic atmospheres and randomly reoriented the jet direction, similar to this work, to produce realistic jet and lobe structures. Nakamura et al. (2006) modeled Poynting flux dominated jets that are produced by a strong rotating poloidal magnetic field at their base. Finally, there is a model of MHD jets with weak magnetic fields, which is the one utilized in this thesis. Mendygral et al. (2011, 2012) performed similar 3D non-relativistic MHD simulations of weakly magnetized jets with much higher plasma β than in our studies.

1.4.6 Lobe Size Scaling Relations

The jet injects a large amount of energy into the surroundings, which to lowest order generates the Taylor-Sedov-like blast wave. By simple dimensional analysis, we can get an estimate of the scale length of the bubble similar to the analysis of stellar wind bubble by Castor et al. (1975).

$$P = [ML^2t^{-3}] \tag{1.2}$$

and

$$\rho = [ML^{-3}] \tag{1.3}$$

where P is the power injected by the jet, M is the mass, L is the length, t is the time, and ρ is the density. Eliminating the mass gives the scaling relation of the length

$$L \sim \left(P\rho^{-1}t^3\right)^{1/5} \sim P^{1/5}\rho^{-1/5}t^{3/5} \tag{1.4}$$

and the expansion velocity of the bubble

$$v = \frac{\mathrm{d}L}{\mathrm{d}t} \sim P^{1/5}\rho^{-1/5}t^{-2/5} \tag{1.5}$$

By knowing the power generated by the source and the density of the ambient material, we can estimate the length of the bubble and the expansion velocity as a function of time. In contrast, if we can measure the velocity of the shock (which is usually easier), the density, and the scale of the bubble, we can come to an estimate of the power

$$P \sim L^2 v^3 \rho. \tag{1.6}$$

The scaling relation is used to estimate the lobe size given jet power and the density of the environment in Chapter 3.

1.5 Chapters in this Thesis

This thesis is organized as follows. In Chapter 2, I describe the detailed setup of the simulations, with the implementation of synchrotron cooling tracer particles. I show the results in the first experiment regarding how different configurations of magnetic fields in the jets affect the propagation of jets and the morphology of the much larger radio lobes. I also characterize the synthesized radio emission, including properties of spectral index and polarization. We suggest a potential observational signature of the reversal of spectral index gradient at about one turn-over time of the radio bubble.

A detailed derivation of the electron transport equations, which we used in the synchrotron cooling tracer particles, is included in Appendix A.1. The calculation of synchrotron emissivity and polarization is included in Appendix A.2.

In Chapter 3, I extend the simulation to different jet powers and environments, parameterized by different core radii in the β-model. The impact of the environment on the radio morphology and spectral index are discussed. I show the time- and environment-dependent evolution of radio luminosity in the simulations and compare the jet power-radio power relation with data from observations.

In Chapter 4, I present the long-term evolution of the jet-inflated bubble in the context of the cooling flow problem in galaxy clusters. By considering the thermal conduction between the uplifted low-entropy gas and the hot intra-cluster-medium, we propose a new mechanism, in which the AGN acts like a geothermal *heat pump* to facilitate an additional channel of heating. The maximum efficiency and potential additional energy gain of this mechanism are discussed. We demonstrate that, in this scenario, the AGN could heat the cluster core with more than 100 % of the injected energy and the bursty nature can be transformed into a gentle and enduring heating process. This AGN-induced thermal conduction has the potential to significantly increase the efficiency with which AGN can heat cool-core clusters and transform the bursty AGN activities into a smoother and enduring heating process.

I summarize and conclude the works in Chapter 5.

References

Agertz, O., Moore, B., Stadel, J., et al. 2007, MNRAS, 380, 963

Aharonian, F., Akamatsu, H., Akimoto, F., et al. 2016, Nature, 535, 117

Antonucci, R. 1993, ARAA, 31, 473

Antonuccio-Delogu, V., & Silk, J. 2008, MNRAS, 389, 1750

Baum, S. A., & O'Dea, C. P. 1991, MNRAS, 250, 737

Beckmann, V., & Shrader, C. R. 2012, in Active Galactic Nuclei (Weinheim, Germany: Wiley-VCH Verlag GmbH)

Beckwith, K., Hawley, J. F., & Krolik, J. H. 2009, ApJ, 707, 428

Begelman, M., Blandford, R., & Rees, M. 1984, Theory of extragalactic radio sources

Berendzen, R., & Hoskin, M. 1971, Astronomical Society of the Pacific Leaflets, 10, 425

Bîrzan, L., McNamara, B. R., Nulsen, P. E. J., Carilli, C. L., & Wise, M. W. 2008, ApJ, 686, 859

Bîrzan, L., Rafferty, D. A., McNamara, B. R., Wise, M. W., & Nulsen, P. E. J. 2004, ApJ, 607, 800

Blandford, R., Meier, D., & Readhead, A. 2018, arXiv preprint, arXiv:1812.06025

Blandford, R. D., & Konigl, A. 1979, ApJ, 232, 34

Blandford, R. D., & Payne, D. G. 1982, MNRAS, 199, 883

Blandford, R. D., & Znajek, R. L. 1977, MNRAS, 179, 433

Bodo, G., Rossi, P., Massaglia, S., et al. 1998, A&A, 333, 1117

Bolton, J. G., & Stanley, G. J. 1948, Nature, 161, 312

Bower, R. G., Benson, A. J., Malbon, R., et al. 2006, MNRAS, 370, 645

Bryan, G. L., Norman, M. L., O'Shea, B. W., et al. 2014, ApJS, 211, 19

Bugli, M., Del Zanna, L., & Bucciantini, N. 2014, MNRAS, 440, L41

Burbidge, E. M., Burbidge, G. R., & Prendergast., K. H. 1959, ApJ, 130, 26

Burns, J. O. 1990, AJ, 99, 14

Castor, J., Weaver, R., & McCray, R. 1975, ApJ, 200, L107

Cattaneo, A., Faber, S. M., Binney, J., et al. 2009, Nature, 460, 213

Cielo, S., Antonuccio-Delogu, V., Maccio, A. V., Romeo, A. D., & Silk, J. 2014, MNRAS, 439, 2903

Ciotti, L., & Ostriker, J. P. 1997, ApJ, 487, L105

Cirasuolo, M., Celotti, A., Magliocchetti, M., & Danese, L. 2003, MNRAS, 346, 447

Cox, C. I., Gull, S. F., & Scheuer, P. A. G. 1991, MNRAS, 252, 558

Croston, J. H., Ineson, J., & Hardcastle, M. J. 2018, MNRAS, 476, 1614

Croton, D. J., Springel, V., White, S. D. M., et al. 2006, MNRAS, 365, 11

Dubey, A., Antypas, K., Ganapathy, M. K., et al. 2009, Parallel Computing, 35, 512

Fabian, A. C. 1994, ARAA, 32, 277

—. 1999, MNRAS, 308, L39

—. 2012, ARAA, 50, 455

Fabian, A. C., Sanders, J. S., Allen, S. W., et al. 2003, MNRAS, 344, L43

Fabian, A. C., Sanders, J. S., Taylor, G. B., et al. 2006, MNRAS, 366, 417

Fabian, A. C., Sanders, J. S., Ettori, S., et al. 2000, MNRAS, 318, L65

Fabian, A. C., Sanders, J. S., Allen, S. W., et al. 2011, MNRAS, 418, 2154

Ferrarese, L., & Merritt, D. 2000, ApJ, 539, L9

Ferrari, A. 1998, ARAA, 36, 539

Fryxell, B., Olson, K., Ricker, P., et al. 2000, ApJS, 131, 273

Gebhardt, K., Bender, R., Bower, G., et al. 2000, ApJL, 539, L13

Guan, X., Li, H., & Li, S. 2014, ApJ, 781, 48

Hawley, J. F., Fendt, C., Hardcastle, M., Nokhrina, E., & Tchekhovskoy, A. 2015, Space Science Reviews, 1, 53

Heckman, T. M., & Best, P. N. 2014, ARAA, 52, 589

Hopkins, P. F. 2015, MNRAS, 450, 53

Hoyle, F., Fowler, W. A., Burbidge, G. R., & Burbidge, E. M. 1964, ApJ, 139, 909

Hubble, E. P. 1925, Popular Astronomy, 33, 252

—. 1926, ApJ, 64, 321

—. 1929, ApJ, 69, 103

Jansky, K. G. 1933, Radio waves from outside the solar system, doi:10.1038/132066a0

Jennison, R. C., & Das Gupta, M. K. 1953, Nature, 172, 996

Kim, J.-h., Agertz, O., Teyssier, R., et al. 2016, ApJ, 833, 202

King, A., & Pounds, K. 2014, ARAA, 53, arXiv:1503.05206

Leavitt, H. S. 1908, Annals of Harvard College Observatory, 60, 87

Leavitt, H. S., & Pickering, E. C. 1912, Harvard College Observatory Circular, 173, 1

Lee, D. 2013, Journal of Computational Physics, 243, 269

Li, H., Lapenta, G., Finn, J. M., Li, S., & Colgate, S. A. 2006, ApJ, 643, 92

Liska, M., Hesp, C., Tchekhovskoy, A., et al. 2018, MNRAS, 474, L81

Lyubarsky, Y., & Yuri. 2009, ApJ, 698, 1570

Machalski, J., Kozieł-Wierzbowska, D., Jamrozy, M., & Saikia, D. J. 2008, ApJ, 679, 149

Marti, J. M., Mueller, E., & Ibanez, J. M. 1994, A&A, 281, L9

Marti, J. M., Muller, E., Font, J. A., Ibanez, J. M., & Marquina, A. 1997, ApJ, 479, 151

McConnachie, A. W., Irwin, M. J., Ferguson, A. M., et al. 2005, MNRAS, 356, 979

McKinney, J. C., & Blandford, R. D. 2009, MNRAS, 394, L126

McNamara, B. R., & Nulsen, P. E. J. 2012, New Journal of Physics, 14, 055023

Mendygral, P. J., Jones, T. W., & Dolag, K. 2012, ApJ, 750, 166

Mendygral, P. J., O'Neill, S. M., & Jones, T. W. 2011, ApJ, 730, 100

Mizuta, A., Kino, M., & Nagakura, H. 2010, ApJ, 709, L83

Morsony, B. J., Heinz, S., Brüggen, M., & Ruszkowski, M. 2010, MNRAS, 407, 1277

Nakamura, M., Li, H., & Li, S. 2006, ApJ, 652, 1059

—. 2007, ApJ, 656, 721

Norman, M. L., Smarr, L., Winkler, K.-H. A. K.-H. A., et al. 1982, A&A, 113, 285

O'Neill, S. M., Beckwith, K., & Begelman, M. C. 2012, MNRAS, 422, 1436

O'Shea, B. W., Nagamine, K., Springel, V., Hernquist, L., & Norman, M. L. 2005, ApJS, 160, 1

Pedlar, A., Ghataure, H. S., Davies, R. D., et al. 1990, MNRAS, 246

Perucho, M., & Bosch-Ramon, V. 2012, A&A, 539, A57

Porth, O., & Fendt, C. 2010, ApJ, 709, 1100

Reber, G. 1942, Proceedings of the IRE, 30, 367

Reynolds, C. S., Fabian, A. C., Celotti, A., & Rees, M. J. 1996, MNRAS, 283, 873

Rossi, P., Mignone, A., Bodo, G., Massaglia, S., & Ferrari, A. 2008, A&A, 488, 795

Salpeter, E. E. 1964, ApJ, 140, 796

Sanders, D. B., Soifer, B. T., Elias, J. H., et al. 1988, ApJ, 325, 74

Scheuer, P. A. G. 1974, MNRAS, 166, 513

Schmidt, M. 1963, Nature, 197, 1040

Seyfert, C. K. 1943, ApJ, 97, 28

Shapley, H., & Curtis, H. D. 1921, Bulletin of the National Research Council, 2, 171

Shields, G. A. 1999, PASP, 111, 661

Sikora, M., Begelman, M. C., Madejski, G. M., & Lasota, J. 2005, ApJ, 625, 72

Silk, J., & Rees, M. J. 1998, A&A, 331, L1

Slipher, V. M. 1917, Proceedings of the American Philosophical Society, 56, 403

Springel, V. 2005, MNRAS, 364, 1105

—. 2010, Mon. Not. R. Astron. Soc, 401, 791

Stone, J. M., Mihalas, D., & Norman, M. L. 1992, ApJS, 80, 819

Tchekhovskoy, A. 2015, in The Formation and Disruption of Black Hole Jets, ed. I. Contopoulos, D. Gabuzda, & N. Kylafis (Springer International Publishing Switzerland), 45–82

Tchekhovskoy, A., & Bromberg, O. 2016, MNRAS, 461, L46

Tchekhovskoy, A., Narayan, R., & McKinney, J. C. 2011, MNRAS, 418, L79

The IceCube Collaboration, Fermi-LAT, MAGIC, et al. 2018, Science (New York, N.Y.), 361, 146

Tout, C., & Pringle, J. E. 1996, Monthly Notices of the Royal, 281, 219

Tremblay, G., O'Dea, C., Baum, S., et al. 2010, ApJ, 715, 172

Trimble, V. 1995, PASP, 107, 1133

Urry, C. M., & Padovani, P. 1995, PASP, 107, 803

White, R. L., Becker, R. H., Gregg, M. D., et al. 2000, ApJS, 126, 133

Chapter 2

Effect of Magnetic Field Topology in the Jets-Ambient Medium Interaction – Instabilities and Synchrotron Properties

Abstract

We present a series of magneto-hydrodynamic (MHD) simulations of jets injected with dynamically important magnetic fields and different magnetic field configurations interacting with the intra-cluster medium. The simulations show that the structure of the field could affect the collimation of the jets and thus the morphology of the radio lobes. We develop a computationally efficient framework based on tracer particles to follow the synchrotron cooling of the radio lobes. We find the gradient of spectral index is reversed in the quiescently evolved radio sources after the jet turns off. We present synthesized radio polarimetry that shows distinct polarization features due to the field structure of the jets.

2.1 Introduction

Radio galaxies are commonly observed to have extended and various morphologies if they are resolved (Fanaroff & Riley 1974; Banfield et al. 2015). Nearby sources are seen with rich structures inside their lobes (Leahy et al. 1996; Miley 2003). The radio lobes consist of synchrotron emitting plasma injected by the relativistic jets coming from the supermassive black holes at the center of galaxies. The AGN feedback revealed by the radio sources could play an important role in the evolution of galaxies and clusters of galaxies (see e.g. McNamara & Nulsen 2012, for review).

Jets are thought to be launched by extracting the rotational energy from the black hole (Blandford & Znajek 1977, hereafter BZ) or the accretion disk (Blandford & Payne 1982) through the threading of magnetic fields into the event horizon or the disk. The jet power of the BZ mechanism depends on the magnetic flux and spin of the black hole, which both remain mostly unknown. Large-scale poloidal fields, which could be advected by the accretion flow from larger radius (Beckwith et al. 2009) or generated through a dynamo around the compact object (Tout & Pringle 1996; Bugli et al. 2014), are necessary to accelerate the jets. The twisting of the magnetic fields by the rotation of the black hole or the accretion disk naturally leads to toroidal fields (Tchekhovskoy 2015). It is thought that around the vicinity of the black hole, the flow could be dominated by Poynting flux as in the original BZ mechanism and modeled by Li et al. (2006) and Guan et al. (2014), in which the magnetic energy density is much larger than the kinetic and thermal energy. If the magnetic energy is transferred to the particles within the jets, the particles can be accelerated to highly relativistic velocity through a large range of scales (Heinz & Begelman 2000; Lyubarsky & Yuri 2009). Collimation , which could come from

the magnetohydrodynamical structure of the jets (Nakamura et al. 2007; McKinney & Blandford 2009) or from external pressure such as disk winds (Porth & Fendt 2010), helps the jets remain beam-like for hundreds of kpc.

Although it is generally believed that ordered fields on the scale of the jet radius are necessary to launch and collimate the relativistic outflow, we still do not know whether the field structure can be preserved in the jets or in the radio lobes that are orders of magnitude larger than the jet radius. The BZ mechanism requires strong poloidal fields threading the event horizon of the black hole to accelerate the jets. Beckwith et al. (2008) tried different magnetic field structures, including poloidal, toroidal, and quadrupolar in global general relativistic magneto-hydrodynamic (GRMHD) simulations, and found that only poloidal magnetic fields can generate jets. In the jets, the pitch angle between the poloidal and toroidal magnetic fields play an essential role during the propagation of the jets. Bromberg & Tchekhovskoy (2016) point out that this pitch angle depends on the external medium that confines the jets and denser medium will result in smaller pitch angle, i.e. stronger toroidal fields. Braithwaite (2010) argue that the AGN outflows must have had high helicity to support the long-lasting rising bubble.

Observationally, Gabuzda et al. (2015) found gradients of Faraday rotation measure across the jet structure in observations with the Very Long Baseline Array (VLBA). These gradients suggest the existence of toroidal components of the magnetic field at least in the central few 10-pc region. However, Faraday rotation shows only magnetic fields along the line of sight and can not tell the fields perpendicular to it. We still do not have direct observation of the ratio of toroidal to poloidal field strength. Although there is no clear evidence of recent jet activity in the Milky Way, Nishiyama et al. (2010) has shown the transition from toroidal fields near the Galactic plane to poloidal fields at high Galactic latitude, suggesting ordered magnetic fields around the Galactic center from which the

black hole would have accreted.

In this work, we focus on the interaction of the jets with ambient gas, assuming most of the magnetic energy has been converted to kinetic energy at the inlets of our injection nozzle roughly about 100 pc from the black hole. Although the energy flux is dominated by the kinetic energy in our simulations, magnetic fields are still dynamically important on larger scales. The simulation domain is assumed to be a spherically symmetric intracluster medium in hydrostatic equilibrium, chosen to approximate observations of the Perseus Cluster. To better follow the evolution of the synchrotron spectra, we developed and implemented tracer particles for synchrotron cooling (section 2.2.5). With marginal computational cost, we are able to produce synthesized radio maps with a realistic synchrotron aging model.

The driving motivation of our simulations are the following two questions: 1) How will the topology of magnetic fields of the jets affect the dynamical evolution of radio lobes? 2) Are there any polarization diagnostics from the structure of the radio lobes to infer the magnetic field structure of the jets? We present a series of adaptively refined high-resolution MHD simulations of the AGN jets with different injecting field topology: pure toroidal, pure poloidal, and helical magnetic fields inside the jets, and study the dynamics and synchrotron properties of the simulation products. This work is organized as follows. In Section 2.2, we describe the methodology and techniques used in the simulations. In Section 2.3, we present the results of the simulations, including the dynamics and synchrotron properties. In Section 2.4 and 2.5, we discuss and summarize our findings.

2.2 Numerical Techniques

We use the grid-based adaptive mesh-refinement (AMR) MHD code `FLASH`[1] (Fryxell et al. 2000; Dubey et al. 2009) to perform the simulations. Full 3D simulations are conducted to catch the non-linear physics of the magnetic fields. We include full-resolution simulations of back-to-back jets. This allows us to properly model jet-driven large scale flows across the mid-plane and to use a comparison of the two sides to estimate the uncertainty in derived quantities due to the stochasticity of non-linear fluid mechanics.

We use the unsplit staggered mesh (USM) scheme implemented in Lee (2013) for solving the MHD equations. The USM algorithm in `FLASH` is a finite-volume Godunov scheme consisting of a constrained transport method that preserves the divergence-free nature of magnetic field to machine precision. We use the hybrid Riemann solver, which combines HLL and HLLD solver for high accuracy and stability, 3rd- order reconstruction and the mc slope limiter.

The initial conditions are described in Section 2.2.1. The simulation box is $1 \times 0.5 \times 0.5$ Mpc with $16 \times 8 \times 8$ base blocks and hydrostatic diode boundary condition (`hydrostatic-f2+nvdiode`). Each block has 8 by 8 by 8 cells. The minimum cell size is 30 pc under 9 levels of adaptive refinement. The jet nozzle diameter is resolved by 2 blocks, or 16 cells. The refinement criteria include the native second derivative based estimator and also a self-defined momentum-based condition that ensures that we resolve the jets at the highest level of refinement. We restrict the maximum refinement level for the ICM further away from the center that the number of blocks to the center is always larger than 32 in the direction of the jet.

The jets are active at a constant jet power until 10 Myr. The maximum refinement

[1] http://flash.uchicago.edu/

level used to resolve the jets is reduced after the jets are turned off at 10 Myr for computational expediency as described below.

The gravitational potential is set up so that the intracluster medium is in hydrostatic equilibrium for the initial conditions described in Section 2.2.1. The cluster potential is assumed to be spherically symmetric and static throughout the simulations, neglecting changes in the gravitational potential due to the changes in gas density, which is equivalent to assuming that gravity is dominated by dark matter.

Most of the visualization and analysis work is performed with the `python`-based software package `yt`[2] (Turk et al. 2010). The 3D rendering is carried out in `VisIt` (Childs et al. 2012).

2.2.1 Initial Conditions

We simulate jet propagation into an initially non-magnetized cluster in hydrostatic equilibrium and inject the highly magnetized ($\beta_p = p_{\rm gas}/p_B \sim 1$) jets at the center of the cluster. Initial density and temperature profiles are set according to recent observations of the Perseus Cluster by Zhuravleva et al. (2015). We describe the analytical formula of the profile in this section. The respective numerical value of each variable can be found in Table 2.1.

The density profile follows a spherically symmetric β-model, which is formulated as

$$\rho(r) = \frac{\rho_0}{[1 + (\frac{r}{r_c})^2]^{\frac{3}{2}\beta}}. \tag{2.1}$$

The temperature profile is set such that the core of the cluster is cooler than the outskirt as we have seen in cool core clusters.

$$T(r) = \frac{T_{\rm out}[1 + (\frac{r}{r_{\rm c,T}})^3]}{\frac{T_{\rm out}}{T_{\rm core}} + (\frac{r}{r_{\rm c,T}})^3}. \tag{2.2}$$

[2] http://yt-project.org/

Note that the core radius for the temperature profile is different from the core radius for the density profile. The radial profile is plotted in Fig. 2.1. The jet and the ICM fluids follow ideal gas law with respective $\gamma_j = 4/3$ and $\gamma_{\rm ICM} = 5/3$. The mean molecular weight μ is assumed to be the same for both fluids.

Table 2.1 : List of variables used in the simulation.

Variable	**Symbol**	**Value**	**Unit**
jet power	L	1×10^{45}	erg/s
jet velocity	v_j	3×10^9	cm/s
jet gamma	γ_j	4/3	
jet density*	ρ_j	1.73×10^{-26}	g/cm^3
jet nozzle radius	$r_{\rm jet}$	7.5×10^{20} 243	cm pc
jet magnetic field*	B	1.7×10^{-4}	gauss
jet plasma beta	β_p	1	
jet internal Mach number	M_j	10	
jet toroidal to poloidal field ratio	h	∞, 1, 0	
mean molecular weight	μ	0.61	
ICM core density	ρ_0	9.6×10^{-26}	g/cm^3
ICM density profile beta	β	0.53	
ICM density profile core radius	r_c	26	kpc
ICM core temperature	$T_{\rm core}$	3.0 3.5×10^7	keV K
ICM outer temperature	$T_{\rm out}$	6.4 7.4×10^7	keV K
ICM temperature profile core radius	$r_{\rm c,T}$	60	kpc
ICM gamma	$\gamma_{\rm ICM}$	5/3	

*: not a free parameter, but is determined by other parameters.

2.2.2 Injection of the Jets

The jets are injected into the grid through a cylindrical "nozzle" at the center of the simulation domain (see, e.g. Heinz et al. 2006; Morsony et al. 2010). The total energy output is governed by the choice of the radius, velocity v_j, density ρ_j, Mach number M_j, and toroidal magnetic field strength B_ϕ inside the nozzle. Energy, mass, and magnetic flux are injected into the simulation domain through the nozzle. The power of the jets L can be expressed as the sum of the kinetic energy flux, the enthalpy flux, and the Poynting flux which can be expressed as the integral over the nozzle cross-section

$$L = 2 \int v_j \left(\frac{1}{2} \rho_j v_j^2 + \frac{\gamma_j}{\gamma_j - 1} P_j + \frac{B_\phi^2}{8\pi} \right) \cdot \mathrm{d}a, \tag{2.3}$$

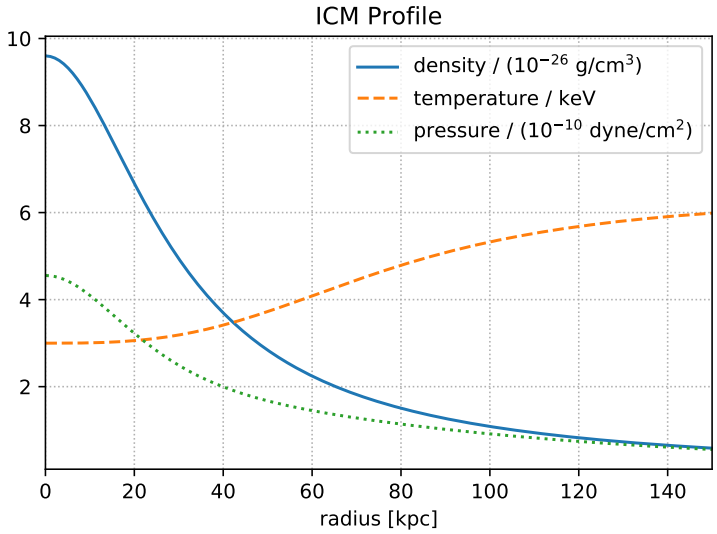

Figure 2.1 : Radial profiles of the initial conditions implemented in our simulations. The profile is constructed by the parameters inferred from recent observation of the Perseus Cluster and the condition of hydrostatic equilibrium. Analytical prescriptions can be found in Section 2.2.1. The gravity is set up such that the initial cluster is in hydrostatic equilibrium.

where the factor of 2 accounts for two sides of the nozzle. The radial velocity profile of the jet is constant within the nozzle radius (r_1 in Fig. 2.3) and gradually goes to zero (at $r_{\rm out}$) in a tapering feather region set to be 1/4 of the nozzle radius.

$$v_j(r) = \begin{cases} v_0 & \text{if } 0 < r \leq r_2 \\ \frac{v_0}{2}\left(1 + \cos(\pi \frac{r - r_2}{r_{\rm out} - r_2})\right) & \text{if } r_2 < r \leq r_{\rm out} \\ 0 & \text{if } r > r_{\rm out} \end{cases} \tag{2.4}$$

The integral in Equation 2.3 is used to calculate the total energy input throughout the nozzle. The kinetic and thermal power are kept to be the same across all simulations. We use the jet's internal Mach number to parametrize the ratio between density and pressure given a fixed fluid velocity

$$M_j = \frac{v_j}{c_s} = v\sqrt{\frac{\rho_j}{\gamma_j P_j}}. \tag{2.5}$$

The plasma β_p, defined as the ratio of thermal to magnetic pressure

$$\beta_p = \frac{p_j}{p_B}. \tag{2.6}$$

is used to parametrize the strength of the magnetic field inside the jet and is set to 1 for all magnetized jets. The magnetic pressure includes both toroidal (B_ϕ) and poloidal (B_z) fields inside the nozzle.

$$p_B = \frac{B^2}{8\pi} = \frac{B_\phi^2 + B_z^2}{8\pi} \tag{2.7}$$

2.2.3 Magnetic Fields Inside the Jets

We set up 3 different cases of magnetized jets with toroidal, helical, and poloidal fields in the jets (as depicted in Fig. 2.2), along with a non-magnetized case (hereafter the hydro case) as a control case.

We use a polynomial expression for B_ϕ to construct a smooth toroidal magnetic field inside the jet, which is constant ($B_{\phi 0}$) in most parts of the jet and approaches zero at the

axis $r = 0$ and the boundary $r = r_{\rm jet}$. We split B_ϕ into 3 regions: 0 to r_1, r_1 to r_2, and r_2 to $r_{\rm jet}$. The polynomials are constructed such that the derivatives are also smooth at the boundaries. The following functions are used for such field:

$$B_\phi = B_{\phi 0} \begin{cases} -\dfrac{2r^3}{r_1^3} + \dfrac{3r^2}{r_1^2} & \text{if } 0 < r < r_1 \\ 1 & \text{if } r_1 < r < r_2 \\ -\dfrac{2(r_{\rm out} - r)^3}{(r_{\rm out} - r_2)^3} + \dfrac{3(r_{\rm out} - r)^2}{(r_{\rm out} - r_2)^2} & \text{if } r_2 < r < r_{\rm out} \end{cases} \tag{2.8}$$

Poloidal fields B_z are designed to be constant (B_{z0}) inside the jet and reverse the direction outside the nozzle such that the magnetic loop is closed. The B_z outside of the

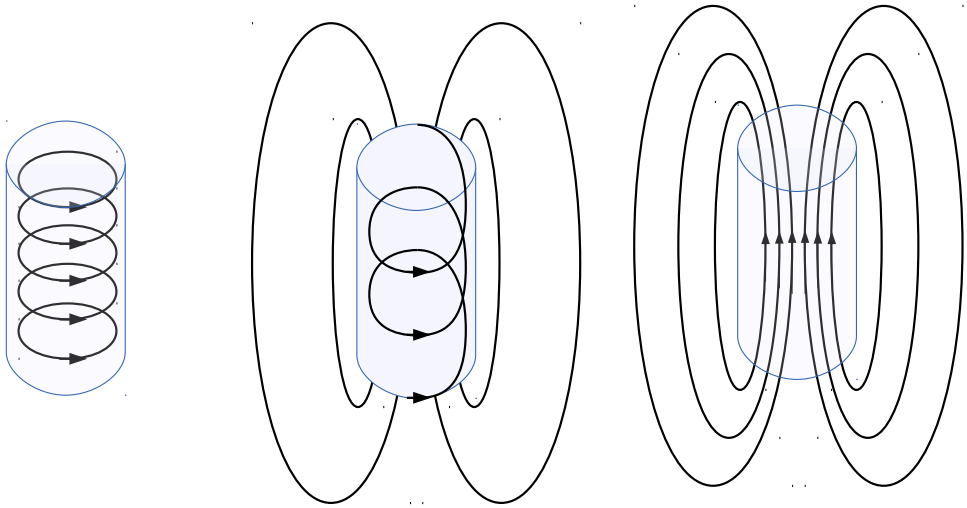

Figure 2.2 : Schematic drawings of toroidal (*left*), helical (*middle*), and poloidal (*left*) magnetic field lines in the simulation. The total magnetic field strength is set to be the same for all 3 cases. The shaded regions indicate the size of the jet nozzle. Note that the drawing shows only poloidal field in the plane, but the actual field is axisymmetric.

nozzle is 10% of the strength inside. The same as in the toroidal fields, we construct the functional form of B_z to ensure smooth derivatives at the transitions. The resulting profile of the magnetic fields is shown in Fig. 2.3.

In practice, we use vector potential $\mathbf{A}$ to prescribe the magnetic field to ensure we have a divergence-free field.

$$A_r = 0 \tag{2.9a}$$

$$A_\phi = \frac{1}{r}\int r B_z \, \mathrm{d}r \tag{2.9b}$$

$$A_z = \int B_\phi \, \mathrm{d}r \tag{2.9c}$$

In order to replenish the toroidal fields as the fluid in the nozzle moves out, we calculate the advection rate and add proper flux to maintain the same magnetic field strength. The field injection region is outside of the hydrodynamic nozzle.

A parameter h is used to control the ratio between toroidal and poloidal components inside the jet nozzle

$$h = \frac{B_{\phi 0}}{B_{z0}}. \tag{2.10}$$

We set $h = \infty$ for toroidal case, $h = 1$ for helical case, and $h = 0$ for poloidal case. The total magnetic field pressure is set to be the same for all 3 cases, such that

$$(B_\phi^{\text{toroidal}})^2 = (B_\phi^{\text{helical}})^2 + (B_z^{\text{helical}})^2 = (B_z^{\text{poloidal}})^2 \tag{2.11}$$

2.2.4 Jet Jitter

We include a modest variation in the jet direction around the mean jet axis, which is oriented along the z-axis of the simulation box. This jitter is imposed for two reasons:

First, it is known from observations that the jet axis changes direction on timescales comparable to the jet travel time (e.g. Nulsen et al. 2002; Young et al. 2005). This may be

due to bona fide jet precession, but even in the absence of an ordered, secular variation in jet axis, dynamical instabilities in the accretion disks and jets are likely to cause moderate changes in orientation (Pringle 1996; Heinz et al. 2006). Extreme re-orientation between episodes of jet activities could result in X-shaped radio sources that have been observed (Dennett-Thorpe et al. 2002; Roberts et al. 2018). This, however, is not what we are

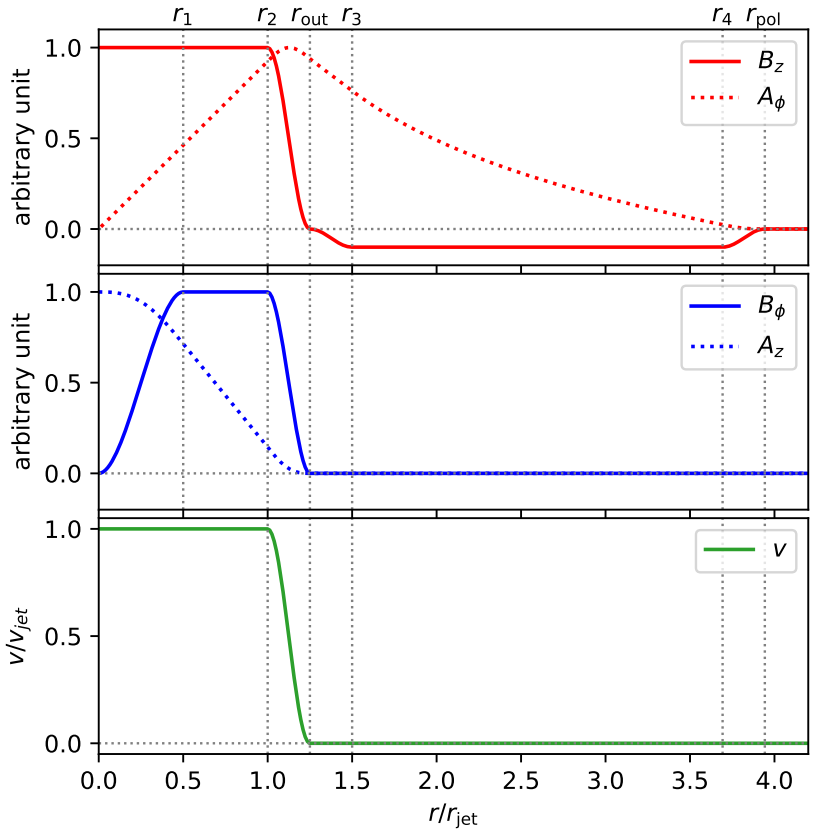

Figure 2.3 : Radial profiles of the magnetic fields (upper panel) and velocity (lower panel) inside and outside the nozzle. The inner tapering radius r_1 is set to be 1/2 of the nozzle radius. The tapering feather ($r_{\rm out} - r_2$, $r_3 - r_{\rm out}$, and $r_{{\rm pol}-r_4}$) is set to be 1/4 of the nozzle radius. The poloidal field (B_z) closes outside of the nozzle, where we can see negative values. The B_z outside of the nozzle is set to be 10% of the field in the nozzle and r_4 is the corresponding radius to close the field loop.

modeling in this work.

Second, analytic and numerical models of uni-directional jets do not generally reproduce the well-known shape of radio galaxies, leading to much larger aspect ratios of cocoons and radio lobes than observed (e.g. Norman et al. 1982; Marti et al. 1994), and are insufficient to couple the AGN energy to the central cluster (Vernaleo & Reynolds 2006). This led Scheuer (1974, 1982) to propose the so-called dentist drill effect, which spread jet thrust over a much larger cone than that prescribed by the jet's opening angle. Several studies also show that the precession of the jets is necessary to match the observed morphology of the radio emission (see e.g. Heinz et al. 2006; Nawaz et al. 2016).

This is particularly important in simulations like ours that are not fully relativistic: Relativistic jets with a velocity close to c have an energy-to-momentum ratio of about c, while in our simulation the speed of the jets is set to be 0.1 c and has a smaller energy-to-momentum ratio. The result of the excess momentum leads to an elongated shape that does not fit observations (see Fig. 2.6).

To offset this effect, we let the pointing direction of the jet precess in a random walk prescription and limited within a given opening angle. One can see the jets are bent in Fig. 2.5 due to the introduction of this jittering. The motion of the jet axis throughout the simulation is shown in Fig. 2.4. The opening angle of this cone is small—the average angle between the jet and the z-axis is about 8 degrees, corresponding to the typical change one would expect due to dynamical instabilities within the jet and potential changes in jet direction from either change in the net angular momentum of accreted material or disk precession.

We produce two sets of simulations with and without the jitter effects. A set of non-precessing jets with toroidal, helical, poloidal, and no magnetic fields are first performed to study the propagation and effect of the magnetic field topology. These results are presented

in Section 2.3.1 and 2.4.1. For the rest of the chapter, we focus on the simulations with the implementation of the jet jittering described here.

2.2.5 Synchrotron Cooling Tracer Particles

The intensity of the non-thermal synchrotron emission depends on (a) the number density of electrons, which is derived from the energy density in the simulations, assum-

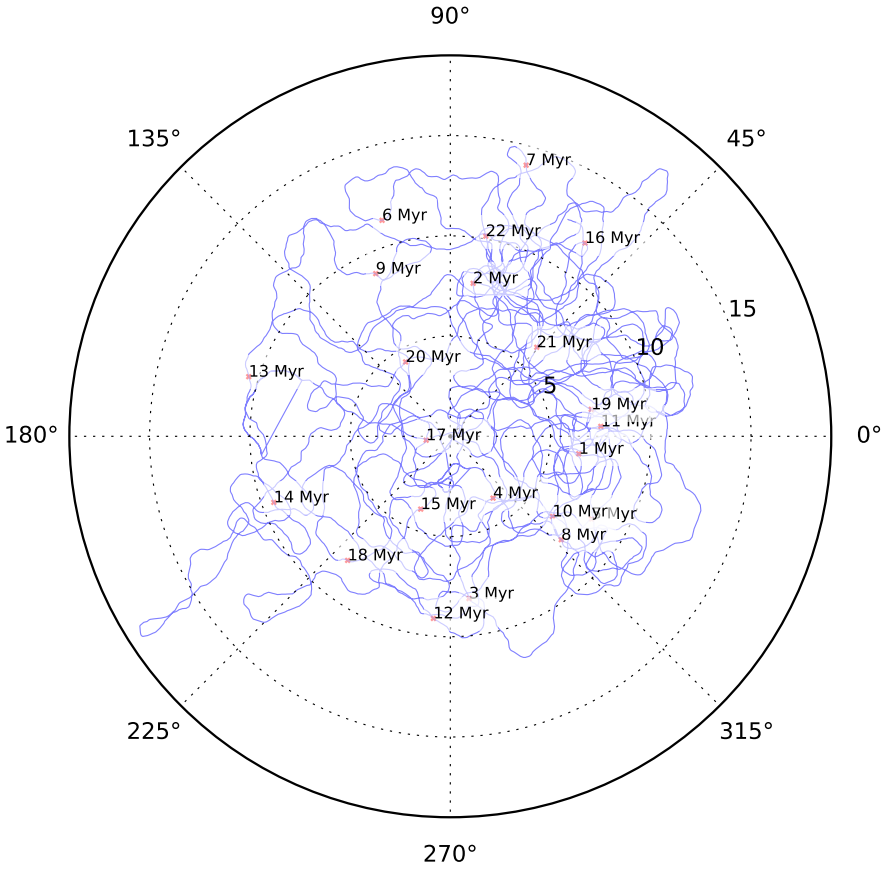

Figure 2.4 : The pattern of the jet pointing direction as implemented in the simulation. The pointing undergoes a random walk process but is constrained by a maximal angle that can be set in the simulation. Red crosses label the position and time of the pointing since the launch of the jet. The labels on the radial-axis are in unit of degrees, from 0 to 20°.

ing the internal energy of the fluid is dominated by the relativistic electrons, and (b) the strength and orientation of the magnetic fields, which is readily available in MHD simulations or assumed to be a fraction of the thermal energy density in hydrodynamic simulations (e.g. Mimica et al. 2009; Obergaulinger et al. 2015). However, to obtain the spectra of the synchrotron emission, one still needs (c) the energy distribution of the electrons. There are several ways to account for (c), including assuming a simple power-law (e.g. Hardcastle & Krause 2014; English et al. 2016), grid-based electron population transport model, for example in Del Zanna et al. (2008); Mendygral et al. (2012), or Lagrangian particle-based electron transport in (Mimica et al. 2009; Vaidya et al. 2016, 2018).

We develop and implement a simple yet powerful framework to study synchrotron emission in our simulation. Our technique is built on top of the Lagrangian particle framework in `FLASH` (Dubey et al. 2012). To trace the cooling of relativistic electrons, processes of synchrotron radiation and adiabatic expansion/compression are tracked by individual computational Lagrangian tracer *particles*. Bicknell & Melrose (1982); Coleman & Bicknell (1988) show that the population transport equations for particles subject to synchrotron losses and adiabatic compression can be solved analytically. For an initial powerlaw distribution of electrons, the distribution is then represented by the power-law index and the cut-off energy. In this framework, each *particle* essentially tracks this cut-off energy, rather than solving the transport equation on a grid of the energy distribution.

This requires significantly less computation and memory footprint than solving the full transport equations numerically (Mendygral et al. 2012; Vaidya et al. 2018). More importantly, the existence of a closed, analytic solution to the transport equation makes this approach more *accurate* than a finite-difference solution of the same equation.

Using the numerically integrated analytic solution of the transport equation for each synchrotron tracer particle and total particle pressure and magnetic fields from the

grid, we can then produce synthesized synchrotron emission maps, including polarization information, at any frequency in post-processing. Although we will focus on the radio-frequency radiation in this work, this framework can be extended to synchrotron emission in higher energy bands, e.g. in the x-ray.

Note that the term *particle* here refers to the numerical perspective of an element that moves spatially during the simulation. Each *particle* represents an ensemble of non-thermal electrons that are modeled in the spatial proximity of the location of the tracer particle. The cooling of the electrons is governed by synchrotron losses, which depend on the magnetic field strength, and by adiabatic expansion or compression, i.e. the ratio of current fluid density to initial density. We assume the synchrotron radiation from the radio lobes is optically thin to self-absorption, and the radiation energy is negligible compared to the thermal energy of the gas. This is consistent with most extended radio sources observed, which have steep spectral indices (see e.g. Laing et al. 1983).

In this work, particles are injected at the cross-sections of the jet nozzle and are assumed to represent a power-law distribution of relativistic electrons. However, the same particles can be injected anywhere in the simulation domain where acceleration processes take place. Indeed, further development of our framework will be suitable for studying and disentangling different acceleration mechanisms.

The solution to the electron transport equation subject to synchrotron and adiabatic cooling can be found in Bicknell & Melrose (1982); Coleman & Bicknell (1988). A detailed derivation can be found in Appendix A.1. For each *particle*, the cutoff frequency can be calculated as

$$\gamma_{\rm cut}(t) = \frac{\left(\frac{n(t)}{n_0}\right)^{\frac{1}{3}}}{\int_{t_0}^{t} A(t')\,(\frac{n(t')}{n_0})^{\frac{1}{3}}\,\mathrm{d}t'}, \tag{2.12}$$

where $n(t)$ is the number density of electrons at time t, n_0 is the initial number density of

particle, and $A = \frac{4\sigma_T}{3m_e c} U_B$ is the energy loss rate for the synchrotron process.

In the simulation, we have to choose a time to begin the integration. This is when the electrons are accelerated to have a power-law energy distribution. While the acceleration mechanism is still not fully understood, the site of the acceleration can happen inside the jet (Bicknell & Melrose 1982) and/or at terminal hotspots due to magnetic field reconnection (Romanova & Lovelace 1992; Sironi & Spitkovsky 2014; Sironi et al. 2015; Guo et al. 2015) or diffusive shock acceleration (Bell 1978; Blandford & Ostriker 1978; Drury 1983; Caprioli & Spitkovsky 2014; Park et al. 2015). We choose to begin the cooling of the synchrotron electrons when the bulk velocity of the *particles* is less than half of the jet velocity (set to 0.1 c in our simulations). The choice has two implications: 1) If the particle goes through a terminal shock, the acceleration happens inside the terminal hotspots when the velocity of the fluid is greatly reduced. 2) If the particle does *not* go through a terminal shock, it is assumed that the acceleration happens inside the jets and the distribution of electrons is a perfect power-law.

Compared to the method used in other simulations, e.g. Hardcastle & Krause (2014), this method has the advantage of knowing the synchrotron spectra to the spatial resolution of the particles by implementing the synchrotron cooling tracer particles in addition to the orientation and strength of the magnetic fields. This makes the synthesized synchrotron maps more meaningful at different frequencies and allows us to model the frequency-dependent properties.

We would like to point out that we solve the kinetic equation analytically and integrate Equation 2.12 numerically. Our implementation is computationally more efficient and more accurate compared to dividing the energy distribution into many bins (e.g. in Vaidya et al. (2018)).

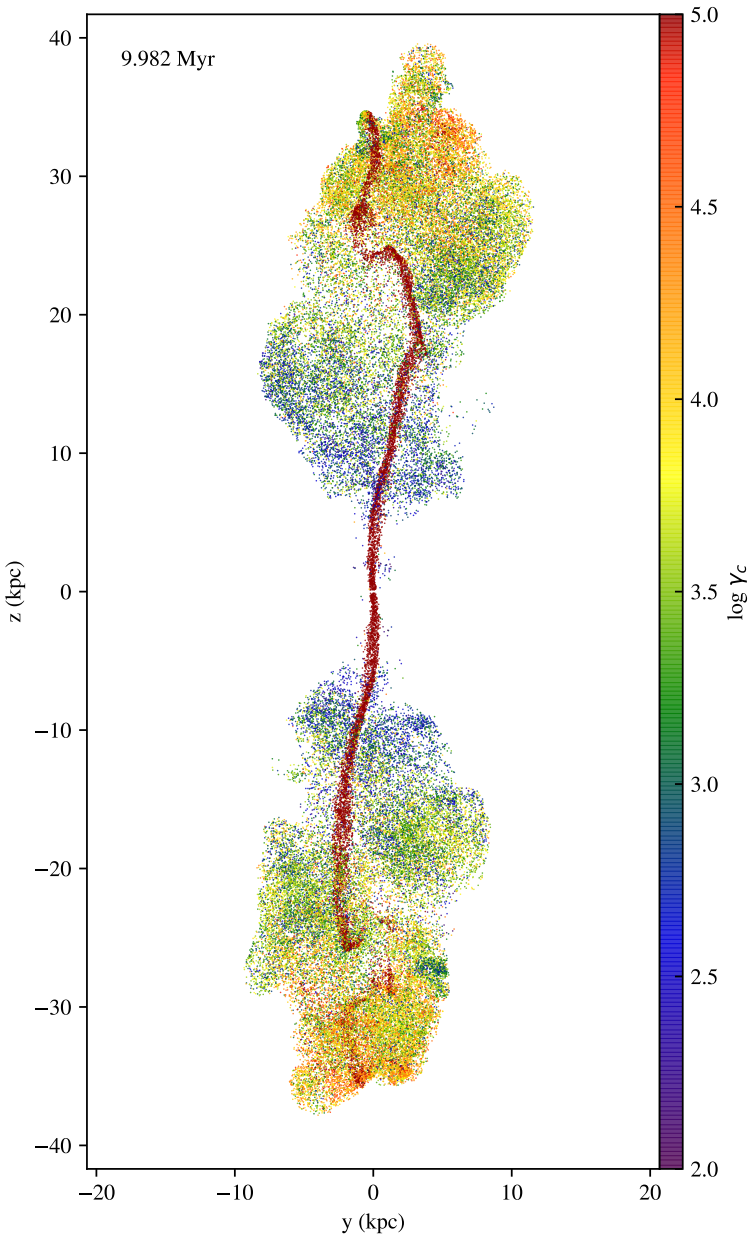

Figure 2.5 : Projection of particle $\gamma_{\rm cut}$, which corresponds to the cut-off energy of the electron distribution, at 10 Myr. Each particle, which represents an ensemble of electrons, is accelerated in the termination shocks, where it starts from a power-law distribution with infinitely large cut-off energy. As particles propagate with the fluid, their cut-off energy is changed due to synchrotron radiation and adiabatic expansion/compression.

2.2.6 Synchrotron Emissivity

We map the synchrotron spectrum of individual particles onto the grid and produce synthesized radio observations in post-processing of the simulated data. The synchrotron spectra of the grid cells are determined by the cut-off energy of the nearby particles weighted by inverse distance squared. The derivation can be found in Appendix A.2. The emissivity in each cell is calculated by

$$J(\nu,\alpha) = P(B\sin\alpha)^{\frac{3}{2}} \cdot \left[\frac{10e^{\frac{7}{2}}C_0}{8\sqrt{\pi}c^{\frac{9}{2}}m_e^{\frac{5}{2}}\ln(\frac{\gamma_{\max}}{\gamma_{\min}})}\nu^{-\frac{1}{2}}e^{\left(-\frac{\nu}{\nu_c(\gamma_{\max})}\right)}\right], \tag{2.13}$$

in which $\gamma_{\max}$ is taken from γ_{cut} of the tracer particles in Equation 2.12, and pressure P and magnetic field B are taken from the simulation grid. In practice, we calculate the value in the bracket for each tracer particle in our simulation. Then we fill the value in each cell of the grid by the weighted nearest neighbor deposition, in which the cell value is determined by the nearest 10 particles weighted by inverse distance square because not every computational cell contains a tracer *particle*. The emissivity calculated in Equation 2.13 is the total energy emitted per time per volume per frequency per solid angle.

The emissivity can then be integrated along the line-of-sight to calculate the synthesized synchrotron maps, which are presented in Section 2.3.3. We note that relativistic Doppler boost is not taken into account in the calculation. We correspondingly filter out the emission from the jet. The relativistic beaming effect will reduce the observed luminosity when the line-of-sight is perpendicular to the velocity by a factor of $1/\Gamma$, in which Γ is the bulk Lorentz factor of the fluid. Since we are using a non-relativistic code, the bulk Lorentz factor of the jet cannot be determined accurately.

2.2.7 Synchrotron Polarization

Synchrotron radiation is intrinsically polarized. Although hard to measure, the polarization of the emission could reveal useful and unique information about the emitting objects, including the magnetic field orientation in the plasma among others. Here we describe our technique to synthesize the synchrotron polarization from the MHD simulations.

In a single cell in the simulating domain, the magnetic field has a specific direction. The plasma will emit different strength of synchrotron radiation parallel and perpendicular to the magnetic field. The power of each is given by Equation A.34. For a power-law distribution of electrons, one can show the degree of polarization is

$$\Pi = \frac{p+1}{p+\frac{7}{3}}, \tag{2.14}$$

in which the power-law index p is assumed to be 2.

The excess of the perpendicular component is then transformed into Stokes Q and U parameters given an observational orientation. The Stokes Q and U are calculated for each cell in our simulation and later integrated through the line-of-sight to obtain the synthesized observations. A complete derivation is included in Appendix A.2.

$$Q(\nu,\alpha) = -\Pi \int J(\nu,\alpha)\cdot 2\cos(2\theta)\,\mathrm{d}l \tag{2.15a}$$

$$U(\nu,\alpha) = -\Pi \int J(\nu,\alpha)\cdot 2\sin(2\theta)\,\mathrm{d}l, \tag{2.15b}$$

where θ is the angle between the magnetic fields and the horizontal axis of the observation. The negative sign accounts for the fact that the perpendicular component is the major component of the synchrotron radiation, i.e. the radiation is primarily perpendicular to the magnetic fields.

2.3 Results

We investigate how different topology of the magnetic fields in the jets affect the jet-ambient medium interaction, including the collimation, propagation, and the imprints on the radio lobes.

2.3.1 Non-Precessing Jets

We first study the simulations without explicit precession to serve as our calibration and baseline cases. These non-precessing simulations have the same configuration as our primary simulations, but without the jittering mentioned in Section 2.2.4.

Snapshots of density slices from the four simulations are shown in Fig. 2.6. Upon comparing the simulations, we can see that each jet propagates at different speed into the external medium. Although the fluid velocity is set to be the same across all simulations, the head of the jet is influenced by the dynamics of magnetic fields and thus has different ability to propagate. In this section, we describe the analysis of the simulation results and discuss the mechanisms that make the jet head propagate at different velocities.

We determine the propagation velocity of the jet head in the simulations by measuring the endpoint of the jet fluid in the direction of the jet axis (z-axis). This is achieved by creating profiles of the jet fluid fraction weighted by the fluid mass against the z-coordinate. We then determine the location of the jet head to be where this fraction $f_{\rm W}$ exceeds 10^{-6}. Although we show only one side of the jets in Fig. 2.6, the simulations are performed for both sides. We analyze both sides (+z and -z) and the difference between them can be considered as the numerical uncertainty for the analysis.

Fig. 2.7 shows the results of this analysis. The edges of the shaded regions represent the location of the jet head in both sides. There are a few interesting points in this analysis. First, the toroidal jet propagates the fastest at the beginning (before 1 Myr) followed by the

helical and hydro jets, while the poloidal jet is the slowest. Second, the hydro jet becomes slightly faster than all others between 1 and 3 Myr, but slows down after about 3 Myr. Finally, at later times after 4 Myr, the poloidal jet remains the slowest, while the hydro jet becomes slower than the helical and toroidal jets. The hydro jet propagates at the velocity comparable to the poloidal jet.

Analytically, the propagation velocity of the jet head can be estimated by balancing the ram pressure in the frame of the jet head once the density ratio and the bulk velocity in the jets is known (see e.g. Norman & Winkler 1985). One will obtain the velocity of the

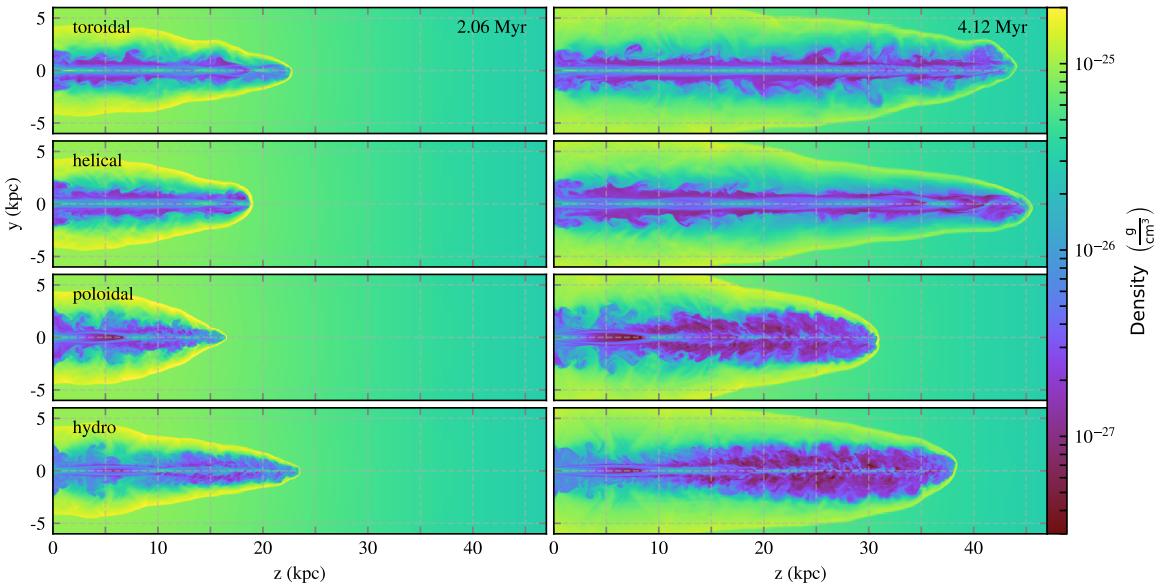

Figure 2.6 : Slices showing density through the central plane in simulations with constant jet direction (non-precessing) at two different times. From top to bottom: pure toroidal, helical, poloidal, no magnetic field. One can see the effect of the magnetic field on the propagation of jets. The toroidal component of the magnetic field imposes hoop stress on the flow and helps collimate the jets, while the poloidal component increases the lateral pressure and makes the jet expand. See texts for more discussions.

jet head as

$$v_h = \frac{\sqrt{\eta}}{1+\sqrt{\eta}} v_j, \tag{2.16}$$

where v_j is the jet fluid velocity and $\eta = \rho_j/\rho_e$ is the ratio of the jet fluid density and environment density. In our cases, the jet fluid velocity is fixed to be 0.1 c ($\sim$ 30 kpc/Myr), and the environmental density profile is also the same for all simulations. The variation of the propagation velocity comes from the density of the jet. Although the density of the nozzle is the same for all simulations, the different configurations of magnetic fields cause the jet to expand at different rates. Fig. 2.8 shows the density profile along the jet axis at about 4 Myr.

Even though in all simulations the jets begin with the same density in the nozzle,

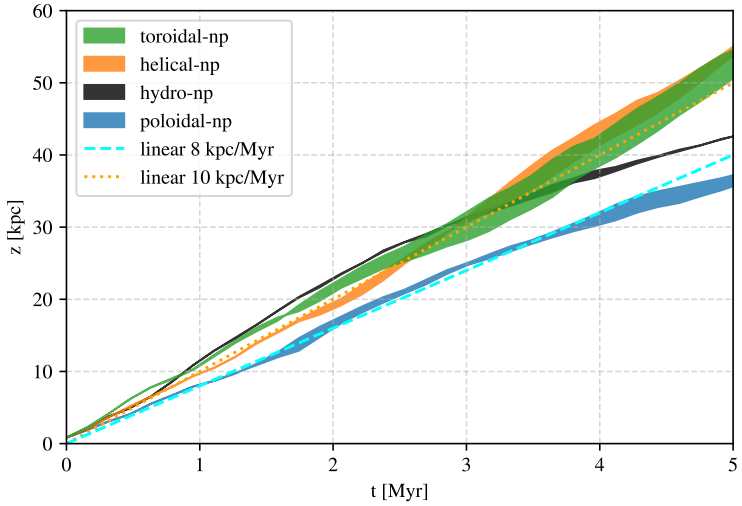

Figure 2.7 : Propagation distances of the jet heads for the 4 non-precessing jets. The edges of the filled region represent the longest extension of the jet fluid in the +z and -z directions for simulations without precession. Dotted and dashed lines: linear propagation rate for comparison. Note that the jet fluid is set to a velocity of 0.1 $c \sim$ 30 kpc/Myr in our simulations.

the magnetic structure determines the later evolution of the jet. It is clear that the jet in the toroidal case (green line) maintains the highest density as it propagates, while the jet in the poloidal case drops to very low density as soon as the fluid leaves the nozzle. Two reference lines of constant head velocity v_h are plotted in Fig. 2.7: 8 and 10 kpc/Myr for density ratio η of 0.12 and 0.23 respectively.

Given how the magnetic fields work, we would expect that the toroidal jet propagates fastest due to the hoop stress imposed by the toroidal magnetic fields on the flow. The toroidal fields collimate the jet, compress the flow, and increase the density, enabling the fluid to penetrate faster in the ICM. On the other hand, the poloidal magnetic fields act as additional radial pressure that expands the jet and reduces the density, making it slower

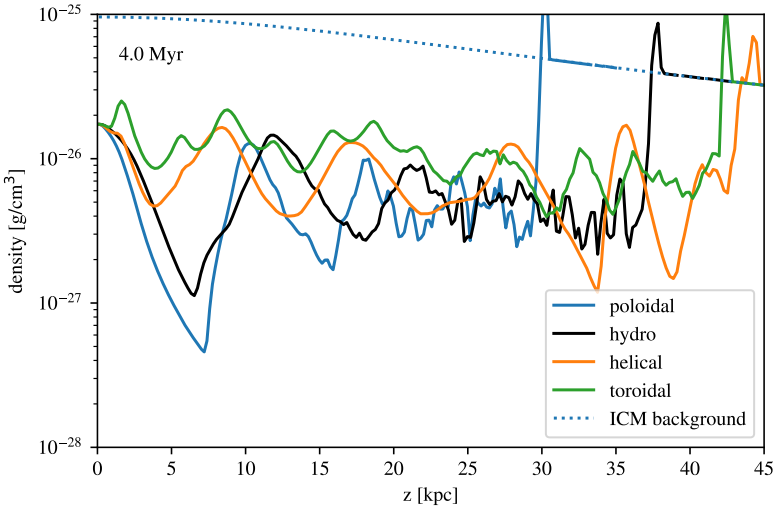

Figure 2.8 : Averaged density profile within 0.25 kpc from the axis of the non-precessing jets at 4 Myr. All simulations begin with the same density in the nozzle, but the different configurations of the magnetic fields give rise to different density profiles after the jet fluid leaves the nozzle. This causes the different propagation velocity of the jet heads in our four cases.

to propagate.

However, the high density and degree of collimation of the toroidal case do not consistently make the toroidal jet propagate the fastest. As seen in Fig. 2.7 and the right panel of Fig. 2.6, the helical jet propagates as fast as the toroidal jet at a later time ($\gtrsim 3$ Myr). We investigate this conflicting behavior and find that the pure toroidal field leads to the development of MHD instabilities, which we will describe in detail in Section 2.4.1.

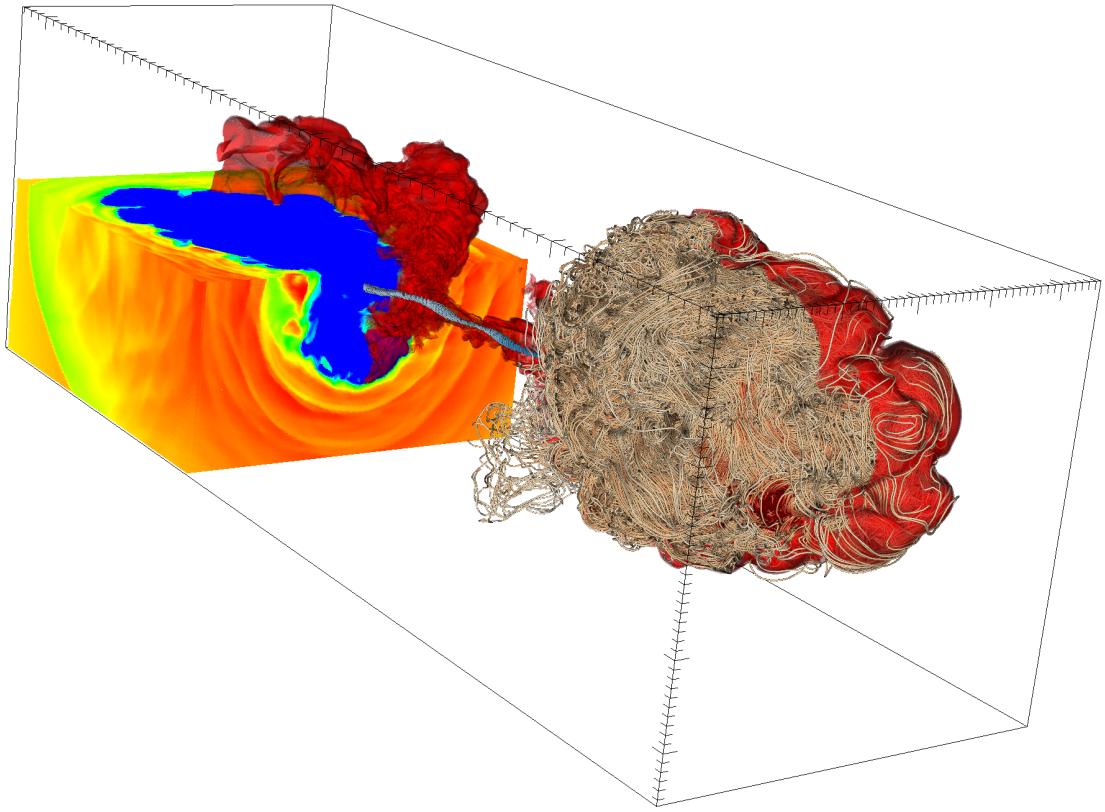

Figure 2.9 : 3D rendering of a simulation snapshot with helical magnetic fields in the jets. At left, slices show the temperature map (hot in blue and cold in red). At right, streamlines of magnetic fields represent the magnetic structure inside the lobe. Although the magnetic fields are highly ordered in the jet, they become mostly tangled in the lobe.

2.3.2 Dynamical Properties

When jitter is implemented (Section 2.2.4), the shapes of the cavity look very different from the non-precessing jets. The cavities created by the jets resemble the lobes of typical FR-II radio galaxies (Fanaroff & Riley 1974). Some typical examples include Cygnus A, Centaurus A, Fornax A and Hydra A. In Fig. 2.10, we show the central slices of the four simulations at about 10 Myr. The jets have been continuously on for 10 Myr, injecting hot and low-density plasma in the ICM, creating cavities and cocoons. The shapes of the toroidal and helical cases are different from the poloidal and hydro cases. When toroidal fields are included in the jet (both toroidal and helical cases), the cavities are more elongated, with larger aspect ratios, compared to those without toroidal fields (poloidal and hydro cases).

To quantify the differences in propagation, we measure the extent of the lobes from

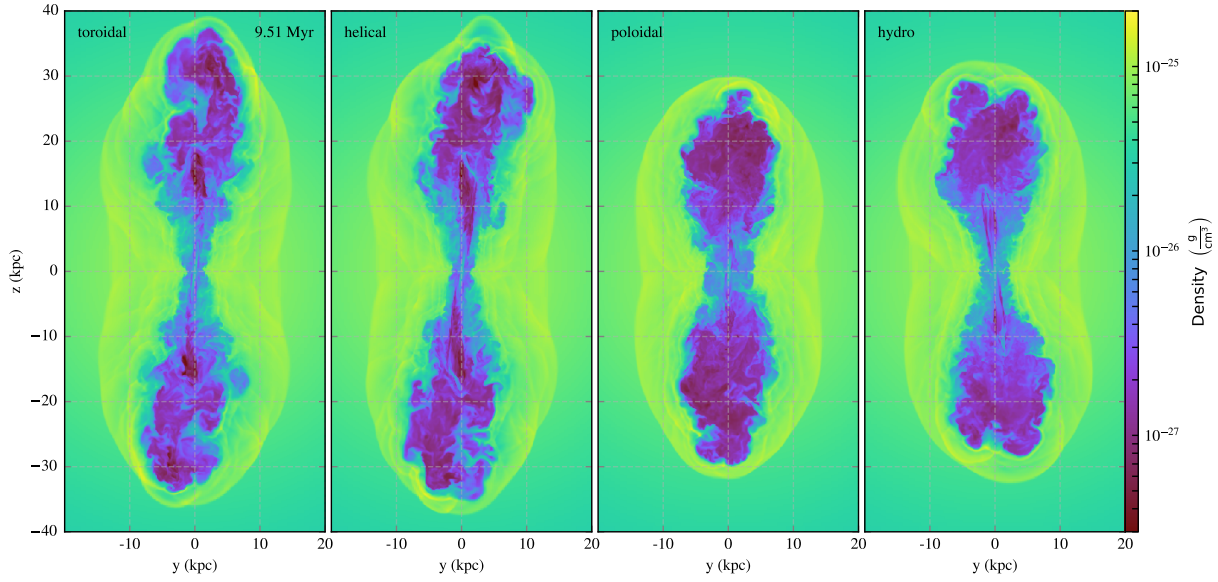

Figure 2.10 : Slices showing the density through the central plane from four simulations with different magnetic field topology in the jets at 10 Myr. From left to right: pure toroidal, helical, poloidal, no magnetic field.

our simulations similar to what we have done in the non-precessing cases (Section 2.3.1). The location of the jet heads is plotted in Fig. 2.11. At the very early stage (< 1 Myr), we see the sequence of toroidal $>$ hydro $\gtrsim$ helical $>$ poloidal in lobe sizes. However, after 1 Myr the toroidal case slows down to be comparable to the helical case, and the hydro case slows down to be comparable to the poloidal case. At 10 Myr, the time shown in Fig. 2.10, they form two distinct groups with toroidal $\sim$ helical $>$ hydro $\sim$ toroidal.

The behavior can be viewed in conjunction with the non-precessing cases in Section 2.3.1. The toroidal and helical cases, given the action of magnetic hoop stress, can collimate better and carry more ram pressure during the propagation, resulting in the cavities being more elongated. On the other hand, the poloidal and hydro cases lack the collimation

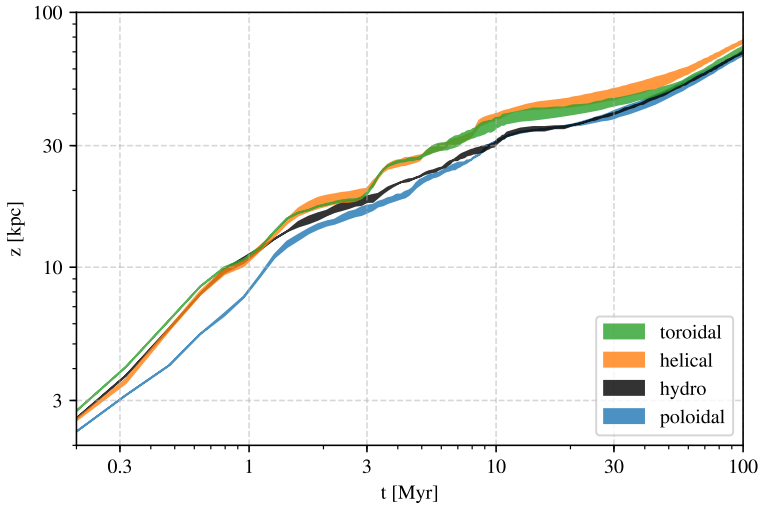

Figure 2.11 : Evolution of the lobe extent in the four precessing simulations. Edges of the shaded area represent the furthest extents of the jet fluid in +z and -z directions, representing two sides (upper and lower) of the jets and can be interpreted as numerical uncertainties in the simulations. The jets are turned off at 10 Myr. Note that both axes are in log-scale.

mechanism and propagate more slowly.

However, the pure toroidal case does not show significant differences in the cavity shape compared to the helical case. This is in contradiction to the understanding that the propagation velocity is determined by the collimation of the jet and thus by the strength of toroidal fields. We have seen similar results in the non-precessing case, in which the propagation of the pure toroidal case slows down to be comparable to the helical case. We attribute this to the development of MHD instabilities and will discuss in further details in Section 2.4.1.

In the hydrodynamic case, in which magnetic fields are absent, we can see more Kelvin-Helmholtz (KH) instabilities developing at the boundaries of the cavity. The magnetized jets and lobes suppress the KH instabilities at the shearing boundaries. This is consistent with previous findings that magnetic fields can suppress the instabilities (see e.g. Ryu et al. 2000; Jones & De Young 2005).

2.3.3 Synchrotron Properties

With the implemented tracer particles, we can synthesize the synchrotron radiation at various frequencies of different evolutionary stages for different magnetic injection topologies. We show in Fig. 2.12 the synchrotron emission maps at 150 MHz. In the early stages, due to the precession of the jets, the shape of the radio image is spiky with various episodes of the jet rapidly propagating into the ambient medium as jitter changes the jet direction. The emission is brightest at the endpoints of the spikes, where the jet fluid runs into the denser medium and decelerates. These locations correspond to the hotspots seen in many of the FRII objects. At later time, after around 10 Myr when jets are off, more rounded shapes of the radio emission emerge due to the expansion of the hot jet fluid.

After the end of the jet activity and energy injection, the inflated bubbles rise

buoyantly and form vortices (see e.g. Churazov et al. 2001; Gardini 2007; Churazov et al. 2013). If viewed from an inclined angle (Fig. 2.13), a synchrotron emitting torus is visible at 100 Myr in each simulation. This is similar to the mushroom clouds seen after an energetic explosion on earth. As proposed by Churazov et al. (2001), the torus is formed due to the low-density hot gas rising in the stratified cluster atmosphere. The shape of the torus very much resembles the morphology of Fornax A (Fomalont et al. 1989; Anderson et al. 2018), which has passively evolved for at least 100 Myr and does not show any hotspots.

A common indicator of the plasma age of the synchrotron emitting medium is the spectral index, which depends on the injection index as well as the cooling history. We calculate the projected emissivity at two frequencies based on the *particle* aging model described in Section 2.2.5 and 2.2.6. The spectral index between two frequencies is then $\alpha = \log(I_{\nu_1}/I_{\nu_2})/\log(\nu_1/\nu_2)$. The results are shown in Fig. 2.14. A gradient from the flatter spectra at the heads to the steeper spectra at the tails is apparent in the figure when the jet is still active (< 10Myr).

The synchrotron cooling tracer particle implementation adopted for these figures assumes that the electron distribution is a fresh power-law at the working surface/termination shock, where the bulk velocity of the plasma drops and the bulk of the jet kinetic energy is dissipated in a strong shock, motivating our assumption that the synchrotron emitting plasma is accelerated in these termination shocks. This results in a young and relatively flatter spectrum ($\alpha \sim 0.5$) at the hotspots. Thus, when the jets are still active, the tips of the lobes generally show flatter spectra compared to the lower regions closer to the AGN sources. Note that we explicitly filter out the emission from the jets. In actual observations, the removal of the active jet component might be crucial to reveal this gradient.

After leaving the hotspots, the plasma starts to cool and form a steeper spectrum toward the tail of the lobes. After the jets turn off, the plasma gradually becomes mixed

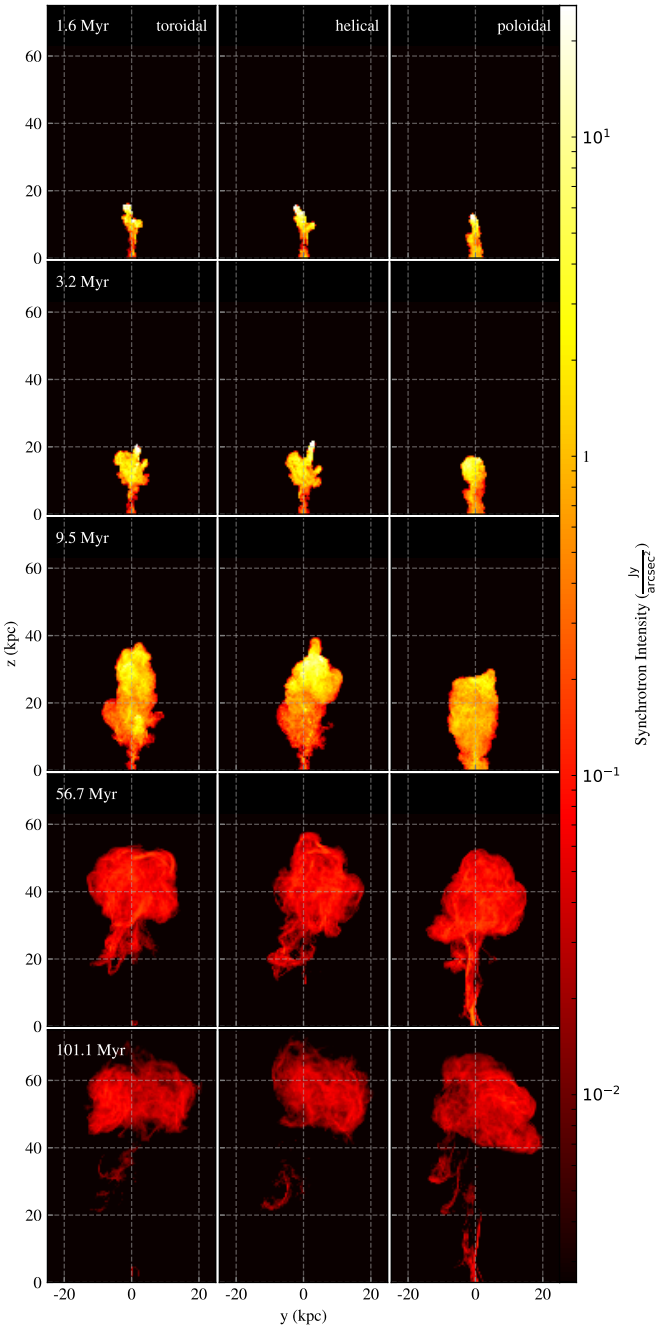

Figure 2.12 : Evolution of synchrotron emission at different times in the simulations. *Left* column: toroidal magnetic fields; *middle* column; helical magnetic fields; *right* column: poloidal magnetic fields.

and even shows a *reversed* age gradient at some particular times. This is due to the vortex structure formed during the rising of the bubble. The back-flow of the vortex brings the young plasma down to the edge of the tails, and the old plasma rises faster in the center. At an even later time ($\sim$ 100 Myr), the lobes do not show significant gradients. This reverse age effect can be important when searching for and analyzing fossil radio plasma in X-ray cavities of galaxy clusters. We will discuss this in more details in Section 2.4.3.

The radio lobes in the poloidal case, compared to helical and toroidal cases, have

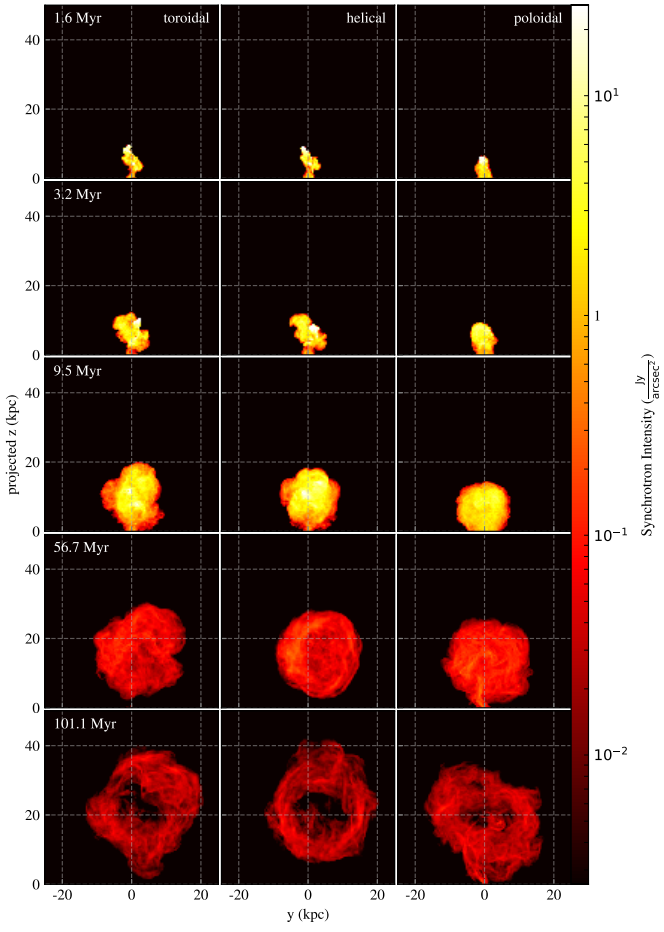

Figure 2.13 : Same as Fig. 2.12 but viewed from a 30-degree inclination angle relative to the jet axis. Notice that the radio emitting plasma has a torus shape in all 3 cases that are obvious in an inclined angle.

relatively flatter spectral indices among the 3 magnetized cases. This can be seen in Fig. 2.14, where the poloidal case has generally redder false color at every stage. This effect is caused by the overall weaker magnetic field in the poloidal field case. The cooling rates in the poloidal case are thus relatively slower, yielding both weaker emission and flatter spectra when compared to the other 2 cases at the same time. On the other hand, the helical case has the steepest spectral index because of the stronger magnetic fields. Note that although we inject more magnetic flux in the toroidal case, it does not have the strongest magnetic fields because of the onset of the kink instability and the resulting numerical reconnection discussed in Section 2.4.1. For the poloidal case, even though we begin with the same magnetic field strength in the nozzle, the expansion of the jet quickly makes the field much weaker as shown in Fig. 2.22.

2.3.4 Polarization Properties

Using the methods described in Section 2.2.7, we calculate the Stokes Q and U emissivities for each cell in the simulation domain. The projected Stokes Q and U maps are obtained by integrating along the line-of-sight. We then use the projected Stokes parameters to calculate the fraction and orientation of the polarization. An example of the polarization maps are shown in Fig. 2.16 for three simulations. We rotate the line segments by 90 ° to show the inferred direction of the magnetic fields.

Qualitatively, most of the orientations of the magnetic fields derived from the polarization follow the structure of the emitting medium. They are mainly parallel to the lobe *boundaries*. This can be understood both by the stretching of magnetic fields along the filamentary structure at the edges, and the reduced stochastic depolarization due to the shorter path length along the edges. Our results are in agreement with VLA observations of radio galaxies (e.g. Bridle et al. 1994). The high-resolution polarization

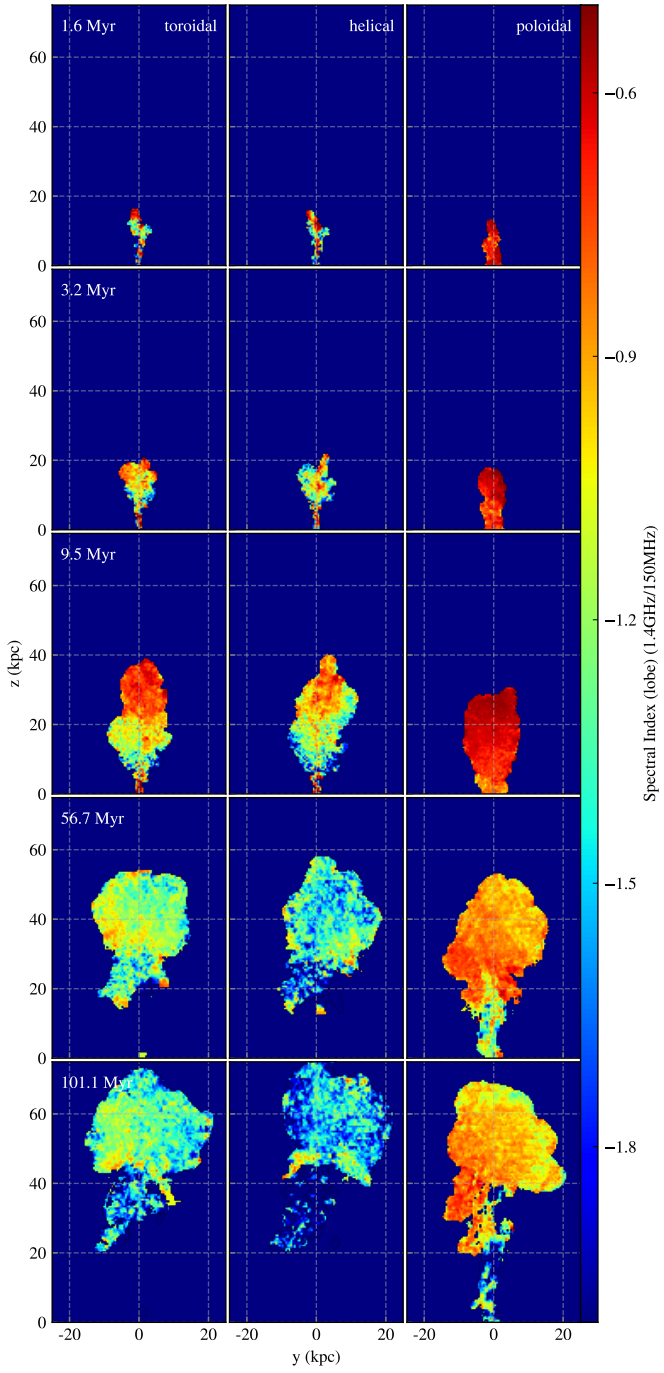

Figure 2.14 : Evolution of synchrotron spectral index at different times in the simulations. The spectral index α is calculated as $\alpha = \log(I_{\nu_1}/I_{\nu_2})/\log(\nu_1/\nu_2)$. In this figure, $\nu_1 = 1400$ MHz and $\nu_2 = 150$ MHz. *Left* column: toroidal magnetic fields; *middle* column; helical magnetic fields; *right* column: poloidal column.

study of Cygnus A (Perley, R. A.; Carilli et al. 1996) and Pictor A (Perley et al. 1997) shows detailed magnetic field orientations following the boundaries, filaments, and loops.

To evaluate whether it is possible to infer the properties of lobe and jet magnetization from polarization properties of radio sources, we plot histograms of the polarization angle distributions in Fig. 2.18. Position angle 0 means the magnetic fields inferred by the polarization is parallel to the jet-axis (z-axis). The histogram is calculated based on pixels and weighted by the polarized intensity. We clearly see a trend that in the poloidal case,

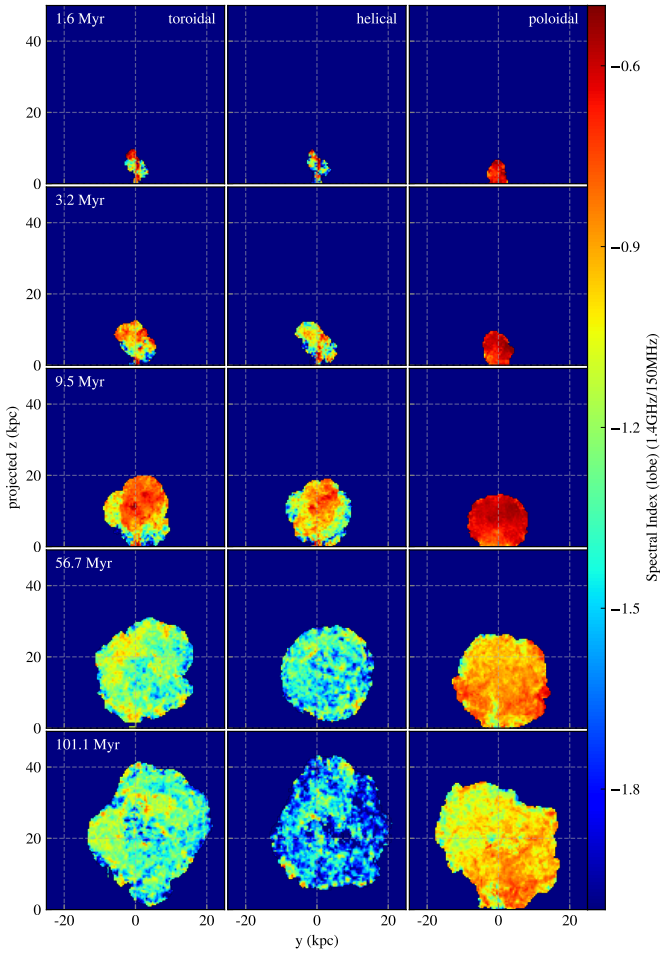

Figure 2.15 : Same as Fig. 2.14 but viewed from 30-degree inclination relative to the jet axis

the distribution of angles concentrates toward 0. This is consistent with the fact that only parallel fields are initially present in the poloidal simulation. The excess of position angles parallel to the jet axis is apparent from the early stages and becomes very significant at 50 Myr. However, this feature disappears at a much later time, as seen in the bottom panel of Fig. 2.18 at 100 Myr.

If the radio source is observed at an inclined angle, the excess of position angle parallel to the jet axis is no longer apparent. In Fig. 2.19, we show the same histogram

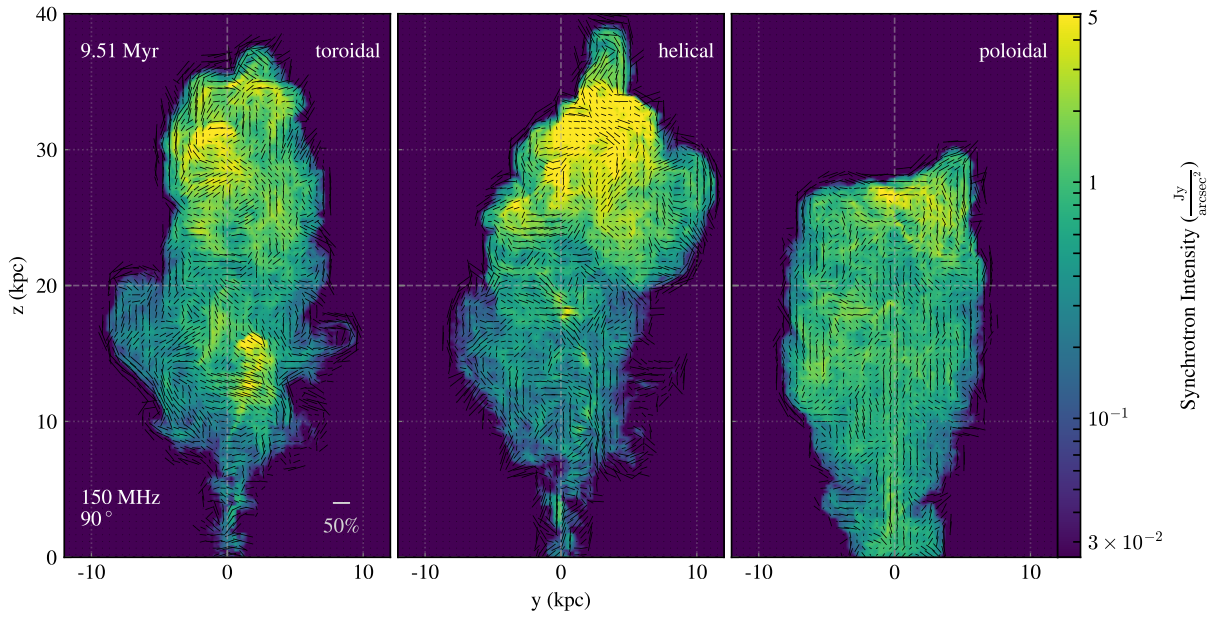

Figure 2.16 : Synthesized synchrotron intensity with line segments denoting the projected magnetic field orientations derived from the integrated Stokes Q and U parameters in the simulations. The length of the segment indicates the percentage of polarization. The line-of-sight is perpendicular to the jet-axis. Most of the magnetic orientations seem to follow the intensity structure. Note that since the polarization of synchrotron emission is perpendicular to the direction of the magnetic fields, we show the magnetic field direction by rotating the polarization angle by 90 degrees.

of the position angle for the synthesized observation at 30 degrees to the jet axis. In this case, the 3 simulations do not show a significant difference from each other. We can infer that the projected magnetic fields do not have a preferred orientation in this radio source, which indicates that the magnetic fields are not only parallel to the jet axis but mostly tangled, as revealed in the rendering (Fig. 2.9).

In Fig. 2.20, we plot the polarization spectra, that is, histograms of the polarization fraction at different frequencies, weighted by the total intensity. We can see that the general trend is that higher frequencies have higher fractions. This can be understood by the volume filling factor of the emitting gas. At higher observed frequency, we only see the young particles emitting radiation. There are fewer regions along the line-of-sight that contribute to the emission. Since the magnetic fields in the lobes are mostly tangled in our simulations, the smaller numbers of emitting regions will result in less depolarization, i.e., a higher polarization fraction. This effect is most prominent when the cooling frequency of the source matches the observing frequency.

The median value of the polarization fraction is plotted in Fig. 2.21. The overall median polarization fraction is high at an early time (t=3.2 Myr), reaches minimum during

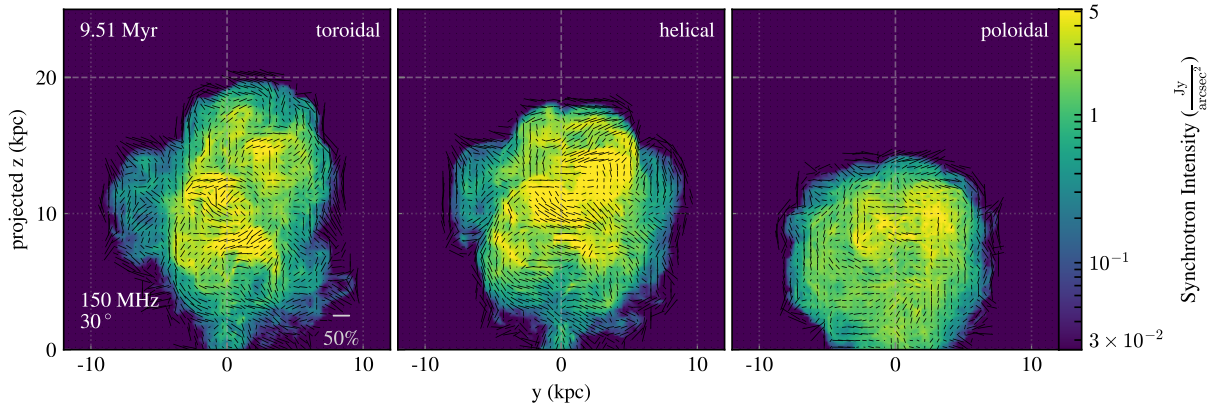

Figure 2.17 : Same as Fig. 2.16, but view at 30-degree inclination to the jet-axis.

the active phase of the jet (t=9.5Myr), and keep increases after the jet is off (57 and 101 Myr). The slope becomes steeper at later times since more particles have cooled so that their cutoff frequencies are below the observed frequency. Although the polarization of radio sources is affected by many other factors, e.g. cluster or foreground medium, the feature of the increasing slope might be worth looking for in high-resolution polarimetry.

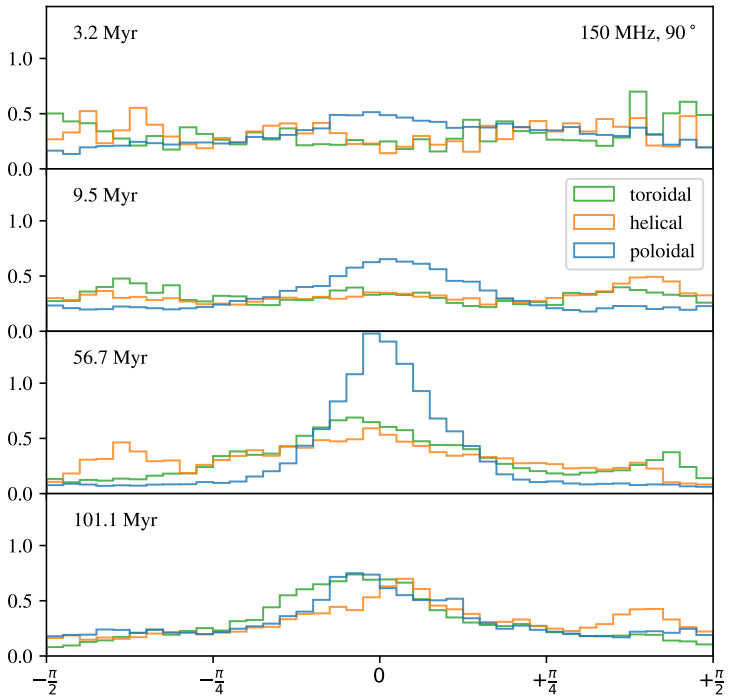

Figure 2.18 : Histogram of the synchrotron polarization position angles weighted by the polarized intensity at different times in the simulations. The line-of-sight is perpendicular to the jet axis. 0 means the magnetic fields are parallel to the jet-axis. The histogram of 150 MHz emission is shown here, and other frequencies have similar trends.

2.4 Discussions

2.4.1 Magnetic Field Strength and Kink Instabilities

We found in our simulations that the helical case becomes fastest at the later stage even though it starts slower. Also, the helical case maintains the highest total magnetic energy among all three magnetized cases, while the poloidal case has the lowest.

Magnetic energy injection occurs differently for the different cases: For the poloidal

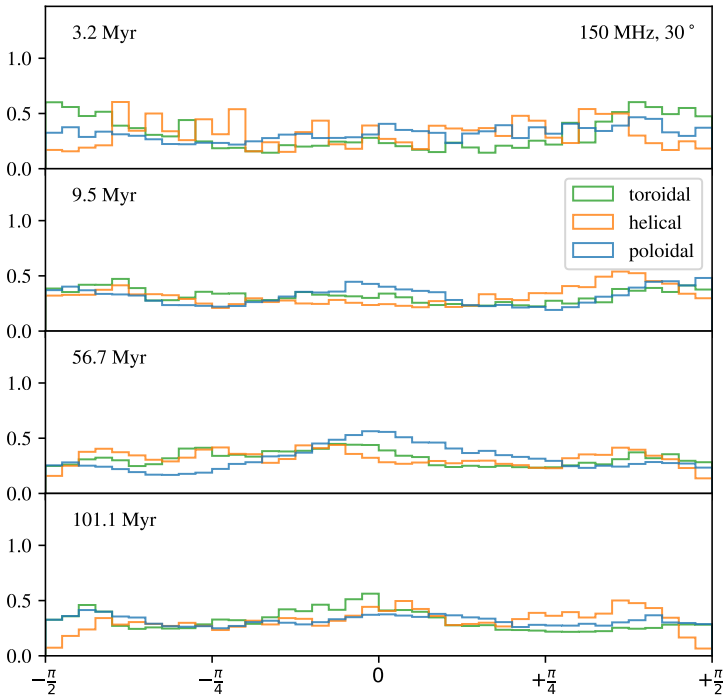

Figure 2.19 : Histogram of the synchrotron polarization position angles weighted by the polarized intensity at different times in the simulations. The line-of-sight is inclined 30° to the jet axis. 0 means the magnetic fields are parallel to the jet-axis. The histogram of 150 MHz emission is shown here, and other frequencies have similar trends.

case, the initial dipole field is stretched and amplified and no additional magnetic flux is injected in the simulation domain. On the other hand, we inject additional toroidal magnetic flux into the domain for the toroidal and helical cases.

Due to the lateral expansion of the jets, the toroidal (ϕ) component scales as $1/r$ while the poloidal (z) component scales as $1/r^2$. For initially comparable fields in toroidal and poloidal components, once the jet expands, the toroidal component will dominate the overall magnetic field *in the jet*.

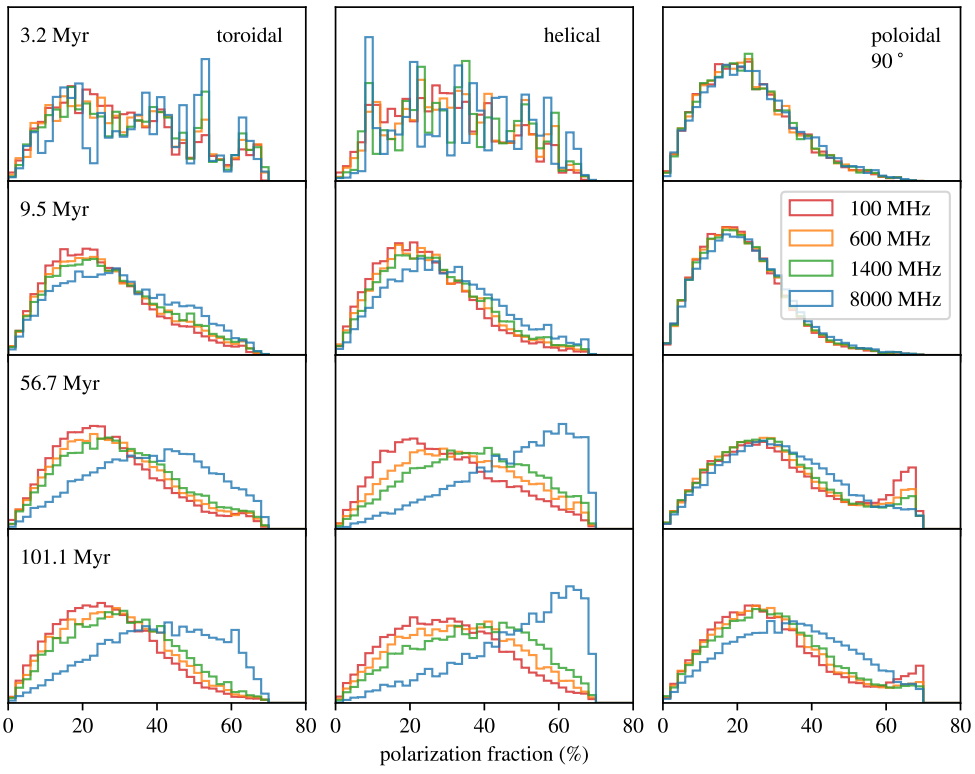

Figure 2.20 : Histogram of the synchrotron polarization fraction weighted by the intensity at different times in the simulations. *Left* column: toroidal magnetic fields; *middle* column; helical magnetic fields; *right* column: poloidal column.

In the lobes, magnetic fields become mostly tangled due to the turbulent motions. This can be seen in the rendered image in Fig. 2.9 as well as the evolution of different magnetic components in Fig. 2.22. In order to investigate the evolution of the magnetic field, we measure the magnetic energy of the (r, z, ϕ) components in cylindrical coordinates. In the non-precessing cases (denoted "np"), the ϕ component is maintained at a high level for both toroidal and helical cases, while in the precessing cases, the ϕ component is no longer dominant energetically. Rather, the different components are comparable to each other, especially around and after 10 Myr when the jet is turned off as shown in the right panel of Fig. 2.22.

The long-term behavior of the helical and the purely toroidal configuration require further discussion. We find that the counterintuitive behavior described above can be explained by the action of the kink instability, which can account for the field decrease in the toroidal case. This can be clearly seen in Fig. 2.23. The toroidal (ϕ) field in the toroidal

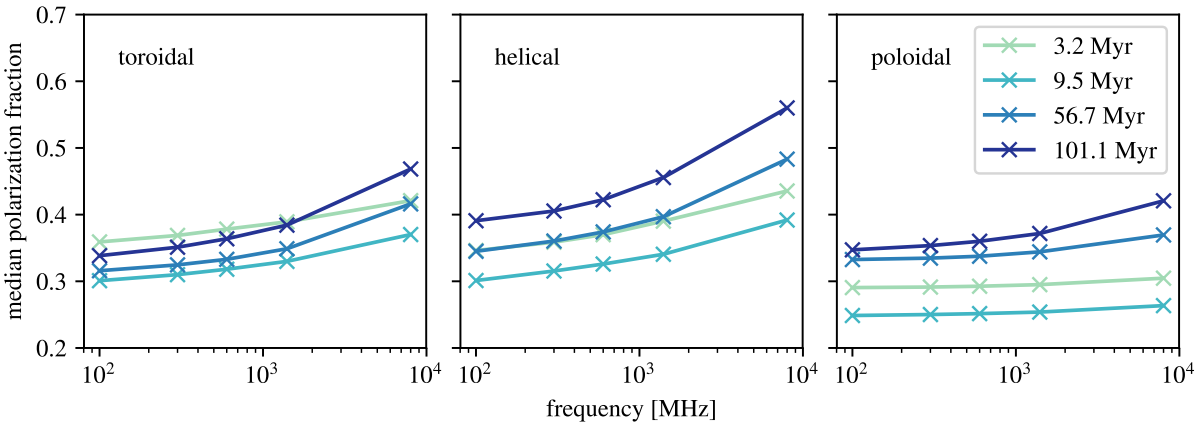

Figure 2.21 : Relationship between median polarization fraction and frequency at different times in the simulations. Higher frequencies have higher polarization fraction, and the slope increases with time as more young plasma has cooled. The increasing slope might be an indicator of the age of radio sources.

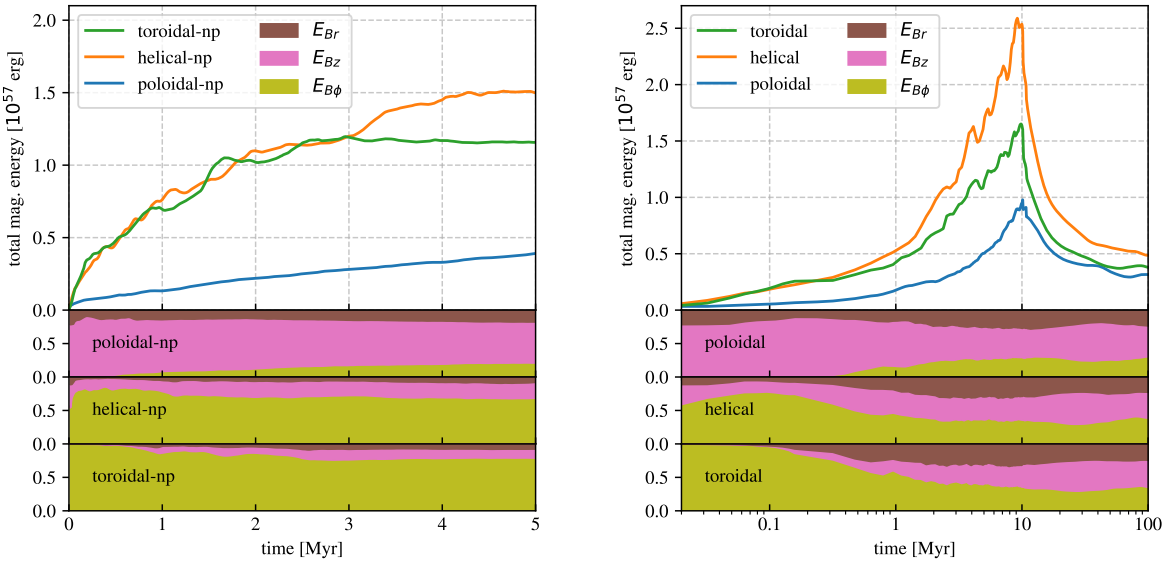

Figure 2.22 : Evolution of the magnetic energy and different components of the magnetic energy in the simulations. Different colors denote different magnetic configurations of the injection nozzle of each simulation. Solid lines indicate the total magnetic energy, while the filled charts show the percentage of the r, z, and ϕ components. *left panel*: non-precessing simulations (denoted "np"). Although in toroidal case more magnetic flux is injected in the domain, at later times the amount of magnetic energy is surpassed by the helical case. The poloidal case remains the lowest in magnetic energy. *right panel*: precessing jets active for 10 Myr. The magnetic energy decreases after the jet is off due to (mostly numerical) reconnection in the lobes. Note that at later times (after 10Myr), the z component increases, which is likely caused by the buoyantly rising bubble stretching the magnetic fields vertically.

case, although initially stronger than in the helical case, suffers from dynamical disruption and subsequent numerical dissipation due to the kink modes that become non-linear along the jet.

Appl et al. (2000) pointed out that current-driven instabilities are important in astrophysical jets and carried out linear stability analysis of the growth rates. They found that the growth rate depends on the radius of the jet, the Alfvén velocity, as well as the magnetic pitch $P = rB_z/B_\phi$. When normalized by the Alfvén crossing time ($r_{\rm jet}/v_A$), the growth rate is inversely proportional to the pitch or third power of the pitch depending on small or large pitch regimes. Larger pitch leads to a lower growth rate, i.e. the kink instability is suppressed. Although in our simulations the pitch profile is different from the analyzed profiles in Appl et al. (2000), we can still compare our instability growth rate to their calculations.

First, we consider the toroidal case, which should have a magnetic pitch close to zero and develop instabilities very quickly. However, we do not see the growth of the instability until the jet reaches beyond 18 kpc (Fig. 2.23). This can be accounted for by the numerical resolution required to resolve the unstable modes in our simulations. Roughly speaking, the minimum wavelength that can be resolved and thus grow in the simulation is about 4 cell-widths, which is about half of the jet radius. The maximum wavenumber that can be resolved is then $k_{\rm max} = 2\pi/\lambda_{\rm min} \sim 12/r_{\rm jet}$. The growth time of this unstable wavenumber is about $3r_{\rm jet}/v_A$ (c.f. Fig. 3 in Appl et al. (2000)) or ~ 0.2 Myr given $r_{\rm jet} \sim 240$ pc and $v_A = 0.012c$ in our simulations. The jet fluid is moving at 0.1 c in our simulations, which gives an instability e-folding length scale of 6 kpc. The instability becomes visible at about 3 times of this length scale.

Second, we consider the helical case, in which the jet has magnetic pitch of order of 1 ($P/r_{\rm jet} \simeq 1$). From Fig. 3 in Appl et al. (2000), we can infer that the maximum growth

rate is about 0.1 ($\Gamma r_{\rm jet}/v_A \sim 0.1$) and thus the e-folding growth time is of order 10 Alfvén crossing times ($t = 1/\Gamma = 10\, r_{\rm jet}/v_A$), which is roughly 0.8 Myr in our cases. Considering the jet fluid is 0.1 c, this timescale corresponds to a length scale of 24 kpc. We would expect the instability to become apparent at 3 or 4 times of this length scale. This can explain why there is no visible instability for the helical jet in Fig. 2.23.

This is similar to the findings of previous works (Nakamura et al. 2007; Guan et al. 2014; Bromberg & Tchekhovskoy 2016; Barniol Duran et al. 2017) that if the ratio between toroidal and poloidal fields is large, internal kink modes will develop and disrupt the jets. Due to the limit of our numerical resolution, the kink instability drives numerical reconnection at the core of the jet.

In Bromberg & Tchekhovskoy (2016); Barniol Duran et al. (2017), the authors

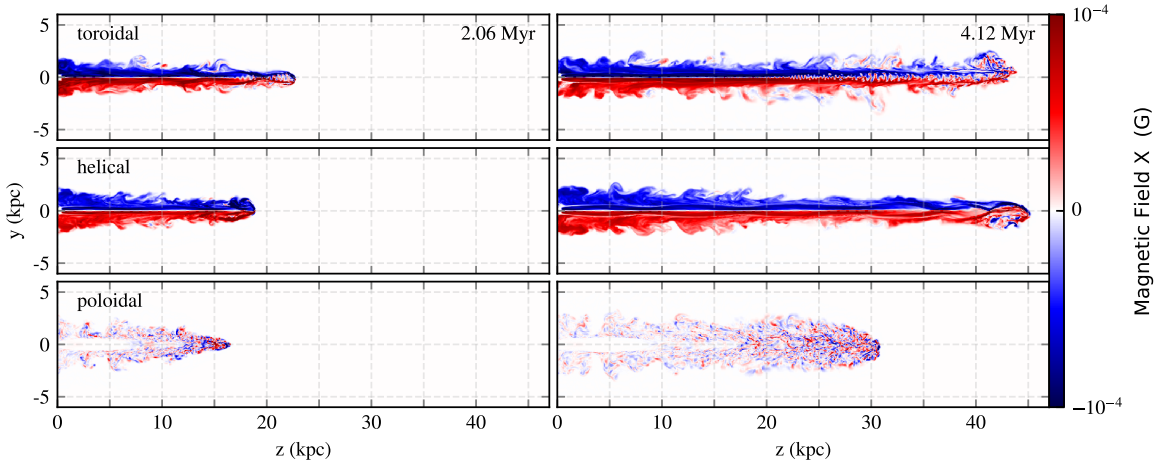

Figure 2.23 : Central slices of the magnetic fields in the x-direction (perpendicular to the image plane). In the toroidal case, kink instabilities start to develop after 15 and 20 kpc at 2 and 4 Myr respectively. Due to the limited resolution in our simulations, the instabilities result in magnetic energy being converted to thermal energy. Thus, it reduces the jet head propagation velocity of the toroidal case at later times.

attribute the development of the kink instability to the external medium density profile since the pitch angle of their jets depends strongly on the external medium. They argue that the jets propagating in denser external medium (headed jets) suffer from the kink instability, while the jets propagating in the less dense medium or a previously evacuated funnel (headless jets) can maintain their stability. Various factors, e.g. the spin of the central black hole, can change the magnetic pitch. In this work, we show that even in the same density profile, different magnetic pitches can still result in varying growth rates of the kink instability.

2.4.2 Comparison to Cygnus A

Given the obvious visual similarities, it is instructive to compare our synthesized radio maps with Cygnus A, the brightest and nearest powerful FR II radio source (Carilli & Barthel 1996). Although our simulations are not specifically modeled to resemble the Cygnus A cluster, the resulting radio maps have a lot of similarities to the observed properties of the typical FRII object, including the morphology as well as spectral index distribution (McKean et al. 2016).

In Fig. 2.12, single or multiple hotspots are visible when the jet is active (before 10 Myr). The misalignments between jet-axis and hotspots are natural results of the jittering implementation and mimic the two hotspots seen in Cygnus A (Pyrzas et al. 2014). While active jets are seen in Cyg A, we compare only the lobes with our synthesized image since we leave out most of the jet emission. At 50 Myr, more filamentary structures are developed, similar to Cygnus A. We note that the estimated age of the Cygnus A ranges from few Myr (Carilli et al. 1991) to 100 Myr due to the large uncertainties in the magnetic fields. Differences in structure could also arise from the different duty cycles of the source.

Our spectral index maps at 10 Myr show a strong gradient from the hotspot to the

tail of the lobe. The head of the lobe, where the plasma is freshly injected, has a flat spectrum with spectral index α close to 0.5, while the spectral index steepens toward the tail with $\alpha \sim 2$, where most of the plasma is old. This is consistent with the detailed observations of Cygnus A (Carilli et al. 1991).

2.4.3 Spectral index gradient evolution

In Section 2.3.3, we see a clear spectral index gradient while the jets are still active when the sources are observed close to perpendicular to the jet axis. During the active jet, at the time of 9.5 Myr, we see flatter spectral index or younger plasma located at the tips of the lobe, while the older plasma is at the tails close to the central plane. This gradient of the spectral index has been seen in many observations of FR-II sources (e.g. Steenbrugge et al. 2010; Shulevski et al. 2017; Savini et al. 2018). At a later time after the jet is off (roughly at 50 Myr in our case), a reverse gradient can be seen in the spectral index map. The relatively younger plasma is now at the tails of the lobe, while the tips appear to be older, as shown in Fig. 2.14.

If the viewing direction is closer to the jet axis, the spectral index is flatter in the center and gets steeper closer to the edges of the lobe while the jet is active, as shown in the third row (9.5 Myr) of Fig. 2.15. However, once the jets shut off, the distribution of the spectral index becomes again reversed – steeper at the center and relatively flatter closer to the edges, as in the 4th row (56.7 Myr) of Fig. 2.15.

The reversal can be understood as a consequence of the rotation of the rising bubble. Our radio sources resemble typical FR-II sources, in which the radio emission is brighter away from the central engine. The fresh young plasma appears in the vicinity of the hotspots which are located at the farthest ends of the radio lobes. While it is still not clear what acceleration mechanism powers FR-II sources — whether the relativistic electrons are

accelerated in the terminal shocks, i.e. the hotspots, or *in situ* in the jets —, those sources produce a spectral index (or age) gradient from flatter (younger) at the farther ends of the lobes to steeper (older) closer to the central source.

Two effects likely initiate the rotation. First, the injection of the jet creates a backflow toward the tail of the lobe, which has been pointed out and extensively discussed by several authors (Norman et al. 1982; Antonuccio-Delogu & Silk 2010; Cielo et al. 2017). Depending on the size and location of the cavity, backflows might reach back to the central plane where the supermassive black hole is located or circulate within the cavity. In our simulations, the helical and toroidal cases have cavities away from the central plane, while the poloidal and hydro cases show puffy cavities extending to the central plane (Fig. 2.10). Second, the buoyantly rising bubbles naturally develop vortices and cause the global rotation of the plasma in the bubble as the Rayleigh-Taylor instability emerges Churazov et al. (2001).

The result of the circulation within the bubble is a reversal of the age gradient that can be seen at roughly one eddy-turnover time after the jet comes to a stop, as shown in Fig. 2.24. This is an interesting phenomenon that has not been pointed out before. Currently, most of the observed FR-II sources exhibit age gradient from the head to the tail since most of the detected sources are higher luminosity objects whose powering jets are still active or have been active recently. Once the jet stops, the radio luminosity quickly drops at least an order of magnitude within a few Myr. Although these low-surface brightness radio sources are brighter at low frequencies, the inherently lower resolution at lower frequency might make the detection of the reversing effect more difficult.

However, we can also identify this effect by measuring the emission-weighted distance of the lobes from the core at different frequencies. The higher frequency emission will be further away from the core while the jet is active and remain so for some time after the jet turning off. In Fig. 2.25, we show the fractional offset between the synthesized

emission at 1400MHz and 100MHz. While the jet is active within the first 10 Myr, the offset fluctuates quickly, likely due to the hotspots moving across the lobe, but it generally stays positive. This positive offset, which indicates higher frequency emission being further away compared to lower frequency emission, diminishes after 60 Myr. The time is roughly when we observe the reversal of spectral index gradient, which is about one turnover time after the jet ceased.

Even though the occurrence of this effect might require stable environments and a long time between episodes of active jets, it might become more prevalent when high-sensitivity, lower-frequency radio observations become available in the near future when we will be able to detect low surface brightness and relatively old radio bubbles. If the observation has good enough resolution, we might be able to put constraints on the orientation of the jet axis based on the distribution of the spectral index.

2.4.4 Strength of the magnetic fields in the jet

In this work, we focus on the interaction of the jets with ambient gas, assuming most of the magnetic energy has been converted to kinetic energy at the boundaries of our injection nozzle roughly about 100 pc from the black hole. Indeed, Sikora et al. (2005) argue that, from observational data, the conversion of Poynting flux to kinetic energy happens mostly within 10^3 gravitational radii at parsec scale, which is consistent with our assumptions. Although the energy flux is dominated by the kinetic energy in our simulations, magnetic fields are still dynamically important at larger scales.

In our simulations, we do not set the strength of the magnetic fields explicitly. Instead, we choose the plasma beta β_p to be of order unity inside the jet nozzle, which implies that the magnetic pressure is comparable to the thermal pressure of the gas and is dynamically important. The field strength is then determined by our choices of jet power, internal Mach

number, and nozzle cross-section. We note the resulting magnetic field strength at the jet base ($\sim$ kpc from the black hole) is about 170 μG. While it is currently impossible to precisely infer the strength of the magnetic fields in the jets from observations, O'Sullivan & Gabuzda (2009) find the magnetic fields in the AGN cores are in the range of 100 $\sim$ 300 μG at 1 pc and scales like r^{-1}. Our setting of magnetic fields is consistent with their findings.

We would like to stress that in our simulations we adopt kinetic jets, in which the kinetic energy dominates over the thermal and magnetic energy. This accounts for the relatively minor differences between different magnetic topologies since the kinetic power

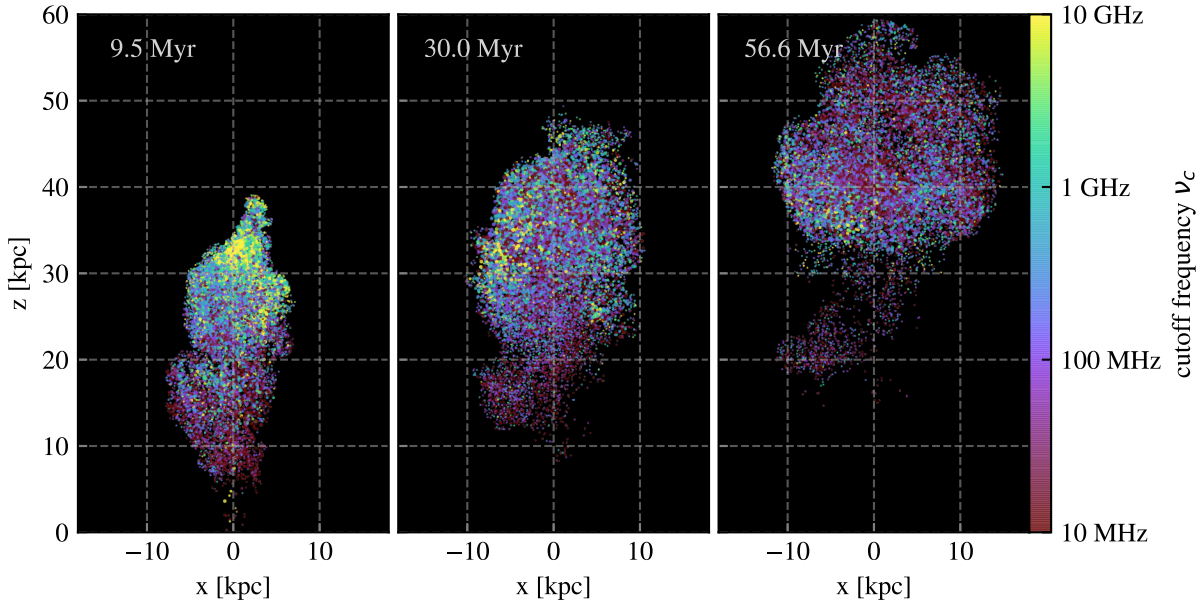

Figure 2.24 : The cutoff frequency of the *particles* at 3 different times of the helical case. The size of the points represents the local gas density– bigger points indicate lower density. While the jet is still active, We can see a clear gradient from the tip to the tail of the lobe. While the jet is off, part of the older plasma that was initially at the tail is lifted by the vortex to the top. This make a *reversed* age gradient at $\sim$ 60 Myr in our case.

is 10 times larger than the thermal and magnetic power.

2.4.5 On Spectral Aging Models

The spectral aging model commonly used in radio observations is usually simplified, using a single electron distribution, assuming equipartition between magnetic fields and electrons. Although the model can help us get an overall idea about radio galaxies, it often does not reflect the complexity and complicated structure of the radio lobes inflated by jets. In our model, we implement a realistic model of synchrotron cooling with self-consistent magnetic fields. We are able to trace the cooling of individual particles, which represent ensembles of relativistic electrons, to produce the synchrotron spectra. Combined with the magnetic fields, we can synthesize high-resolution and high-fidelity synchrotron intensity maps at any frequency.

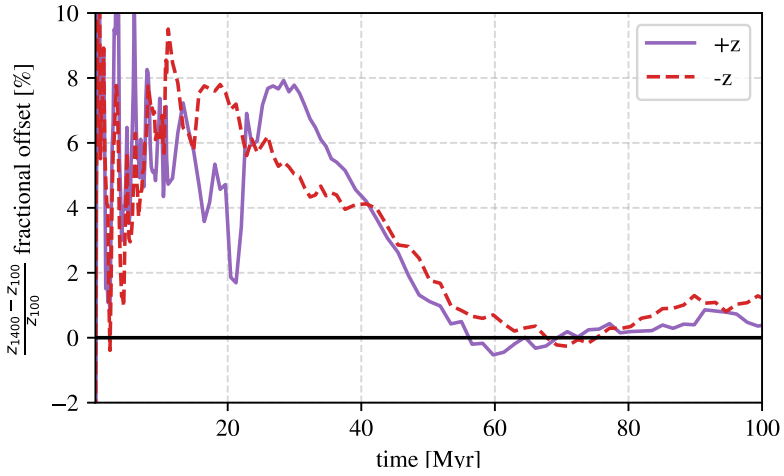

Figure 2.25 : Fractional offset of the weighted centers between 1400MHz and 100MHz. The emission weighted distance from the central AGN are calculated from two frequencies and the fractional difference is shown here. The offset is positive during time when the jet is active. It remains positive for roughly a turnover time and disappears after 60 Myr.

Conventionally, spectral aging models assume a constant magnetic field, which is usually derived from minimum energy arguments, to calculate the age of the radio source. However, as seen in our simulations, the magnetic fields that a particular plasma ensemble experiences along its trajectory are varying at different stages. In the hotspots where the fresh plasma begins to cool, the magnetic fields are strongest due to compression at the terminal shocks. When the plasma leaves the hotspots, the magnetic field strength significantly drops because of the adiabatic expansion of the plasma as well as reconnection of the highly tangled field. We note that this latter effect is enhanced in any numerical simulation because of limited resolution and numerical diffusivity.

As a consequence, the cooling rates in the lobes are much slower compared to the cooling rates in the hotspots. The evolution of the spectral index depends on the strength of the magnetic field. Although we begin with the same magnetic field strength in the nozzle, the resulting field varies due to a combination of the expansion and instabilities.

2.4.6 Constraints and Limitations of Our Simulation

The Lagrangian particles begin cooling after they leave the jet. Our current model does not capture any re-acceleration outside the hotspots. A more complex framework (e.g. Vaidya et al. 2018) is necessary to study various acceleration mechanisms and the resulting synchrotron emission.

In our current setup, the surrounding medium is non-magnetized. All the magnetic flux comes from the injection of the jet. Although this setup is obviously unphysical, we use our simulations to create a baseline for future studies in which more complicated factors might affect the dynamics of the jets and the bubbles. Some researches hint that the evolution of bubbles might be affected more by the surrounding magnetic field than by the field inside the bubbles (Ruszkowski et al. 2007; Dursi & Pfrommer 2008). We will leave

the investigation of jets interacting with magnetized surroundings to future work.

2.5 Conclusions

The motivation of this study is to address the following two questions: Will the topology of magnetic fields of the jets affect the large-scale radio lobes? Would it be possible to identify and develop diagnostics of the radio lobes to infer the magnetic field structure of the jets? Although ordered magnetic fields are most likely necessary to launch the jets, it has been uncertain whether the field topology can be maintained in radio lobes that could be few 100 kpc away from the source.

In this chapter we present a series of high-resolution MHD simulations of AGN jets with different injecting field topology. We set up pure toroidal, pure poloidal, and helical magnetic fields inside the jets (see Fig. 2.2). The jets are then evolved according to the ideal MHD formalism. Our jets are well-resolved compared to other simulations, making them suited to study the delicate magnetic field structure in the jets as well as the inflated lobes.

In this work, we do not discuss the origin of the magnetic field in the jets nor the mechanisms that determine the field topology in the jets. The existence of poloidal and toroidal components greatly increases the stability of the magnetic fields in the jets. In our simulations, the ratio between the poloidal and toroidal fields determines the large-scale and long-term evolution of the magnetic fields in the lobes and their morphology.

We demonstrate the role of magnetic fields in collimating the jet fluid by imposing hoop stress. The presence of toroidal magnetic fields prevent the jet from over expanding and enables faster propagation of the jet heads. On the other hand, the presence of poloidal fields is also vital in that the development of kink instability can be suppressed. Counter-intuitively, pure toroidal jets do not propagate faster than the helical jets. Instead, they

become comparable to the helical case and lose much of their magnetic energy through the instability. We find that toroidal and helical jets generate more elongated cocoons and the cavities inflated by the jets are further away from the central engine compared to pure poloidal and hydro jets.

After the jet fluid hits the heavy cluster medium, turbulent motions in the lobes, as well as the precession of the jets, lead to highly tangled magnetic topology in the lobes. We do not see large-scale organized field structures in the lobes. The field strength steadily decreases after the jet becomes inactive due to the numerical reconnection of the tangled fields and adiabatic expansion.

The simulations give us time-series data that are post-processed to create synchrotron maps that encompass information from the cooling of the jet plasma (from synchrotron tracer particles) and the orientation of magnetic fields (from grid cells). This allows us to construct Stokes I, Q, and U imaging at desired orientations and frequencies.

We show a reversal of the spectral index gradient after the jet shuts off due to the reciprocal motions of the young and old plasma in the rotating bubble. We find that the histogram of the polarization position angle can be a good indicator if the magnetic topology of the jet is pure poloidal. The polarization-inferred magnetic fields are more likely to be aligned with the jet-axis in the poloidal case. However, this feature vanishes as the line-of-sight changes toward the jet-axis. We also find that higher frequencies have higher polarization fractions in all cases due to smaller filling factors and thus lower depolarization. Future deep radio sky surveys, for example with SKA[3], may allow us to examine the sources with low-surface brightness and statistics of polarization in radio galaxies and help us determine the magnetic structure of the jets (Agudo et al. 2015).

[3]Square Kilometer Array, https://www.skatelescope.org/

References

Agudo, I., Boettcher, M., Falcke, H., et al. 2015, Proceedings of Advancing Astrophysics with the Square Kilometre Array (AASKA14), arXiv:1501.00420

Anderson, C. S., Gaensler, B. M., Heald, G. H., et al. 2018, ApJ, 855, 41

Antonuccio-Delogu, V., & Silk, J. 2010, MNRAS, 405, 1303

Appl, S., Lery, T., & Baty, H. 2000, A&A, 355, 818

Banfield, J. K., Wong, O. I., Willett, K. W., et al. 2015, MNRAS, 453, 2326

Barniol Duran, R., Tchekhovskoy, A., & Giannios, D. 2017, MNRAS, 469, 4957

Beckwith, K., Hawley, J., & Krolik, J. 2008, ApJ, 678, 1180

Beckwith, K., Hawley, J. F., & Krolik, J. H. 2009, ApJ, 707, 428

Bell, A. R. 1978, MNRAS, 182, 147

Bicknell, G. V., & Melrose, D. B. 1982, ApJ, 262, 511

Blandford, R. D., & Ostriker, J. P. 1978, ApJ, 221, L29

Blandford, R. D., & Payne, D. G. 1982, MNRAS, 199, 883

Blandford, R. D., & Znajek, R. L. 1977, MNRAS, 179, 433

Braithwaite, J. 2010, MNRAS, 406, 705

Bridle, A. H., Hough, D. H., Lonsdale, C. J., Burns, J. O., & Laing, R. A. 1994, AJ, 108, 766

Bromberg, O., & Tchekhovskoy, A. 2016, MNRAS, 456, 1739

Bugli, M., Del Zanna, L., & Bucciantini, N. 2014, MNRAS, 440, L41

Caprioli, D., & Spitkovsky, A. 2014, ApJ, 783, 91

Carilli, C. L., & Barthel, P. D. 1996, AAR, 7, 1

Carilli, C. L., Perley, R. A., Dreher, J. W., & Leahy, J. P. 1991, ApJ, 383, 554

Childs, H., Brugger, E., Whitlock, B., et al. 2012, in High Performance Visualization–Enabling Extreme-Scale Scientific Insight, ed. E. W. Bethel, H. Childs, & C. Hansen (Boca Raton, FL, USA: Taylor & Francis), 357–372

Churazov, E., Bruggen, M., Kaiser, C. R., Bohringer, H., & Forman, W. 2001, ApJ, 554, 261

Churazov, E., Ruszkowski, M., & Schekochihin, A. 2013, MNRAS, 436, 526

Cielo, S., Antonuccio-Delogu, V., Silk, J., & Romeo, A. D. 2017, MNRAS, 467, 4526

Coleman, C. S., & Bicknell, G. V. 1988, MNRAS, 230, 497

Del Zanna, L., Volpi, D., Amato, E., & Bucciantini, N. 2008, A&A, 453, 621

Dennett-Thorpe, J., Scheuer, P. A., Laing, R. A., et al. 2002, MNRAS, 330, 609

Drury, L. O. 1983, Reports on Progress in Physics, 46, 973

Dubey, A., Antypas, K., Ganapathy, M. K., et al. 2009, Parallel Computing, 35, 512

Dubey, A., Daley, C., Zuhone, J., et al. 2012, ApJS, 201, 27

Dursi, L. J., & Pfrommer, C. 2008, ApJ, 677, 993

English, W., Hardcastle, M. J., & Krause, M. G. H. 2016, MNRAS, 461, 2025

Fanaroff, B. L., & Riley, J. M. 1974, MNRAS, 167, 31P

Fomalont, E. B., Ebneter, K. A., van Breugel, W. J. M., & Ekers, R. D. 1989, ApJ, 346, L17

Fryxell, B., Olson, K., Ricker, P., et al. 2000, ApJS, 131, 273

Gabuzda, D. C., Knuettel, S., & Reardon, B. 2015, MNRAS, 450, 2441

Gardini, A. 2007, A&A, 464, 143

Guan, X., Li, H., & Li, S. 2014, ApJ, 781, 48

Guo, F., Liu, Y. H., Daughton, W., & Li, H. 2015, ApJ, 806, 167

Hardcastle, M. J., & Krause, M. G. H. 2014, MNRAS, 443, 1482

Heinz, S., & Begelman, M. C. 2000, ApJ, 535, 104

Heinz, S., Briiggen, M., Young, A., & Levesque, E. 2006, MNRAS, 373, L65

Jones, T. W., & De Young, D. S. 2005, ApJ, 624, 586

Laing, R. A., Riley, J. M., & Longair, M. S. 1983, MNRAS, 204, 151

Leahy, J. P., Bridle, A. H., & Strom, R. G. 1996, in Extragalactic radio sources: proceedings of the 175th Symposium of the International Astronomical Union, ed. R. D. Ekers, C. Fanti, & L. Padrielli, Vol. 175 (Bologna: Kluwer Academic Publishers), 157

Lee, D. 2013, Journal of Computational Physics, 243, 269

Li, H., Lapenta, G., Finn, J. M., Li, S., & Colgate, S. A. 2006, ApJ, 643, 92

Longair, M. S. 2011, High Energy Astrophysics, 3rd edn. (Cambridge, UK: Cambridge University Press)

Lyubarsky, Y., & Yuri. 2009, ApJ, 698, 1570

Marti, J. M., Mueller, E., & Ibanez, J. M. 1994, A&A, 281, L9

McKean, J. P., Godfrey, L. E., Vegetti, S., et al. 2016, MNRAS, 463, 3143

McKinney, J. C., & Blandford, R. D. 2009, MNRAS, 394, L126

McNamara, B. R., & Nulsen, P. E. J. 2012, New Journal of Physics, 14, 055023

Mendygral, P. J., Jones, T. W., & Dolag, K. 2012, ApJ, 750, 166

Miley, G. 2003, ARAA, 18, 165

Mimica, P., Aloy, M.-A., Agudo, I., et al. 2009, ApJ, 696, 1142

Morsony, B. J., Heinz, S., Brüggen, M., & Ruszkowski, M. 2010, MNRAS, 407, 1277

Nakamura, M., Li, H., & Li, S. 2007, ApJ, 656, 721

Nawaz, M. A., Bicknell, G. V., Wagner, A. Y., Sutherland, R. S., & McNamara, B. R. 2016, MNRAS, 458, 802

Nishiyama, S., Hatano, H., Tamura, M., et al. 2010, ApJL, 722, L23

Norman, M. L., Smarr, L., Winkler, K.-H. A. K.-H. A., et al. 1982, A&A, 113, 285

Norman, M. L., & Winkler, K.-H. A. 1985, Los Alamos Science, 38

Nulsen, P. E. J., David, L. P., McNamara, B. R., et al. 2002, ApJ, 568, 163

Obergaulinger, M., Chimeno, J. M., Mimica, P., Aloy, M. A., & Iyudin, A. 2015, High Energy Density Physics, 17, 92

O'Sullivan, S. P., & Gabuzda, D. C. 2009, MNRAS, 400, 26

Park, J., Caprioli, D., & Spitkovsky, A. 2015, Physical Review Letters, 114, 085003

Perley, R. A., Roser, H.-J., & Meisenheimer, K. 1997, A&A, 328, 12

Perley, R. A.; Carilli, C. L., Perley, R. A., & Carilli, C. L. 1996, in Cygnus A – Studay of a Radio Galaxy, Proceedings of the Greenbank Workshop, held in Greenbank, West Virginia, 1-4 May, 1995. (Cambridge University Press), 168

Porth, O., & Fendt, C. 2010, ApJ, 709, 1100

Pringle, J. E. 1996, MNRAS, 281, 357

Pyrzas, S., Steenbrugge, K. C., & Blundell, K. M. 2014, A&A, 574, A30

Roberts, D., Saripalli, L., Wang, K., et al. 2018, ApJ, 852, 47

Romanova, M. M., & Lovelace, R. V. E. 1992, A&A, 262, 26

Ruszkowski, M., Enßlin, T. A., Brüggen, M., Heinz, S., & Pfrommer, C. 2007, MNRAS, 378, 662

Rybicki, G. B., & Lightman, A. P. 1979, Radiative Processes in Astrophysics (Weinheim, Germany: Wiley-VCH)

Ryu, D., Jones, T. W., & Frank, A. 2000, ApJ, 10, 11

Savini, F., Bonafede, A., Brüggen, M., et al. 2018, MNRAS, 474, 5023

Scheuer, P. A. G. 1974, MNRAS, 166, 513

—. 1982, In: Extragalactic radio sources; Proceedings of the Symposium, 163

Shulevski, A., Morganti, R., Harwood, J. J., et al. 2017, A&A, 600, A65

Sikora, M., Begelman, M. C., Madejski, G. M., & Lasota, J. 2005, ApJ, 625, 72

Sironi, L., Petropoulou, M., & Giannios, D. 2015, MNRAS, 450, 183

Sironi, L., & Spitkovsky, A. 2014, ApJL, 783, L21

Steenbrugge, K. C., Heywood, I., & Blundell, K. M. 2010, MNRAS, 401, 67

Tchekhovskoy, A. 2015, in The Formation and Disruption of Black Hole Jets (Springer International Publishing Switzerland), 45–82

Tout, C., & Pringle, J. E. 1996, Mon. Not. R., 281, 219

Turk, M. J., Smith, B. D., Oishi, J. S., et al. 2010, MNRAS, 423, 3018

Vaidya, B., Mignone, A., Bodo, G., & Massaglia, S. 2016in (IOP Publishing), 012023

Vaidya, B., Mignone, A., Bodo, G., Rossi, P., & Massaglia, S. 2018, ApJ, 865, 144

Vernaleo, J. C., & Reynolds, C. S. 2006, ApJ, 645, 83

Young, A. J., Wilson, A. S., Tingay, S. J., & Heinz, S. 2005, ApJ, 622, 830

Zhuravleva, I., Churazov, E., Arévalo, P., et al. 2015, MNRAS, 450, 4184

Chapter 3

Radio Jets in Galaxy Groups – Sampling in Jet Powers and Environments

Abstract

Feedback from AGN is a potential mechanism to explain the stellar content of massive galaxies. We conduct simulations of AGN jets in group environments. Understanding the dynamics of the jets and how radio emission depends on the environment is key to the investigation of AGN feedback. We explore the parameter space of 3 different jet powers and four different environments, parametrized by the core radius r_c in the β-model, in this work. We improve the previously developed techniques to model the synchrotron emitting plasma by incorporating shock identification in the numerical simulation. We investigate the morphological dependence of radio emission on jet power and environment. We compare the observed relationship between jet power and radio luminosity to simulations and further reveal how this correlation depends on the environment and jet active time.

3.1 Introduction

Thanks to the availability of galaxy surveys, we now know that the population of galaxies forms two distinct groups on the color-magnitude diagram — a red sequence and a blue cloud (Bell et al. 2004). Galaxies in the blue cloud are generally young, less massive, and gas-rich, while galaxies on the red sequence are old, massive, and gas-poor (see e.g. Kauffmann et al. 2003; Baldry et al. 2004). Models of galaxy formation require some "feedback" mechanisms to prevent forming too many stars and some "quenching" mechanisms to quickly move galaxies from the blue cloud to the red sequence. Two feedback mechanisms are commonly assumed to explain the deficiency of star formation. Supernova and wind feedback, both from star formation itself, are invoked in the case of low-mass galaxies (Larson 1974; Dekel & Woo 2003). On the other hand, feedback from the central supermassive black hole is most commonly assumed to explain the high mass end (Bower et al. 2006; Fabian 2012; Kormendy & Ho 2013). Recent results indicate that AGN feedback is necessary over a wide range of galaxies (Su et al. 2019).

AGN are one of the important processes to regulate the star-formation rate and even expel the cold gas and prevent further star formation, especially in massive galaxies. AGN impact their host galaxy via gas interaction. The gas in the galaxies needs to cool from ionized gas to atomic gas and to molecular gas in order to form stars. AGN prevent the gas from cooling by heating or expelling the gas in their vicinity. In some cases, AGN could also have positive feedback (increase star formation rate) on local clumps in the host galaxies by inducing rapid cooling in compressed gas (see e.g. Antonuccio-Delogu & Silk 2008; Gaibler et al. 2012).

There has been little evidence for the connection between AGN feedback and the

decline of star-formation except for the most massive galaxies (see Heckman & Best 2014, for a review). Some observations show that there is a significant delay ($\gtrsim$ 200 Myr) between the starburst phase and the peak of the AGN signal based on optical line ratios (Wild et al. 2010; Yesuf et al. 2014).

The purpose of this work is to provide numerical models for radio galaxies spanning a substantial range of parameter space, including the jet powers, profiles of the gaseous halo and lobe sizes (jet active time). By understanding how radio lobes in galaxy groups evolve, we will be able to apply and compare the models with observations from the upgraded Giant Metrewave Radio Telescope (uGMRT) and the Jansky VLA (JVLA) radio telescopes. We expect to compare the calibrated age estimates from the radio observations with the star-formation history derived from the Mapping Nearby Galaxies at APO (MaNGA) project and determine how the radio AGN affects the formation of stars.

In this chapter, we focus on the numerical modeling of AGN jets in different environments and present preliminary results from the analysis of the simulation products. The connection between the AGN jets and star formation will be addressed in future work.

This work is organized as follows. We describe the methodology and techniques in Section 3.2. In Section 3.3, we present and discuss the results of the simulations. In Section 3.4, we summarize our findings.

3.2 Numerical Setup and Techniques

Here we describe the essential and relevant details of the simulation. Similar the techniques described in Section 2.2 in Chapter 2, we conduct full 3D ideal MHD simulations using `FLASH` (Fryxell et al. 2000; Dubey et al. 2009) with the unsplit staggered mesh scheme

(Lee 2013) and AMR. The density profile follows a β-model with various core radii.

$$\rho(r) = \frac{\rho_0}{[1 + (\frac{r}{r_c})^2]^{\frac{3}{2}\beta}}, \tag{3.1}$$

in which we vary the core radius r_c as detailed in Section 3.2.1. We use an isothermal temperature profile with T = 1 keV for all simulations. We set up helical magnetic fields in the jets and let the plasma β be 1 inside the jet nozzle. The surrounding gas is not initially magnetized. The velocity of the jets is set to 0.2 c to better model the relativistic jets as seen in observations[1]. The Mach number of the jets is set to 7.

The relationship between Mach number M_j, the density ρ_j, and the pressure P_j inside the jets is

$$M_j = \frac{v_j}{c_s} = v\sqrt{\frac{\rho_j}{\gamma_j P_j}}. \tag{3.2}$$

The power of the jets is determined by the velocity profile v_j, density ρ_j, pressure P_j, and the toroidal magnetic field B_ϕ

$$L = 2\int v_j \left(\frac{1}{2}\rho_j v_j^2 + \frac{\gamma_j}{\gamma_j - 1}P_j + \frac{B_\phi^2}{8\pi}\right) \cdot \mathrm{d}a. \tag{3.3}$$

Table 3.1 : Radius of the jet and the resolution of the simulation

designation	jet power [erg s^{-1}]	jet radius [kpc]	cell size [pc]
L430 (low-power)	1.0×10^{43}	0.130	16.2
L438 (mid-power)	6.3×10^{43}	0.324	40.5
L446 (high-power)	4.0×10^{44}	0.810	101.3

Given the Mach number, the radius of the jet is set such that the necessary pressure of the nozzle is in balance with the core of the galaxy profile. Thus, for different power of

[1]It would be best to have jets running at the speed of light, but the computational cost is beyond our capacity.

jets, the radius of the nozzle is different and the resolution is determined by the radius–16 cells across the diameter of the jet nozzle, as shown in Table 3.1.

Other than changing jet powers and background profiles, we made a few improvements on the synchrotron tracer particles compared to Chapter 2, particularly in the determination of shock and better modeling of the power-law index, informed from the shock strength. We will describe these implementations in Section 3.2.3.

3.2.1 Galaxy Group Environments

Except for 2 objects, there are no existing X-ray observations of our MaNGA sample. We resort to existing X-ray surveys of galaxy groups to construct a representative set of background gaseous environments for our simulations. For most of the X-ray detected groups, a single or double β-model (Cavaliere & Fusco-Femiano 1976) provides a reasonably good fit to the surface brightness, for example in ROSAT samples in Mulchaey & Zabludoff (1998); Helsdon & Ponman (2000); Osmond & Ponman (2004), and in local volume samples in O'Sullivan et al. (2017). In the case of a double β-model, the central component represents the central galaxy or a central group region.

To minimize complexities in the simulation, we used a single beta-model (Eq. 3.1) to prescribe the gas density distribution in the simulation. We choose to fix the power-law index β but vary the core radius r_c to sample 4 different environments that the radio source could reside in. We do not model the compact component in the case of double β-model since the cores are usually small (a few kpc) and the jet will quickly punch through them. The variation in the core radius represents the various environment that the central galaxy could live in, depending on the mass of the group. We match the gas mass to be about 10% of the virial mass in our sample.

We use the density in galaxy groups measured by Pisano et al. (2004) and Freeland

& Wilcots (2011), who used bent-double radio galaxies to probe the intra-group medium, to inform our choices of density profiles. As shown in Fig. 3.1, the β-model profiles cover most of the observed density in galaxy groups. The central density is based on the X-ray observations of elliptical galaxies by Fukazawa et al. (2006), who showed the electron density at 10 kpc ranges between 10^{-3} cm^{-3} and few times of 10^{-2} cm^{-3}. We set the core density to be 10^{-2} cm^{-3} and do not model the dense gaseous core of the central galaxy. The temperature profile is isothermal at 1 keV.

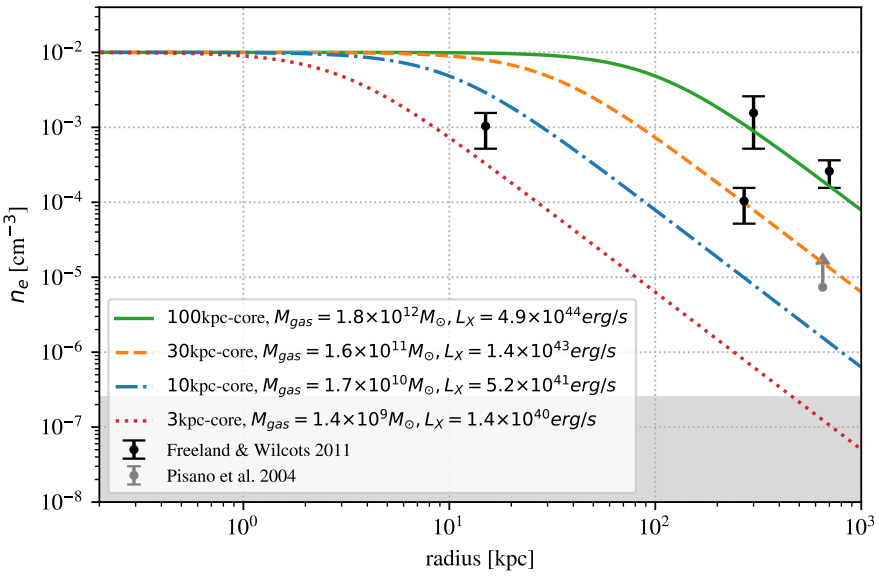

Figure 3.1 : Range in density profiles investigated through the simulations, spanning the parameter space of group profiles in the literature. We will use the same color scheme to represent the environment throughout this work.

The range of jet powers is informed from the radio flux in our samples. Using the relationship between synchrotron flux and cavity power by Godfrey & Shabala (2013); Cavagnolo et al. (2010), the jet powers of the samples fall between 10^{43} and 4×10^{44} erg s^{-1}.

We perform a total of 11 simulations covering 3 jet powers and 4 environments, as shown in Table 3.2. We do not carry out the low-power jet in the 100 kpc core simulation since the low-power jet will only reach up to 30 kpc in size and thus the background density profiles do not differ much between the 30 kpc core and 100 kpc core.

Table 3.2 : Grid of galaxy groups simulations and designations

core radius r_c [kpc] \ power [erg s^{-1}]	1.0×10^{43}	6.3×10^{43}	4.0×10^{44}
3	L430-rc3	L438-rc3	L446-rc3
10	L430-rc10	L438-rc10	L446-rc10
30	L430-rc30	L438-rc30	L446-rc30
100	L430-rc100	L438-rc100	NA

3.2.2 Jet Powers and Target Lobe Sizes

We configure the simulations according to our sample of MaNGA-selected galaxies. The distribution of the jet powers and size scales is shown in Fig. 3.2. Taking into account the computing resources, we select 3 different jet powers. The times for the jets being active are determined by the distribution of the sizes in our samples. We let the jet reach the largest size to cover most of the parameter space as shown in Fig.3.2.

3.2.3 Additional Improvements in Numerical Techniques

3.2.3.1 Shock Identification and Corresponding Tracers

In our first simulations, as described in Chapter 2, we implemented tracer particles on top of the AMR grid to follow the cooling of relativistic particles. The particles are injected at the cross-section of the jet nozzle. The cooling begins right away after the

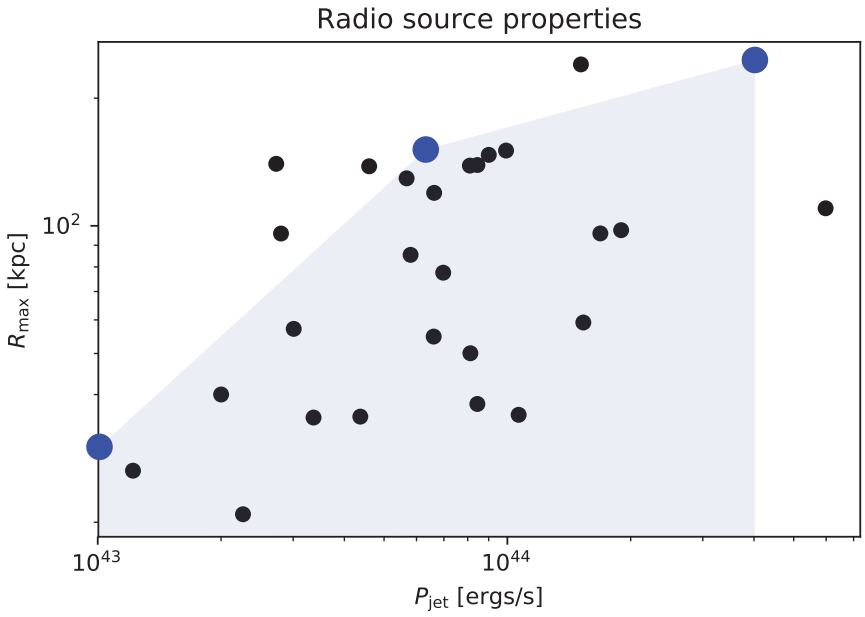

Figure 3.2 : Distribution of the jet powers and lobe sizes from the selected MaNGA samples. The simulations cover the range for most of the samples. Blue dots indicate the 3 jet powers and the target lobe sizes. Samples.

injection. Although it is still not clear how relativistic particles are accelerated in the jet, it is generally believed that the acceleration happens *in situ* inside the jet or at the shock in the hotspots. The underlying assumption of our method is that the relativistic electrons are accelerated to have a power-law energy distribution at the nozzle cross-section. However, as we analyzed the simulation and created radio maps at different frequencies, we realized that the cooling of the tracer particles is much more than we expected. Since the MHD simulation is non-relativistic, the jet fluid is set at 10 % of the speed of light in Chapter 2 in consideration of the computing resources and non-relativistic limit. It is known that the velocity of the jet can still be close to the speed of light at 10s of kpc. Thus, in our simulation, the tracer particles take much longer to reach the hotspot. With the strong magnetic fields in the jets, this results in the overcooling of the tracer particles.

Thus, we redesigned the cooling calculation of the tracer particles to avert the problem and have a more realistic acceleration and cooling scheme. The scheme is based on the assumption of diffusive shock acceleration mechanism. Diffusive shock acceleration (DSA) is a widely accepted mechanism for producing high-energy particles, also known as first-order Fermi acceleration, in which the particles gain energy as they are scattered upstream and downstream of the shock such that they repeatedly cross the shock (Blandford & Eichler 1987).

We identify cells of the shock front based on the velocity divergence and pressure gradient. The shock strength is calculated by estimating density ratios before and after the shock.

$$R = \frac{\gamma + 1}{\gamma - 1} \tag{3.4}$$

It is known that the DSA process produces a power-law spectrum with index

$$p = \frac{R + 2}{R - 1}, \tag{3.5}$$

where R is the compression ratio (Bell 1978; Drury 1983).

We begin following the cooling of the tracer particles when they are located in the shock cells. Numerically, we begin the integral in Eq. 2.12 when the particle leaves the shocked cells. At the same time, the power-law index is determined by the shock strength and recorded in the particle information. We keep track of several cooling integrals based on different criteria, including the encounter of the strongest shock (`TAU1`), the second strongest shock (`TAU2`), the last shock (`TAU3`), and the time when the velocity of the fluid drops below half of the initial jet velocity (`TAU4`).

In this work, the cooling integral associated with the strongest shock is used for generating synthetic radio maps. The combination of other cooling integrals will be incorporated in future work.

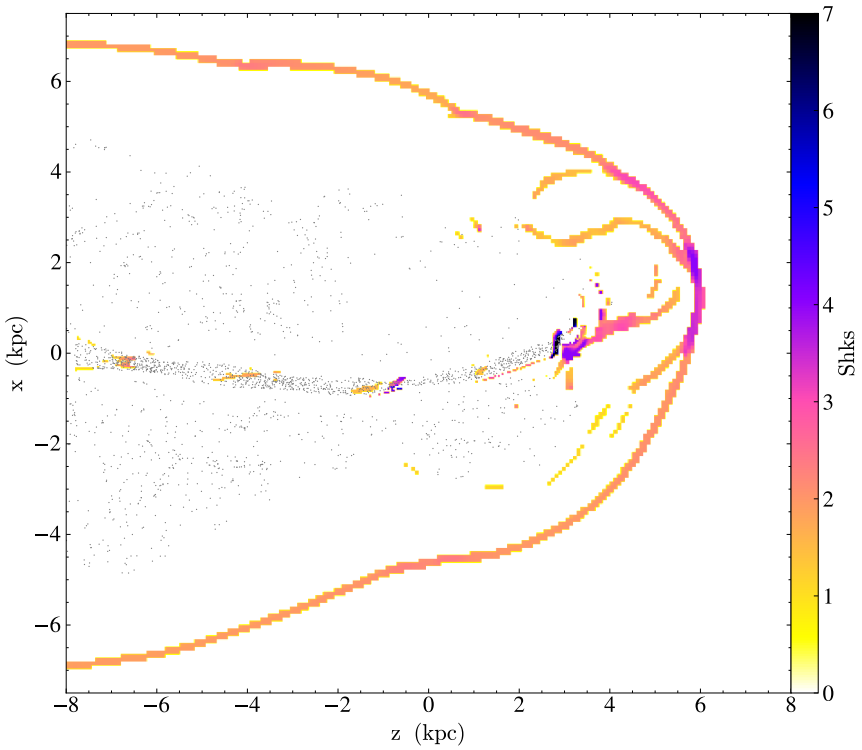

Figure 3.3 : An example slice showing the location and strength of the shock identified by the code. The distribution of jet particles within one minimum cell width from the plane is also shown. We see the termination shock at the end of the jet and also the cocoon shock surrounding the compressed gas, which is caused by the expansion of the bubble. The color indicates the compression ratio of the shock.

3.2.3.2 Additional Cooling Effects

In addition to the synchrotron cooling, we further include inverse-Compton cooling due to CMB and stellar light of the host galaxy, assuming a constant CMB photon density and a spherically symmetric distribution of stellar light. The ratio between the photon density of the CMB and the stellar light can be adjusted post-simulation to account for different properties of the host galaxies.

These effects are stored in the simulation particles, but are not included in the work

presented in this chapter.

3.3 Results

3.3.1 Radio Morphology Comparison

We first show the time series of radio maps for all simulations. In Fig. 3.4, low-power jets in 30, 10, 3 kpc core radii are shown at 5 different times in the simulation. We indicate the core radius by the blue circle in the figures. We can see when the jet launches in the roughly uniform medium inside the core, the radio lobes are shaped approximately like an elongated ellipsoid. When the jets punch through the constant density region outside the blue circle, they begin to expand quickly and form a classical FR-II (Fanaroff & Riley 1974) object, similar to a dumbbell.

The effect is more noticeable in mid- and high-power jets when they propagate further away from the uniform density core as shown in Fig. 3.5 and 3.6. If we consider the width of the radio lobes at the midplane (z=0), we can see that in the 100-kpc core environments, the circumference of the radio lobe keeps increasing since the bubbles try to expand in a rather uniform medium (the first columns in Fig. 3.5 and 3.6). In the 30-kpc core environments, the circumference at the midplane begins to shrink after the lobe reaches outside of the core (Fig. 3.5, the second column from 40 to 80 Myr and third column from 20 to 40 Myr; see also Fig. 3.6, the second column from 40 to 80 Myr).

Since the jets are directional, they expand into both sides of the group medium. When the density is high, the jet fluid quickly flows back within the bubble, and the elongate hot bubble expands in all directions. Once the jets drill outside of the core of the group medium, the fluid can propagate much further without accumulating around the central plane. Thus, the jet heads expand much quicker than other regions. In addition, gravity

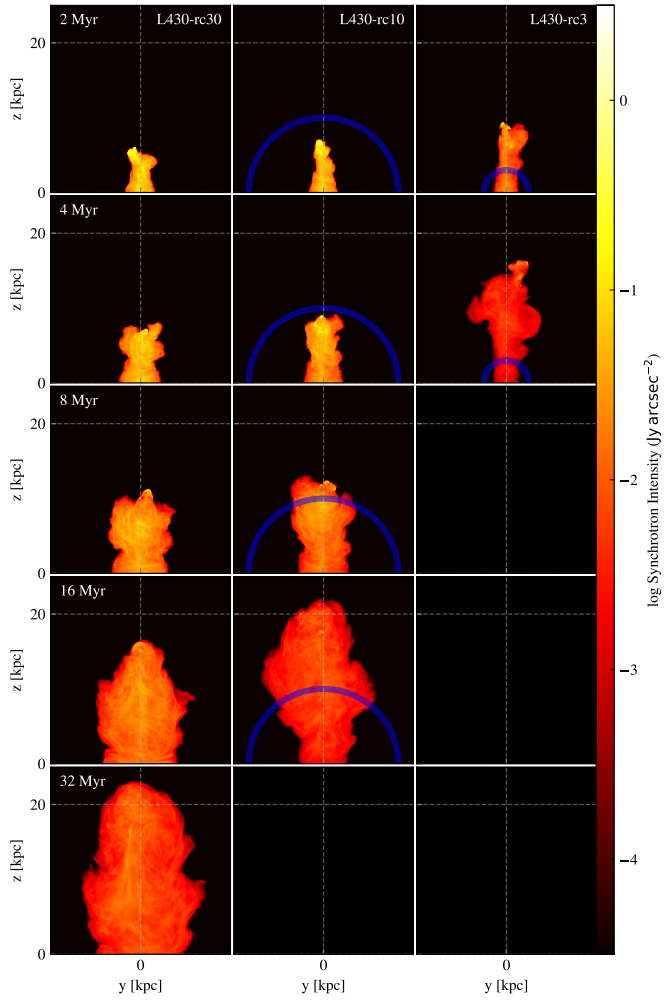

Figure 3.4 : Evolution of synchrotron emission at different times for the low power jets ($L = 10^{43}$ erg s^{-1}). The jets are propagating in different environments. From left to right, core radii in the β-model are 30, 10, 3 kpc. The transparent blue circles indicate the core radius in each panel.

tries to restore the equilibrium state of the group medium by bringing the displaced gas back to the center, as illustrated in Fig. 3.7. Thus, there is an inflow in the equatorial plane that squeezes the jet fluid. In some cases, the compression even makes the radio emission brighter in the thin jets (e.g. r_c=10 at 40 Myr in Fig. 3.5). Note that we exclude the fast-moving jet fluid in the synthesized radio maps since we do not model the relativistic

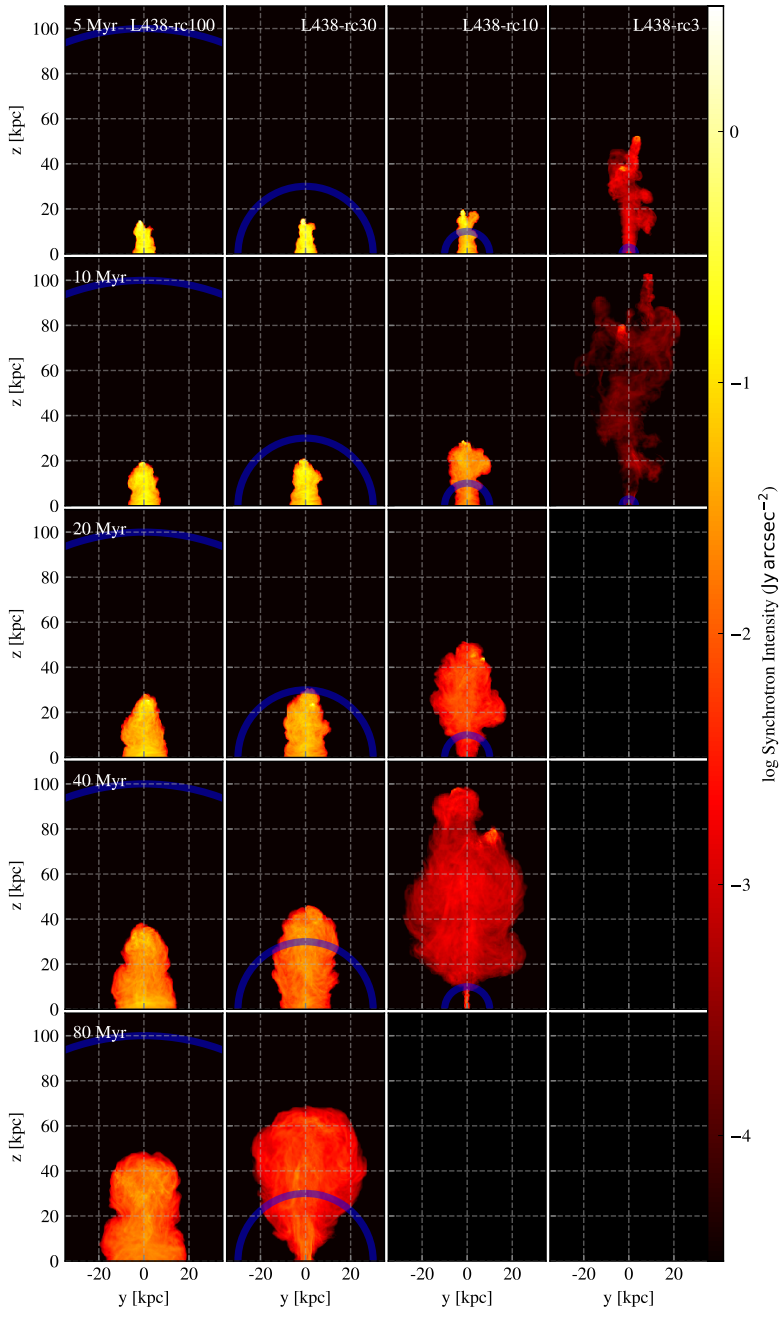

Figure 3.5 : Evolution of synchrotron emission at different times for the mid-power jets ($L = 6.3 \times 10^{43}$ erg s^{-1}). The jets are propagating in different environments. From left to right, core radii in the β-model are 100, 30, 10, 3 kpc. The dashed grids mark the same scale as in Fig. 3.4.

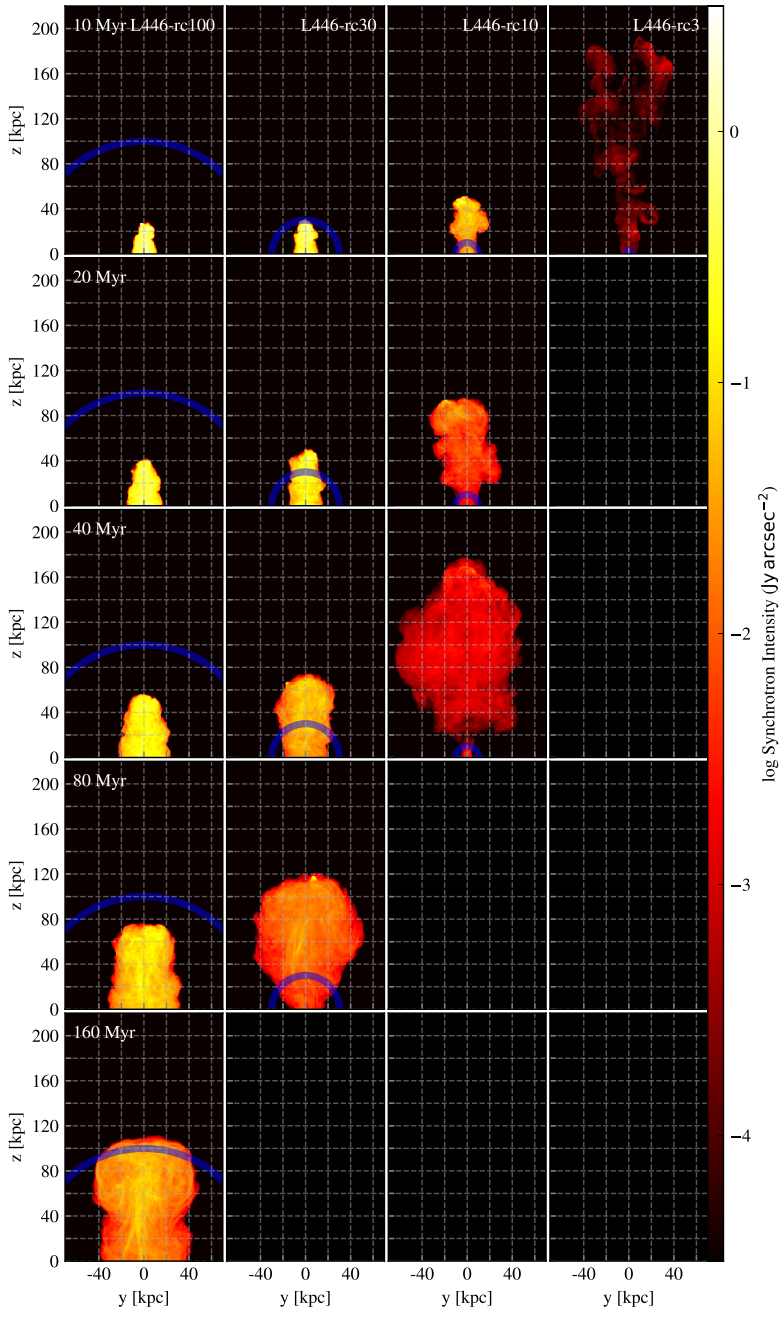

Figure 3.6 : Evolution of synchrotron emission at different times for the high-power jets ($L = 4.0 \times 10^{44}$ erg s^{-1}). The jets are propagating in different environments. From left to right, core radii in the β-model are 100, 30, 10, 3 kpc. The dashed grids mark the same scale as in Fig. 3.4 and 3.5.

boosting of the emission and thus the radio maps can be considered as if the jets were just turning off. The brightening of the jet region does not result from the active jets, but from the old plasma being compressed.

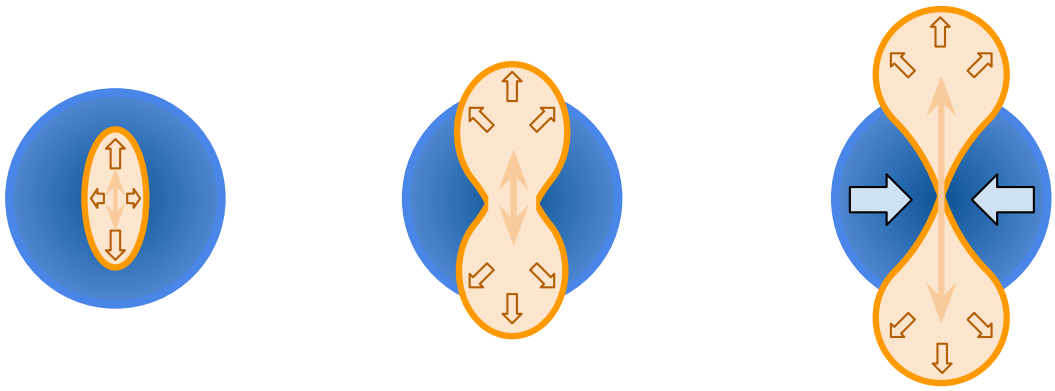

Figure 3.7 : Illustration of lobe expansion in the background profile with an uniform-density core. The bubble expands initially around the equatorial plane, but shrinks to a thin passage as the bubble reaches outside of the core region.

The least dense environment, in which the core size is 3 kpc, represents an isolated galaxy. In this environment, the morphology of the radio emission depends highly on the jitter of the jet axis. Multiple spikes are visible due to change of the pointing directions of the jets.

3.3.2 Same Lobe Sizes in Different Environment and Jet Power

For a given radio source, it is often possible to determine the size of the radio emission. However, the environments that the radio sources reside in are much harder to infer without dedicated X-ray observations. We aim to find distinguishable features from the simulations that may help us constrain the properties of the environments.

For this purpose, we select simulations when the radio lobes reach a specific size and

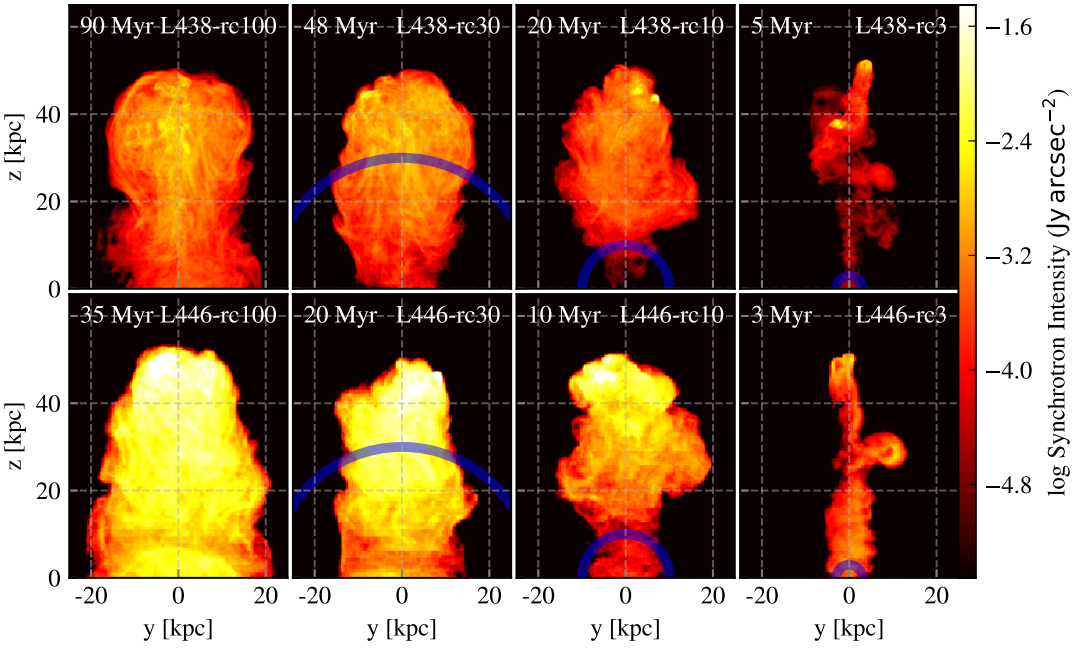

Figure 3.8 : Comparison of the radio lobes at 100 MHz when the lobes reach the same extent (50 kpc) for mid- and high-power jets in different environments. Low-power jets do not reach this size and are omitted here.

compare the resulting morphology and spectral index variations in the lobes caused by either the jet powers or the environments. We select from the high-power and mid-power simulations when one side of the lobe reaches 50 kpc. The low-power jets do no reach 50 kpc while the jets are active and are thus omitted in this comparison. The maps of the radio emission are shown in Fig. 3.8. The transparent blue circles mark the core radius of the gaseous profile, within which the density is roughly constant (cf. Fig. 3.1).

As we have seen in the time series radio maps, the shapes of the radio sources are determined by the environments, even if the extent of the lobes are the same. For jets in the densest environment (100-kpc core), the radio lobe is shaped like an elongated ellipsoidal bubble. From 30-kpc to 10-kpc core, the radio lobe becomes more dumbbell-like. For the 3-kpc core environment, the jet quickly reaches the same extent without enough time

to form a rounded bubble. Thus, the radio lobe appears irregular with several hotspots dominating the emission.

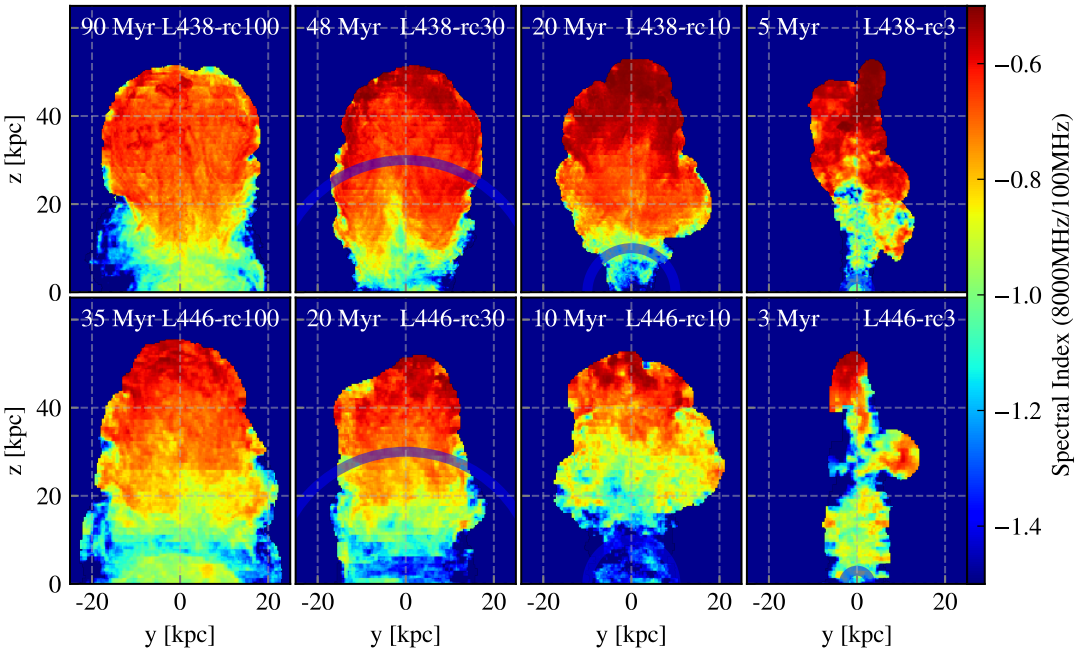

Figure 3.9 : Comparison of the spectral index when the radio lobes reach the same extent (50 kpc) for mid- and high-power jets in different environments. The spectral index α is calculated as $\alpha = \log(I_{\nu_1}/I_{\nu_2})/\log(\nu_1/\nu_2)$. In this figure, $\nu_1 = 8$ GHz and $\nu_2 = 100$ MHz.

The spectral index maps between 100 MHz and 8 GHz are shown in Fig. 3.9. Since the jets are still actively injecting fresh plasma at the tips of the lobes, we can observe the gradients of the spectral index from flatter at the heads to steeper at the midplane (z = 0). The jets in less dense environments ($r_c = 3$ and 10 kpc) also show flatter spectra (dark red color in Fig. 3.9) at the heads compared to the jets in denser environments. The flatter spectra at the jet heads are likely due to the relatively younger age of the sources. The jets in the dense background, nonetheless, also inject fresh plasma at the heads, but the emission from this young plasma mixes with older plasma and thus the observed spectra appear to be steeper.

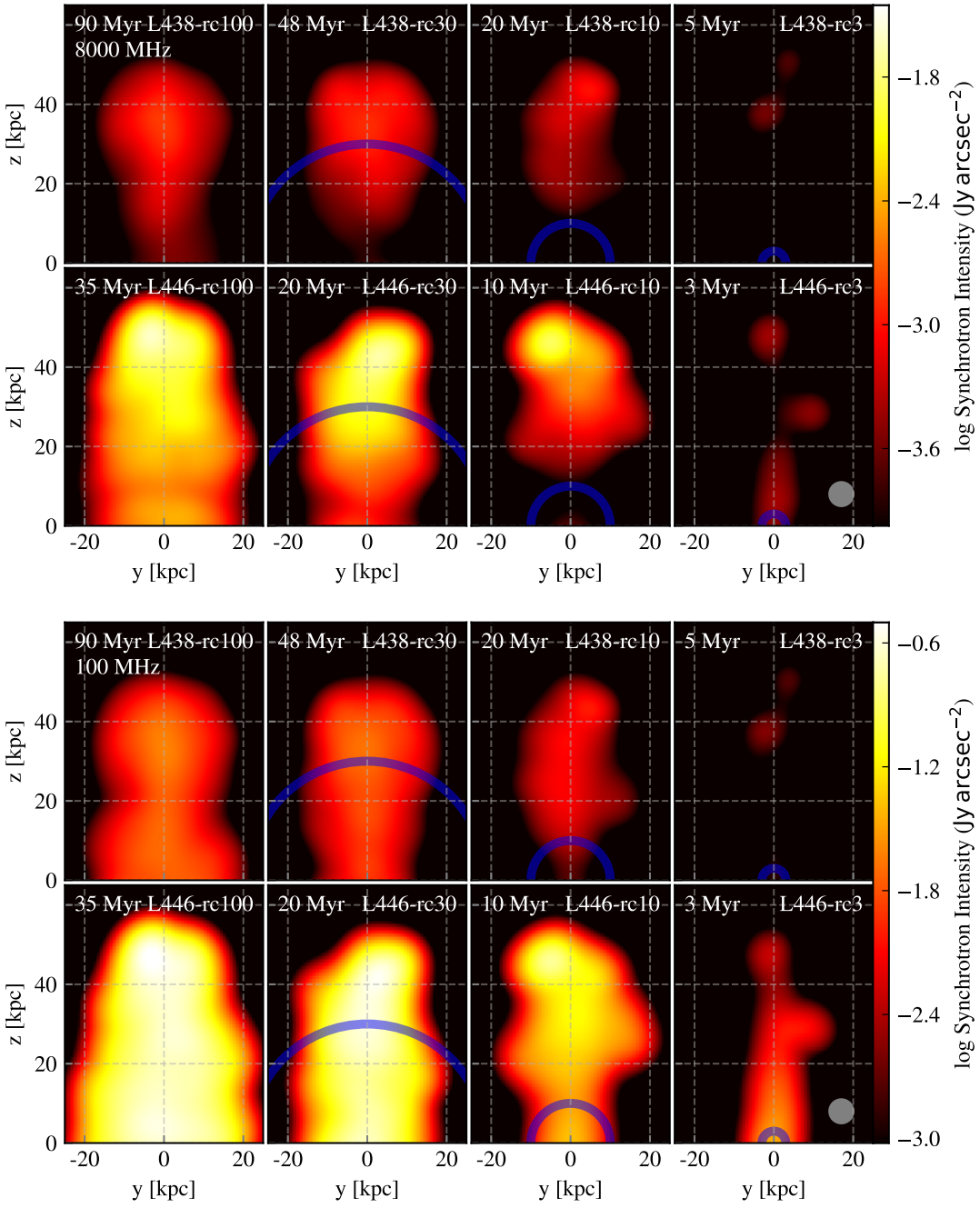

Figure 3.10 : The smoothed images at 8 GHz and 100 MHz for the same simulations shown in Fig. 3.8. The radio maps are smoothed by a Gaussian kernel of $\sigma = 3$ kpc, as indicated at the bottom right corner. The color range is scaled according to $\nu^{-0.5}$ such that the zero-age synchrotron emission will show the same color in two frequencies.

These results emphasize the role of low-frequency deep radio observations since the emission around the equatorial plane is only visible at low-frequency and is relatively weak. We compare the morphological differences in Fig. 3.10 when the radio sources are smoothed by a Gaussian kernel with σ=3 kpc, which corresponds to 1.6 arcsec for an object at redshift z=0.1. We see that for mid-power jets (L438), the high-frequency (8 GHz) emission does not differ much in different environments as shown in the first row of Fig. 3.10. However, at low-frequency (100 MHz), we see the emission from the equatorial plane and can better infer the shape of the synchrotron emitting region. Of course, the morphology depends on the sensitivity of the observations, but we will have a better chance to distinguish the differences at lower frequencies since the emissivity inversely scales with frequency for power-law electron distributions.

As the simulations imply, if a high-power jet is launched from an isolated galaxy, which corresponds to our 3-kpc core profile, it is plausible that we may not be able to detect the radio emission. Whether an isolated galaxy could host and sustain a high-power jet is a question that needs to be answered separately.

3.3.3 Evolution of Lobe Sizes

We can use similar methods as in Section 2.3.2 to examine the evolution of jet lobes in different environments. In Fig. 3.11, we show the propagation of the jet heads for 3 different jet powers and in 4 different environments, characterized by the core radius r_c. As expected, the most powerful jet in the least dense environment propagates the fastest. The high-power jet in the 3-kpc core profile makes it to 250 kpc in less than 13 Myr.

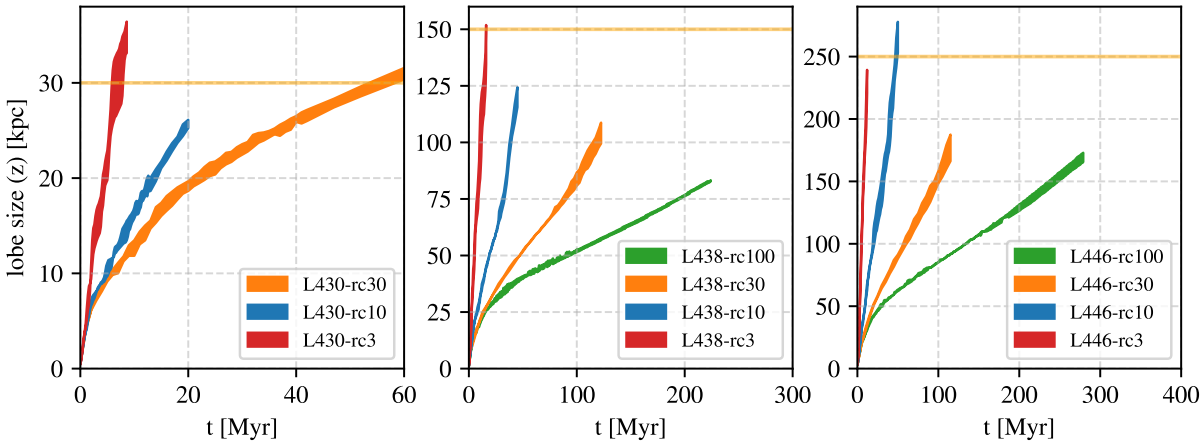

Figure 3.11 : Evolution of the lobe extent for all simulations. *Left*: low-power jets; *middle*: mid-power jets; *right*: high-power jets. Edges of the shaded area represent the furthest extents of the jet fluid in +z and -z directions, representing two sides of the jets. The yellow lines mark the target lobe sizes to be reached in the simulations.

3.3.4 Radio Power and Jet Power

The energetics of jets are usually measured by the cavity shown in X-ray observations (e.g. Bîrzan et al. 2004; Hlavacek-Larrondo et al. 2012). However, not all radios sources have deep enough X-ray coverage. Thus, radio luminosity is usually used to estimate the mechanical jet power. The scaling relationships between these two quantities are crucial to estimate the jet power in systems. Observationally, Bîrzan et al. (2008) and Cavagnolo et al. (2010) examined a sample of 24 and 21 systems, respectively, to establish the scaling between $P_{\rm jet}$ and $L_{\rm radio}$. Although with large scatter, they found a power-law scaling over 8 decades in jet power and radio luminosity

$$P_{\rm jet} \propto L_{\rm radio}^{\beta}, \tag{3.6}$$

where β falls between 0.3 and 0.7.

The synchrotron emissivity in our simulations is calculated according to the electron

energy distribution, the number density of the electrons, and the strength of magnetic fields as detailed in Appendix A.2. The magnetic fields, as prescribed in our simulation to be in equipartition with the thermal pressure in the jet nozzle, do depend on the total power of the jets.

We first inspect the evolution of total radio luminosity in our simulations. As shown in Fig. 3.12, the 100 MHz radio luminosity is calculated, assuming the emission is isotropic[2]. The synchrotron luminosity stays nearly at the same level in the very dense background and when the jets are still in the constant density region. In the less dense environment, the luminosity quickly drops, sometimes more than an order of magnitude. The synchrotron emission is brightest in the dense environment since the collision between the jet fluid and the group medium dramatically enhances the magnetic fields, especially at the hotspots where the jets terminate.

In the simulation, we control the total energy output of the jets. We can put the relationship between the jet power and radio power in the context of observational data. The observational data and the empirical best fits from Bîrzan et al. (2008) and Cavagnolo et al. (2010) are reproduced in Fig. 3.13. The points from our simulation mostly populate the brighter side of the relationship except for those in the 3-kpc core background, as the jets are still active and constantly injecting fresh plasma into the cavities. We expect that the radio luminosity quickly drops after the jets turn off. For the jets in less dense environments, the radio luminosity is weaker than the observational correlation, since the observations focus on galaxy clusters, which correspond to our densest environments.

[2]The radio emission is not isotropic, but depends on the viewing angle and the directions of magnetic fields. However, due to the highly tangled fields as we discussed in Section 2.4.4, especially at a later stage when the lobe is much larger than the radius of the jet, the assumption on the isotropic emission is adequate for the estimation of total luminosity.

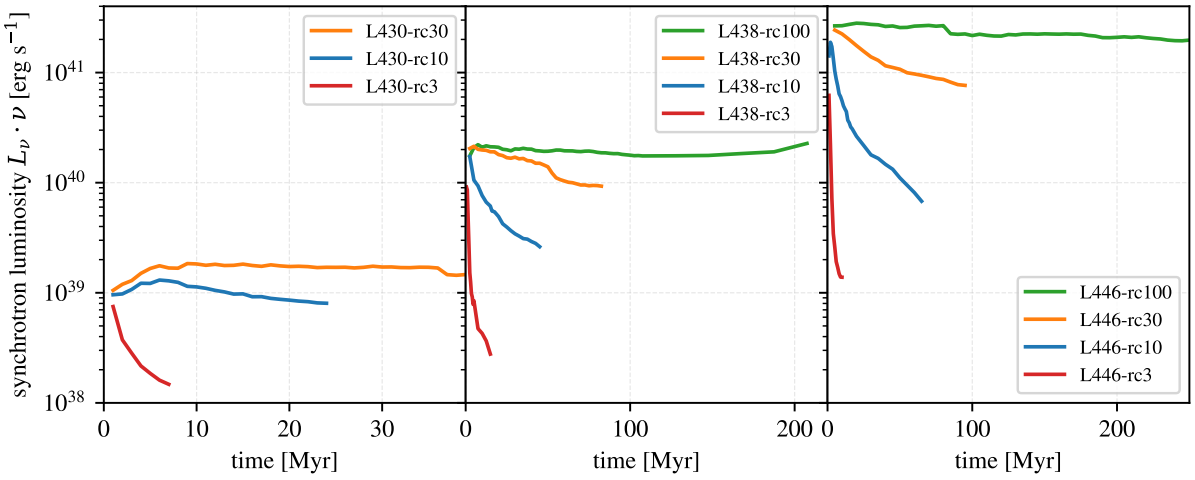

Figure 3.12 : Evolution of the radio luminosity at 100MHz for all simulations. *Left*: low-power jets; *middle*: mid-power jets; *right*: high-power jets. The jets in the densest environment, or the largest core radius, maintain roughly a constant radio output, while the radio luminosity for jets in less dense environments quickly decreases.

The jet power in observations is commonly determined from X-ray cavities, which represents an average power over the course of the bubble inflation. As we have seen in Fig. 3.12, the synchrotron luminosity varies dramatically in different environments, even if the jet powers are the same. The power of the jet remains constant while the jet is active in the simulation, which is unlikely in the actual cases. The variation of the jet power might directly impact the resulting radio luminosity and can explain part of the large scatter in the relationship.

3.4 Summary and Conclusions

In this work, we conduct 11 simulations, covering 3 different jet powers and 4 different environments, parametrized by the core radius r_c in the β-model. We improve the techniques developed previously in Chapter 2 to model the cooling of synchrotron emitting

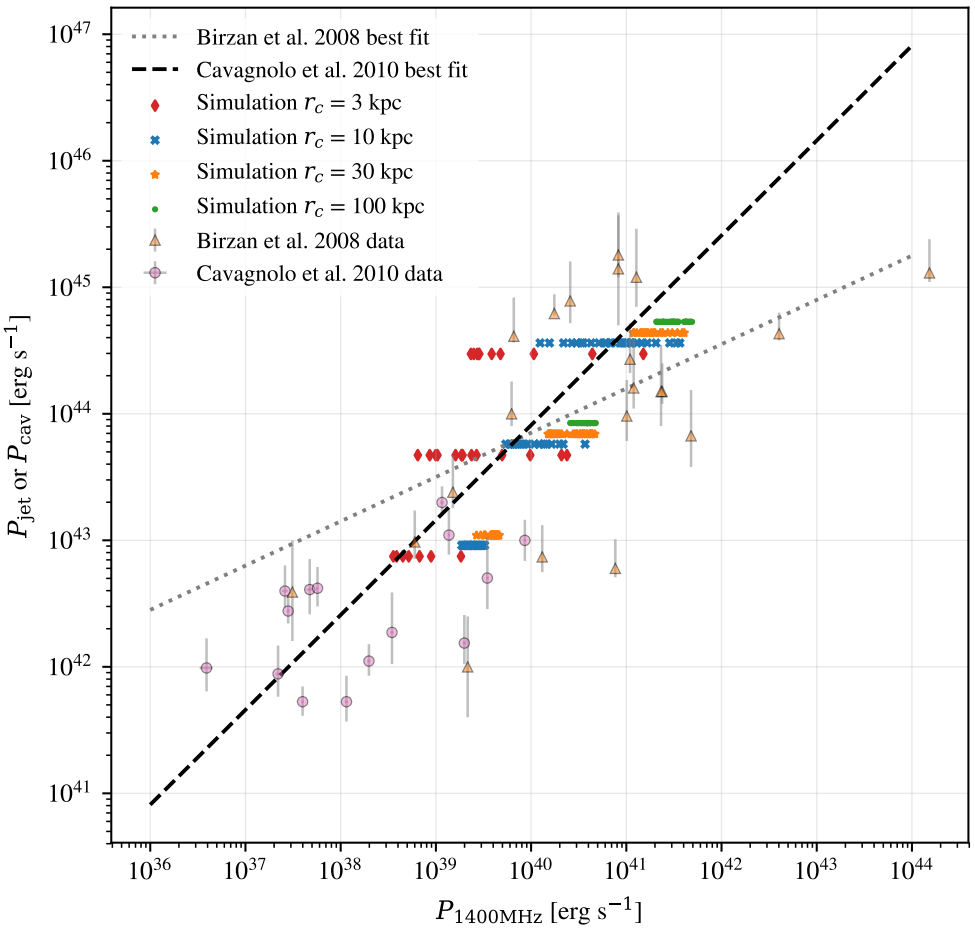

Figure 3.13 : Relationship between radio luminosity at 1400 MHz and total jet power from the simulations and comparison to observational data by Bîrzan et al. (2008) and Cavagnolo et al. (2010). The simulation points are slightly offset from the actual jet powers for clarity. The radio luminosities from Bîrzan et al. (2008) are calculated using WMAP9 cosmological luminosity distances.

plasma by identifying shocks in the numerical simulation.

We show that the morphology of the radio lobes is affected by the combination of jet powers and environments. The radio emission from the lobes inflated by the jets of the same power appears vastly dissimilar in different environments. For the jets propagating within dense environments, the radio lobes are more rounded and have large circumference in the equatorial plane. Once the jets advance beyond the uniform-density core, the heads of the lobes expand quickly and the radio lobes look like classical FR-II sources.

The radio luminosity of jets is empirically measured to be related to the jet power. In this study, we reproduce the relationship from simulations and further reveal how this correlation depends on environment and jet active time.

We use a single β-model with different core radius r_c to prescribe the environment of the jets. It has been known that, in many cases, a double β-model can better fit the X-ray observations of groups and galaxies. The exploration of jet-ambient medium interaction can be extended to a more complicated background profile. For example, varying β or having a double β-model. Putting the jet in a dynamic galaxy group might help us understand the nature of bent-double radio source.

References

Antonuccio-Delogu, V., & Silk, J. 2008, MNRAS, 389, 1750

Baldry, I. K., Glazebrook, K., Brinkmann, J., et al. 2004, ApJ, 600, 681

Bell, A. R. 1978, MNRAS, 182, 147

Bell, E. F., Wolf, C., Meisenheimer, K., et al. 2004, ApJ, 608, 752

Bîrzan, L., McNamara, B. R., Nulsen, P. E. J., Carilli, C. L., & Wise, M. W. 2008, ApJ, 686, 859

Bîrzan, L., Rafferty, D. A., McNamara, B. R., Wise, M. W., & Nulsen, P. E. J. 2004, ApJ, 607, 800

Blandford, R., & Eichler, D. 1987, Physics Reports, 154, 1

Bower, R. G., Benson, A. J., Malbon, R., et al. 2006, MNRAS, 370, 645

Cavagnolo, K. W., McNamara, B. R., Nulsen, P. E., et al. 2010, ApJ, 720, 1066

Cavaliere, A., & Fusco-Femiano, R. 1976, A&A, 49, 137

Dekel, A., & Woo, J. 2003, MNRAS, 344, 1131

Drury, L. O. 1983, Reports on Progress in Physics, 46, 973

Dubey, A., Antypas, K., Ganapathy, M. K., et al. 2009, Parallel Computing, 35, 512

Fabian, A. C. 2012, ARAA, 50, 455

Fanaroff, B. L., & Riley, J. M. 1974, MNRAS, 167, 31P

Freeland, E., & Wilcots, E. 2011, ApJ, 738, 145

Fryxell, B., Olson, K., Ricker, P., et al. 2000, ApJS, 131, 273

Fukazawa, Y., BotoyaNonesa, J. G., Pu, J., Ohto, A., & Kawano, N. 2006, ApJ, 636, 698

Gaibler, V., Khochfar, S., Krause, M., & Silk, J. 2012, MNRAS, 425, 438

Godfrey, L. E. H., & Shabala, S. S. 2013, ApJ, 767, 12

Heckman, T. M., & Best, P. N. 2014, ARAA, 52, 589

Helsdon, S. F., & Ponman, T. J. 2000, MNRAS, 315, 356

Hlavacek-Larrondo, J., Fabian, A. C., Edge, A. C., et al. 2012, MNRAS, 421, 1360

Kauffmann, G., Heckman, T. M., White, S. D., et al. 2003, MNRAS, 341, 54

Kormendy, J., & Ho, L. C. 2013, ARAA, 51, 511

Larson, R. B. 1974, MNRAS, 169, 229

Lee, D. 2013, Journal of Computational Physics, 243, 269

Mulchaey, J. S., & Zabludoff, A. I. 1998, ApJ, 496, 73

Osmond, J. P. F., & Ponman, T. J. 2004, MNRAS, 350, 1511

O'Sullivan, E., Ponman, T. J., Kolokythas, K., et al. 2017, MNRAS, 472, 1482

Pisano, D. J., Wakker, B., Wilcots, E., & Fabian, D. 2004, AJ, 127, 199

Su, K.-Y., Hopkins, P. F., Hayward, C. C., et al. 2019, MNRAS, 487, 4393

Wild, V., Heckman, T., & Charlot, S. 2010, MNRAS, 405, 933

Yesuf, H. M., Faber, S. M., Trump, J. R., et al. 2014, ApJ, 792, 84

Chapter 4

Jets, Bubbles, and Heat Pumps in Galaxy Clusters

A version of this chapter has previously appeared in the Monthly Notices of the Royal Astronomical Society

Chen, Heinz, & Enßlin, 2019, MNRAS

Abstract

Feedback from AGN jets has been proposed to counteract the catastrophic cooling in many galaxy clusters. However, it is still unclear which physical processes are acting to couple the energy from the bi-directional jets to the ICM. We study the long-term evolution of rising bubbles that were inflated by AGN jets using MHD simulations. In the wake of the rising bubbles, a significant amount of low-entropy gas is brought into contact with the hot cluster gas. We assess the energy budget of the uplifted gas and find it comparable to the total energy injected by the jets. Although our simulation does not include explicit thermal conduction, we find that, for reasonable assumptions about the conduction coefficient, the rate is fast enough that much of the uplifted gas may be thermalized before it sinks back to the core. Thus, we propose that the AGN can act like a geothermal *heat pump* to move low-entropy gas from the cluster core to the heat reservoir and will be able to *heat* the inner cluster more efficiently than would be possible by direct energy transfer from jets alone. We show that the maximum efficiency of this mechanism, i.e. the ratio between the conductive thermal energy and the work needed to lift the gas, $\xi_{\rm max}$ can exceed 100%. While $\xi < \xi_{\rm max}$ in realistic scenarios, AGN-induced thermal conduction has the potential to significantly increase the efficiency with which AGN can heat cool-core clusters and transform the bursty AGN activities into a smoother and enduring heating process.

4.1 Introduction

The cores of galaxy clusters often exhibit strong x-ray emission with cooling times short compared to the cluster age, which should lead to substantial radiative cooling and the formation of a *cooling flow* (Fabian 1994). The lack of cold gas in observations (Peterson et al. 2003; Peterson & Fabian 2006) motivates the study of feedback processes that could counteract the cooling (McNamara & Nulsen 2007; Fabian 2012). Mechanical energy deposited by AGN jets could serve as the mechanism to regulate the thermal evolution of galaxy clusters (see McNamara & Nulsen 2012, for review). Strong evidence supporting this mechanism includes X-ray observations of galaxy clusters, which often show radio-filled cavities that are likely inflated by jets from the supermassive black holes in the central galaxy (see e.g. Bîrzan et al. 2004). In many cases, multiple cavities, likely caused by episodic jet activity, are observed. The most detailed observations of this kind include the Perseus Cluster (Fabian et al. 2011) and M87 (Forman et al. 2007). Churazov et al. (2000) show that AGN jets have comparable power to offset the cooling in the Perseus Cluster. Observations of numerous other cool core clusters support this claim, but with large scatter in jet power (see e.g. Rafferty et al. 2006; McNamara & Nulsen 2007; Hardcastle et al. 2019).

However, the processes through which the energy of AGN jets couples to the ICM are still uncertain. The highly directional nature of jets poses substantial difficulty to distribute their energy isotropically in the core of galaxy clusters (O'Neill & Jones 2010). Fabian et al. (2017) argue that the dissipation of sound waves, which are visible as ripples in the x-ray observations, could heat the ICM. Heinz et al. (2006) and Morsony et al. (2010) show that large-scale motion of the cluster helps to disperse the energy from the AGN. Other possible mechanisms include turbulence (Zhuravleva et al. 2014), mixing (Hillel & Soker 2016; Yang

& Reynolds 2015; Hillel & Soker 2018), shocks (Fabian et al. 2006; Li et al. 2017), internal waves (Zhang et al. 2018), and cosmic ray streaming (Enßlin et al. 2011; Ehlert et al. 2018) among others.

Although most of the discussion of heating focuses on the direct energy coupling between the AGN output and the ICM, a few authors have alluded that the removal of the cool gas from the core of the cluster could possibly prevent catastrophic cooling. Yang & Reynolds (2016) point out that a "gentle circulation" can help isotropize the heating from the weak shock and mixing that happens primarily in the jet cone. Uplifted gas trailing the bubbles was also noticed in simulations (Weinberger et al. 2017; Duan & Guo 2018). Pope et al. (2010) calculate the amount of gas transported by a rising bubble and conclude that the mass transport by the bubble wake could prevent the core from overcooling.

Buoyantly rising bubbles are identified and studied by many works. Churazov et al. (2001) conduct hydrodynamic simulations of bubbles to model the radio and x-ray arms in M87. In a deep *Chandra* observation, Forman et al. (2007) detected many filamentary structures that could be associated with independent bubbles in M87. Wise et al. (2007) identify a series of cavities in the Hydra A cluster. Gendron-Marsolais et al. (2017) report observations of cool x-ray gas rims in NGC 4472 that could be gas lifted by the bubbles. Su et al. (2017) find the gas uplift rate is comparable to that expected to cool in low-mass Fornax cluster. These works all suggest that rising bubbles are prevalent and could bring gas from the core to the outskirt of the galaxy cluster.

Although thermal conduction is considered insufficient to offset the cooling in cool-core clusters by itself (Voigt & Fabian 2004; Dolag et al. 2004), it still plays a vital role in the thermal state of the cluster, especially when perturbed by the rising bubble. In this work, we propose and investigate the effect of rising bubbles bringing low-entropy gas from the cool core to the hot outskirts of the galaxy cluster where thermal conduction is much

more efficient. With this mechanism, the AGN could "heat" the ICM with an efficiency that can exceed 100%, drawing on the excess heat contained in the outer cluster like a heat pump. This heating process is also more gentle than direct heating.

This work is organized as follows. We describe the methodology and techniques in Section 4.2. In Section 4.3, we present the results of the simulations, including the energy budget and the conduction rate estimates. We derive and calculate the efficiency of this mechanism in simplified profiles in Section 4.4. In Section 4.5 and 4.6, we discuss and summarize our findings.

4.2 Numerical Setup and Techniques

Here we describe the important and relevant details of the simulation. We conduct full 3D ideal MHD simulations using `FLASH` (Fryxell et al. 2000; Dubey et al. 2009) with the unsplit staggered mesh scheme (Lee 2013) and AMR. We simulate the cluster as a spherically symmetric environment, tuned to match the properties of the cool-core Perseus Cluster following Zhuravleva et al. (2015). The density profile follows a β-model

$$\rho(r) = \rho_0/[1 + (\frac{r}{r_c})^2]^{\frac{3}{2}\beta}, \tag{4.1}$$

with $\rho_0 = 9.6 \times 10^{-26}$ g/cm^3, $r_c = 26$ kpc, $\beta = 0.53$. The temperature profile is set such that the core of the cluster is cooler than the outskirts,
$T(r) = T_{\rm out}\left([1 + (\frac{r}{r_{\rm c,T}})^3]\right) / \left(\frac{T_{\rm out}}{T_{\rm core}} + (\frac{r}{r_{\rm c,T}})^3\right)$, with $T_{\rm core} = 3.0$ keV, $T_{\rm out} = 6.4$ keV and $r_{\rm c,T} = 60$ kpc. We assume monatomic gas in the cluster so that the adiabatic index $\gamma = 5/3$ and choose the mean molecular weight $\mu = 0.61$. The cluster potential is assumed to be spherically symmetric and static throughout the simulations, neglecting changes in the gravitational potential due to the changes in gas density. The fixed gravitational potential is chosen so that the initial conditions are in hydrostatic equilibrium. Our simulations were

set up to study a wide context of questions relating to jet and cluster physics that do not require magnetization of the ICM, so it was not included in the initial conditions of our simulations. The simulation box is $1 \times 0.5 \times 0.5$ Mpc with hydrostatic diode boundary condition (`hydrostatic-f2+nvdiode` in `FLASH`). The adaptive refinement criteria include the native second derivative based estimator and also a self-defined momentum-based condition that ensures that we resolve the jets at the highest resolution (30 pc). The jets are active at a constant jet power until 10 Myr. We restrict the maximum refinement level for the ICM further away from the center. To study the motion of the gas, we use Lagrangian tracer particles in `FLASH` (Dubey et al. 2012). Using density-weighting, we randomly distribute 5×10^5 particles within a 150 kpc radius in the ICM. Thus, each particle represents approximately the same mass.

We set up a *nozzle* through which energy, momentum, and magnetic flux are injected into the simulation grid to model the jets from the central AGN. The magnetic pressure is in equilibrium with the thermal pressure in the nozzle, i.e. plasma β=1. We further set the jet power (10^{45} erg/s), jet speed (0.1c), nozzle radius (240 pc), and the internal Mach number (10), which sets the jet density. The magnetic field of the jet nozzle is set to be poloidal, i.e., parallel to the jet propagation direction[1]. The jet is active for 10 Myr, during which it operates at constant power. The direction of the jet is set up to have a small angle ($\sim$ 8 degrees) jittering to mimic the dentist's drill effect seen in observations and inferred theoretically (Scheuer 1982). After 10 Myr, the jet shuts off and the bubbles inflated by the jets continue to rise. For computational expediency, the highest resolution of the simulation is reduced to 120 pc shortly after turning off the jet (from 30 pc when the jet is active). Radiative cooling and explicit thermal conduction are not included in

[1]We also performed simulations with other topologies which are fully consistent with the results shown here, see Chapter 2

the simulation. We investigate the long-term impact of this one-time activity of the jets on the dynamical state of the galaxy cluster. Visualizations and profile analysis are performed with the `python`-based software package `yt`[2] (Turk et al. 2010).

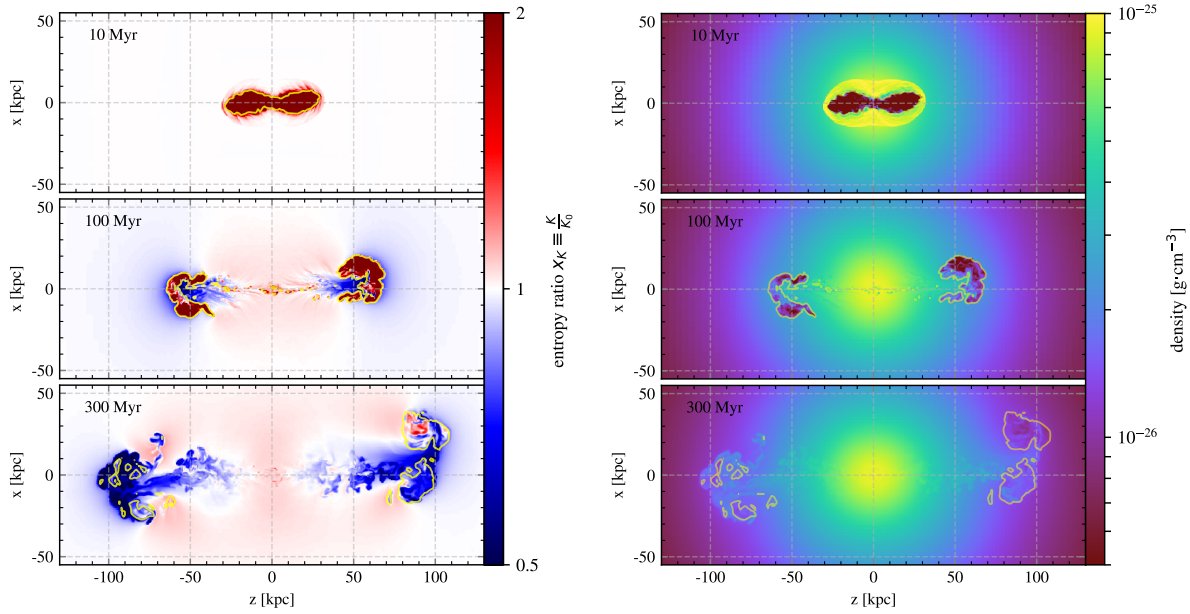

Figure 4.1 : Central slices of the simulation showing (*left*) the entropy of the gas relative to the initial entropy value at the same location and (*right*) the density of the gas at different times in the simulation. We can see the bubbles lift the low-entropy gas, while the cluster core is refilled by the higher-entropy gas. Yellow contours indicate the jet mass fraction of 10^{-3}, above which the conduction rate is excluded in the calculation in Section 4.3.4.

4.3 Results

4.3.1 Motion of the low-entropy gas

First, we investigate the lifting of the low-entropy gas by the rising bubbles. During the active phase of the AGN, only a small amount of gas is displaced by the jet. However, as the jet ceases and bubbles rise, they drag a significant amount of gas from the core in the wake. This phenomenon can be seen clearly in the entropy ratio maps. In Fig. 4.1, the specific entropy, defined as $K \equiv kT/n^{\gamma-1}$, of the gas at different times of the simulation is plotted relative to the entropy profile of the initial ICM conditions alongside the density slices. Since the entropy is conserved during adiabatic processes, the entropy ratio $x_K \equiv K/K_0$ is a good indicator of the origin of the gas[3]. An entropy ratio smaller than one shows the gas has been lifted radially outward, while an entropy ratio larger than one could mean that the gas has been moved inward or reveal the presence of the hot gas from the jet or the shocked cluster gas. When the jet is still active, at 10 Myr, only the very hot gas injected by the jets is visible in the entropy ratio map and the initial entropy profile of the ICM is almost unchanged. This anisotropic heating has been a challenge for invoking AGN feedback to counteract the strong x-ray cooling (O'Neill & Jones 2010).

However, the bubbles keep rising due to both buoyancy and momentum injected by the jets. At 100 Myr (middle panel of Fig. 4.1), we can see there is lower-entropy gas pushed ahead of the bubbles as well as rising in their wakes. A slight increase of density can also be seen in the right panels of Fig. 4.1. However, due to the underlying density gradient of the cluster profile and the strong contrast between the bubble and ICM gas, it

[2] http://yt-project.org/

[3] We do have shocks in the simulation during the initial inflation of the cocoon, so some fraction of the gas undergoes non-adiabatic heating. Its entropy will be correspondingly raised.

is not immediately obvious except in the bottom panel. The sphere inside the location of the bubble ($\lesssim$ 50 kpc) shows a general increase of entropy because of the replenishment of the gas from larger radii. At 300 Myr (lower panel of Fig. 4.1), most of the hot gas injected by the jet is mixed–mostly numerically–with the ICM[4]. The vortex generated by the bubble brings a notable amount of gas moving outward to large radii even further than the bubble. Only a small fraction of the hot gas is still visible as a ring surrounded by the lower-entropy gas. If there is no heat exchange between the high- and low-entropy gas, the low-entropy gas will eventually fall back to the core again. In Section 4.3.4, we argue that the conduction rate will increase when the low-entropy gas is brought into contact with the hot atmosphere, thus heating the gas efficiently before it sinks.

4.3.2 Percentage of gas lifted by the rising bubbles

To quantify the amount of gas being lifted by the rising bubbles, we use tracer particles to track the movement of gas. The particles are distributed according to the density of the gas at the beginning of the simulation. Thus, each particle represents roughly the same mass of gas. The radial displacement of these particles at 300 Myr is shown in the upper panel of Fig. 4.2, in which we group them by their initial radii.

The distribution of the gas displaced by the bubbles can be identified in the middle and lower panel of Fig. 4.2. We group the particles by their initial radii and use the kernel density estimation with the Gaussian kernel width matching the initial average separation between particles. The same kernel is used for both the cumulative distribution and probability density function. The distribution can be viewed as the distribution of mass for the gas in different initial radii. We can see that a larger fraction of mass is lifted

[4]It is important to note that we do *not* count the numerical mixing in our heating rate later on, as it is a purely numerical artifact.

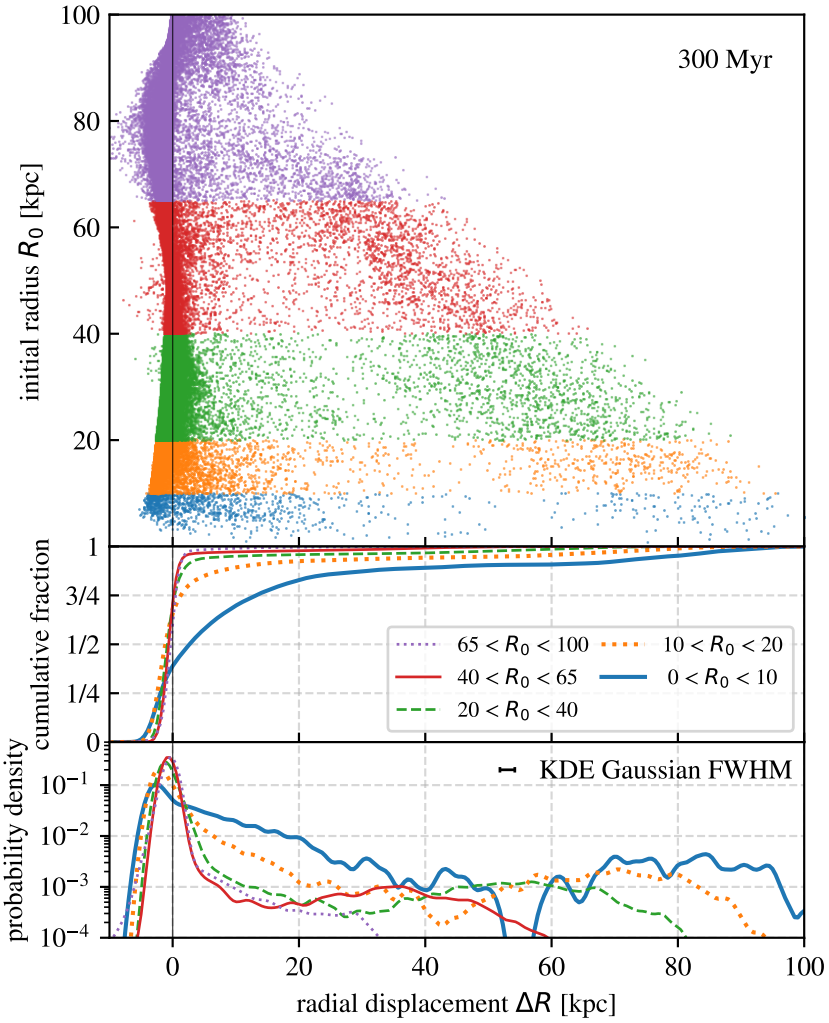

Figure 4.2 : Displacement of tracer particles at 300 Myr. The change in radius (horizontal axis) is plotted against the initial radius (vertical axis, upper panel) of the tracer particles. The particles are initialized such that the number of particles is proportional to the density of the gas. The middle and lower panel shows the cumulative distribution and probability density function using kernel density estimation for the particles grouped by their initial radii. We can see that around 15% of the gas initially within the 10-kpc core is lifted to more than 20 kpc away. While the low-entropy gas is lifted by the bubbles, rest of the higher-entropy cluster gas moves slightly inward to replenish the core.

for the gas closer to the core. For the gas initially inside 10 kpc radius, about 15 percent of the gas is lifted more than 20 kpc outward; for the gas in 10 to 20 kpc initial radii, the fraction is slightly less than 10 percent. This is the effect at 300 Myr of the bubble inflated by the jet that is active for only 10 Myr. If there were additional episodes of jet activity, the fraction would be larger.

In Fig.4.2, we can also see the replenishment of the gas in the core. The negative Δr in both the cumulative fraction and probability density indicates an inward motion due to the removal of low-entropy gas from the core. This motion gradually brings the higher-entropy gas from larger radii to the core. Note that the inflow and the outflow take place at different regions of the cluster – the outflow happens in the cone around the bubbles while the inflow occurs primarily outside the bubble cone.

4.3.3 Mass and energy budget of the low-entropy gas lifted by the rising bubble

We now investigate the mass of the low-entropy gas and the energy that could be extracted from the hot gas and transferred to the uplifted low-entropy gas by heat conduction. We identify gas with entropy ratio x_K below various thresholds in the simulation. The evolution of the mass of the low-entropy is shown in the upper panel of Fig. 4.3. We then estimate the amount of energy needed to bring this gas into thermal equilibrium with its surroundings, assuming monatomic gas under constant pressure:

$$E_{\mathrm{th},x_i} = \int \frac{5}{2} \frac{k_B \Delta T}{\mu m_p} \, \mathrm{d}M_{x_K \leq x_i}, \tag{4.2}$$

where μ is the mean molecular weight and ΔT is the difference between current and initial temperature of the gas at the same location.

We use this upper limit as a proxy for the amount of thermal energy that could be absorbed by the uplifted low-entropy gas. The actual energy budget will obviously depend

on the rate of thermal conduction, which will be discussed in Section 4.3.4, and the dynamic state of the cluster. The lower panel of Fig. 4.3 shows the evolution of this energy as a function of time with different values of x. The vertical axis at the left labels the energy in [ergs], while at the right it denotes this energy relative to the total energy ($\sim 3.16 \times 10^{59}$ erg) injected during the active phase of the jet (10 Myr).

One can see that the conductive energy budget of the low-entropy gas is comparable

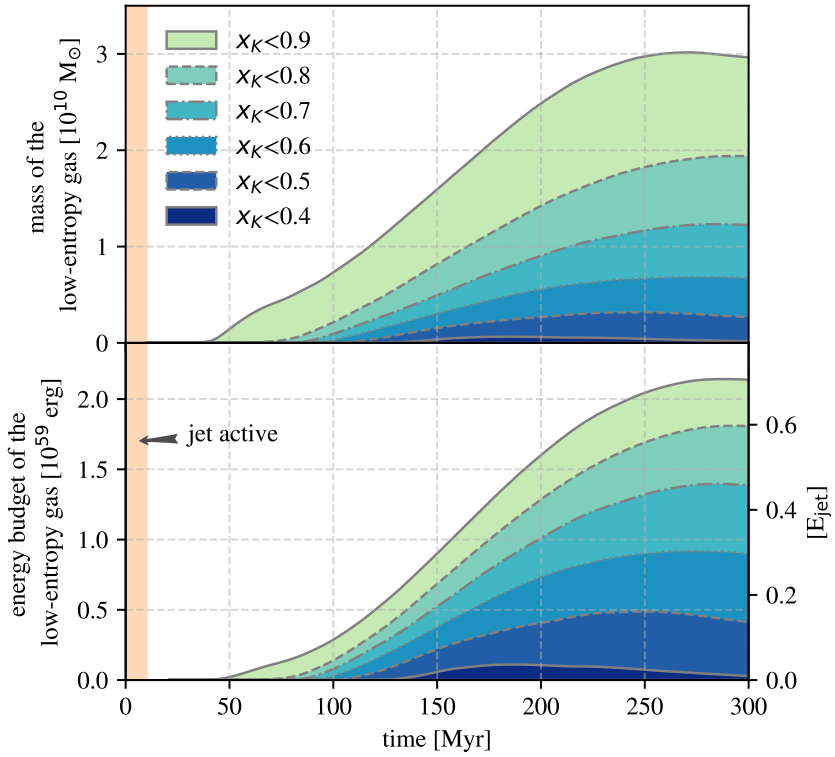

Figure 4.3 : The mass and the energy budget of the low-entropy gas. This figure shows (*upper panel*) the evolution of the amount of mass of the low-entropy gas, which is identified by entropy ratios x_K lower than the threshold, and (*lower panel*) the energy needed to bring the gas to the surrounding temperature. The y-axis on the right of the lower panel shows the energy budget relative to the total energy injected by the active jet in the first 10 Myr.

to the total energy injected by the jet and reaches the peak value at around $t_{\rm peak} \sim 300$ Myr. The value of $t_{\rm peak}$ naturally depends on the details of the system, including the density of the lobe and gravitational potential profile. However, it will likely be on the order of hundred million years, which is induced by the short active phase (10 Myr) of the jets. Thus, it may transform the bursty activities of the AGN into a much longer timespan and result in smoother heating of the cluster.

It is imperative to note that the heat exchange occurs between cluster gas, not with the very high-entropy relativistic plasma inside the bubble, which has a vanishingly small conduction coefficient. The estimated energy budget is not directly from the AGN itself, but from the hot atmosphere at large radii of the clusters, where the cooling time is longer than the Hubble time. When the cooler gas is brought into thermal contact with the hot reservoir, heat exchange can take place more efficiently than it could in a stratified cluster atmosphere. We discuss the rate of heat exchange in the next section.

4.3.4 Conductive heating rates

Next, we estimate the rate of thermal conduction between the uplifted low-entropy gas and the hot thermal bath. We consider the classic Spitzer conduction in ionized gas (Spitzer 1962; Narayan & Medvedev 2001). The Spitzer coefficient can be calculated as

$$\kappa_{\rm Sp} \sim 4 \times 10^{32} \left(\frac{kT}{10\ {\rm keV}}\right)^{5/2} \left(\frac{n}{10^{-3}{\rm cm}^{-3}}\right)^{-1} {\rm cm}^2{\rm s}^{-1}. \tag{4.3}$$

The coefficient has a strong dependence on the temperature and, as a consequence, the conduction rate is slow in the cool core. However, once the cool gas is lifted to large radii and placed in close proximity to hot gas, high temperature and increased temperature gradient both accelerate the thermal conduction rate across the interface. The highly corrugated nature of the interface (cf. Fig. 4.1) further increases conduction compared to a stratified isotropic cluster. High-resolution simulations are critical to resolve this interface.

We then calculate the heat flux by

$$\vec{q} = n k_B f_{\rm Sp} \kappa_{\rm Sp} \nabla T, \tag{4.4}$$

in which $f_{\rm Sp}$ is the fraction relative to the classic Spitzer conduction rate and encapsulates various factors including the orientation of the magnetic fields and the plasma microphysics. Since we do not include magnetic fields in the initial ICM, it is impossible to include anisotropic conduction in this analysis. Instead, we conservatively use $f_{\rm Sp} = 0.1$ and 0.01, which is much lower than the typical 1/3 value used in many studies, and express any findings in terms of $_{\rm Sp}$, the effective conductive coefficient in units of the Spitzer value so that results can readily be understood for a range of assumptions about conductivity. We further exclude regions where the jet mass fraction exceeds 10^{-3} (cf. contours in Fig. 4.1) to avoid counting the heat exchange between the relativistic gas in the hot bubbles and the ICM, which is strongly suppressed. Note that we do not exclude the jet region explicitly in Section 4.3.3, since the selection of the low-entropy gas naturally does not incorporate the hot jet gas.

The instantaneous global heating and cooling rate due to conduction is calculated by taking the divergence of the heat flux. We then add the thermal conduction heating/cooling rates in each radial and entropy bin and compare them with the x-ray cooling rate in the marginal histogram at two different times in Fig. 4.4 and Fig. 4.5. We show two plausible conduction rates at 10% and 1% of the Spitzer value. The heat flux in galaxy clusters is likely far below the nominal Spitzer value, For example, a factor of 100 suppression is consistent with recent results from studies of the plasma physics of conduction (Roberg-Clark et al. 2018a).

One can see that at an earlier time in Fig. 4.4, the conductive heating rate at 10% Spitzer value does not yet overcome the x-ray cooling rate. At 300 Myr in Fig. 4.5, the

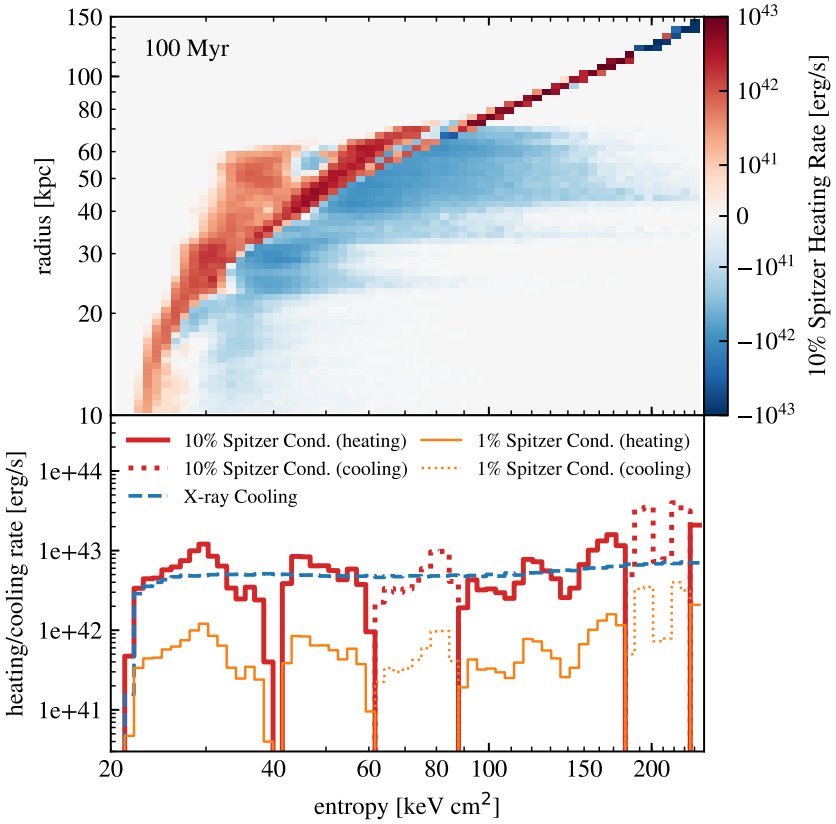

Figure 4.4 : Heating and cooling rate histogram at 100 Myr. The conduction heating and cooling rates are summed in each entropy and radial bins with $f_{\rm Sp} = 0.1$ (*upper panel*). Marginal histogram shows the heating and cooling in entropy bins (*lower panel*). For comparison with the x-ray cooling rate, two conduction rates $f_{\rm Sp} = 0.1$ and 0.01 are plotted. Solid lines indicate heating, while dotted and dashed lines denote cooling. Note that the conductive heat flux occurs primarily around the surface of the uplifted low-entropy gas, while the x-ray cooling happens in all gas. The energy is transferred from the high-entropy gas to low-entropy gas at the same radius and thus the conductive heating and cooling rates as a function of radius have much smaller value. The high-entropy gas that cools at small radii (<60 kpc) is due to the contamination from the hot jet gas.

heating rates can be close to the radiative cooling in some bins even at $f_{\rm Sp} = 0.01$. The heating and cooling rate as a function of radius have much smaller values since most of the Spitzer heat flux happens between the high-entropy and the low-entropy gas at the same radius as shown in the upper panels in Fig. 4.4 and Fig. 4.5. Note that the heating and cooling rates in these figures are cluster-average quantities. While x-ray cooling is a global phenomenon, the conductive heating and cooling happens primarily around the uplifted gas. Thus, the net heating rate locally at the surface of the low-entropy gas is significant even at 1% of the Spitzer rate.

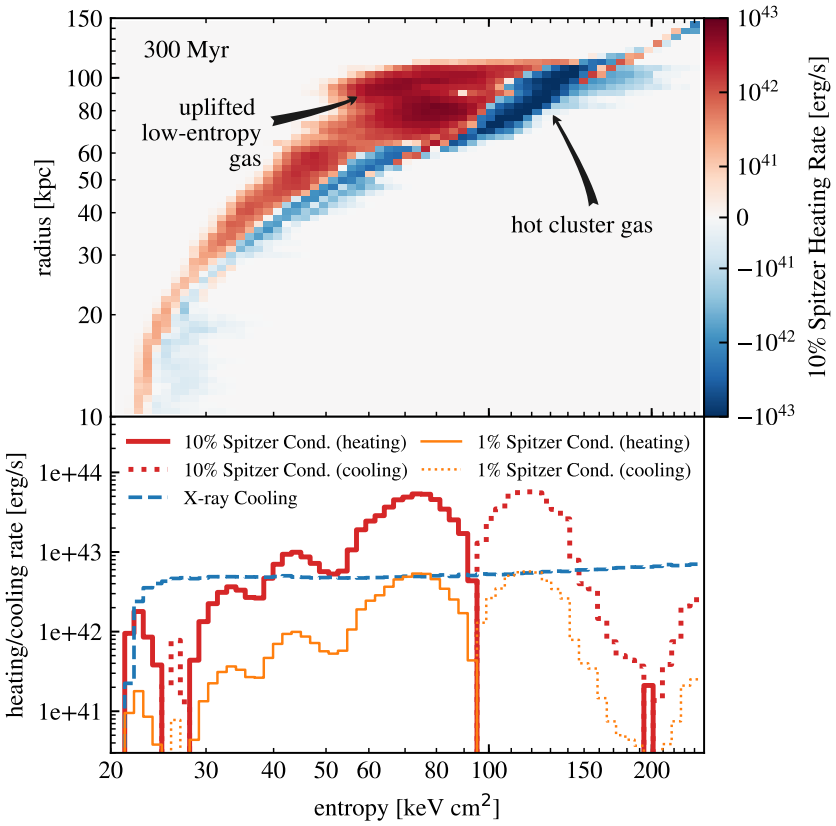

Figure 4.5 : Same as Fig. 4.4 but at 300 Myr. The heating rates are large, especially for the entropy bins between 55 and 95. These are the gas that were originally closer to the core and were brought to larger radii by the rising bubbles.

Although the microphysical details of the conduction deserve investigations in more depth, we find that thermal conduction will be able to bring the low-entropy gas to the temperature of the heat reservoir in a short amount of time. The heating rate increases significantly at later times, which is shown in Fig. 4.6, where we aggregate the net heating rate of the low-entropy gas for 1% Spitzer value and subtract the x-ray cooling rate. Most of the lower-entropy-ratio gas experiences net heating. However, at later times, cooling exceeds heating in the gas with entropy ratio between 0.8 and 0.9, which is indicated by the cumulative heating curve for $x < 0.9$ crossing below the $x < 0.8$ curve after 150 Myr.

We can also estimate the heating timescale $\tau_{\rm heat}$ from the energy budget and the corresponding net heating rate (lower panel of Fig. 4.6). The free-fall time $\tau_{\rm ff}$ at 100 kpc, where most of the low-entropy gas is located at the simulation time of 300 Myr, is about 150 Myr. At 1% of the Spitzer rate, the thermalization timescales are comparable or shorter than the free-fall time. As long as the lifted gas is thermalized before it falls back, the heat pump mechanism will be able to pull more energy than the AGN provided. In the discussion section, we will discuss the conduction rates in more details.

We perform the same calculation on a similar simulation with different jet magnetic field configuration and find the same conclusion. Locally, the conduction rate is slightly different due to different bubble shapes, but globally the energy budget remains much the same within 10%.

4.4 The Maximum Possible Efficiency of the Cluster Heat Pump

In a traditional heat pump, energy is expended on performing mechanical work (compression or decompression) before the heat exchange stage. In geothermal heat pumps, energy is expended to move fluid against gravity. Our case is similar to a geothermal system in that work is done against net gravity.

The low-entropy gas is lifted against the net gravitational force towards the heat reservoir in order for thermal conduction to take place. Due to the buoyancy, lifting the gas from its original location, where the density is the same as the surroundings, requires almost no force. Once the gas is away from its original location, the density drops adiabatically. As long as the density profile of the cluster falls steeper than adiabatic, i.e. the ICM profile is sub-adiabatic, which is always true for convectively stable cool-core clusters, lifting the gas

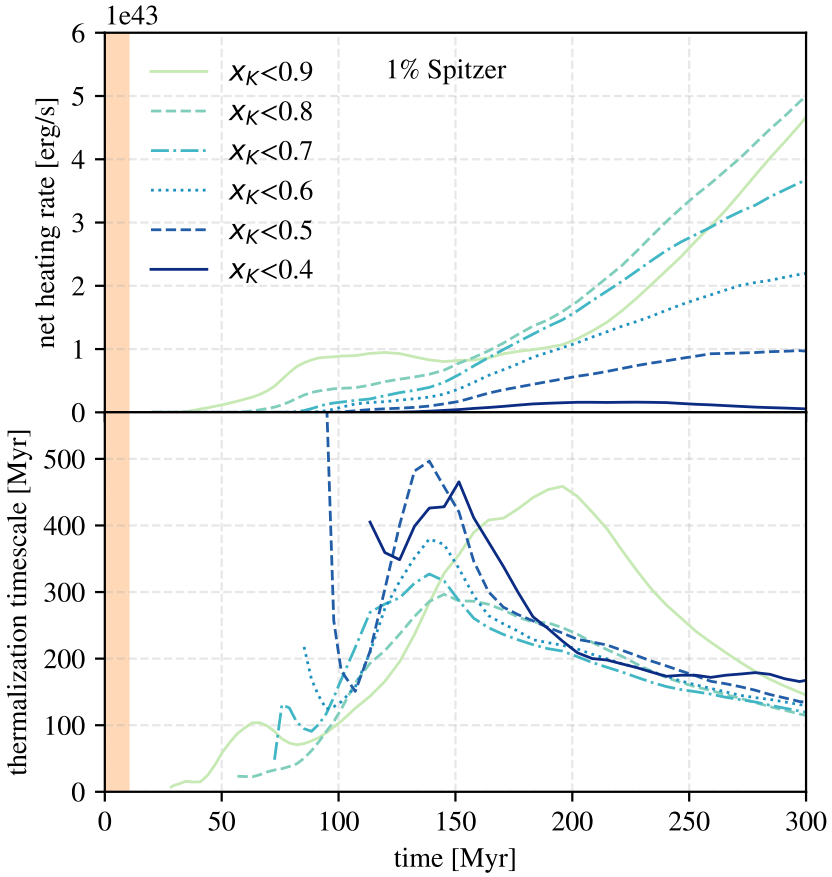

Figure 4.6 : This figure shows the evolution of the aggregated net conductive heating rate at 1% Spitzer value minus the x-ray cooling rate for the low-entropy gas with entropy ratio x_K (*upper panel*), and the average heating timescale $\tau_{\rm heat}$ to thermalize the energy budget of the low-entropy gas (cf. Fig. 4.3) to the surrounding temperature (*lower panel*).

requires work. In this case, the temperature of the lifted gas is lower than the surroundings and allows thermal energy to transfer to the gas through conduction.

Here we consider the limiting efficiency of the heat pump, defined as the ratio between the thermal energy through conduction and the work needed to move the gas to a large radius, in a simplified case. We first consider the generic case where the temperature and density profiles of the ICM follow simple power-laws

$$T(r) = T_0 \left(\frac{r}{R_0}\right)^{\delta}. \quad \rho(r) = \rho_0 \left(\frac{r}{R_0}\right)^{-3\beta}, \tag{4.5}$$

where the index of the density corresponds to β in the β-model outside of the core in Eq. 4.1. When $\delta = 0$, this represents an isothermal atmosphere; for cool-core clusters,

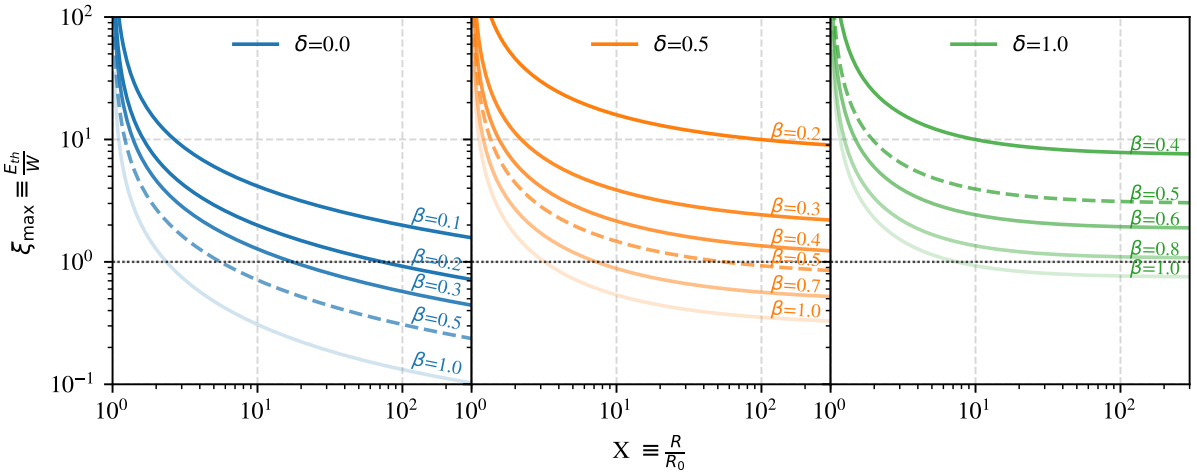

Figure 4.7 : Efficiency for various β and δ (as defined in Eq. 4.5) for monatomic gas. δ=0 corresponds to an isothermal cluster. Note that β must be larger $\delta/3$, otherwise the pressure gradient becomes positive. Dashed lines correspond to $\beta = 0.5$ are most similar to the density profile used in our simulation. The efficiency larger than unity (dotted line) means that more thermal energy is transferred than the work needed to lift the gas. Note that high efficiency does not necessarily mean that the gas can gain a huge amount of thermal energy. See Fig. 4.8 for the energy gain.

$\delta > 0$. The pressure then follows the ideal gas law

$$P(r) = P_0 \left(\frac{r}{R_0} \right)^{-3\beta+\delta}, \tag{4.6}$$

We also assume the ICM is in hydrostatic equilibrium

$$\frac{\mathrm{d}P}{\mathrm{d}r} = -g \cdot \rho, \tag{4.7}$$

which gives us the condition that $-3\beta+\delta < 0$ for negative pressure gradient and the scaling of the gravitational acceleration

$$g(r) = g_0 \left(\frac{r}{R_0} \right)^{\delta-1}. \tag{4.8}$$

In the limiting case of slow lift of a blob of gas, we can neglect the kinetic energy of the blob. When the gas is lifted away from its original location, it will expand to be in

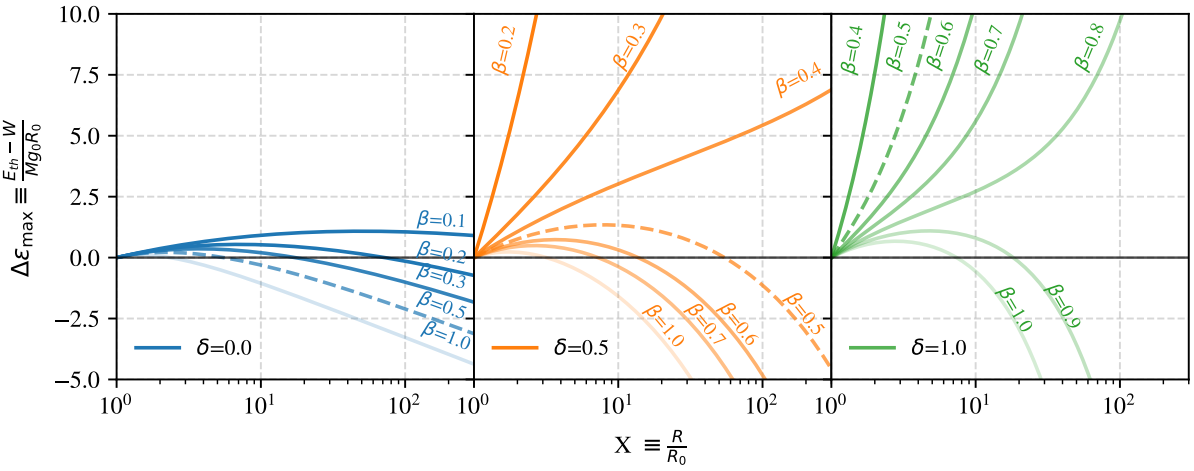

Figure 4.8 : Energy gain for various β and δ for monatomic gas. Dashed lines correspond to $\beta = 0.5$ are most similar to the density profile used in our simulation. For $\beta < 5\delta/6$ the curve diverges to infinity since lifting to larger radii will provide more energy; for $\beta > 5\delta/6$, an optimal lift of X can be found at the peaks of the curves that the heat pump acquires most thermal energy than the expenditure on work for lifting.

pressure balance with the surroundings. The net gravitational force acting on the gas is

$$F_g = -\Delta\rho\ V g = -(\rho_{\rm blob} - \rho(r))V_{\rm blob}\ g(r) \tag{4.9}$$

Assuming the gas expands adiabatically, we have the scaling of the volume

$$V_{\rm ad}(r) = V_0 \left(\frac{P(r)}{P_0}\right)^{-\frac{1}{\gamma}} = V_0 \left(\frac{r}{R_0}\right)^{\frac{3\beta-\delta}{\gamma}} \tag{4.10}$$

and the density

$$\rho_{\rm ad}(r) = \rho_0 \left(\frac{r}{R_0}\right)^{-\frac{3\beta-\delta}{\gamma}}. \tag{4.11}$$

The net gravitational force can then be written as

$$\begin{aligned} F_g(r) &= -\left(\rho_{\rm ad}(r) - \rho(r)\right) V_{\rm ad}(r)\ g(r) \\ &= -Mg_0 \left[\left(\frac{r}{R_0}\right)^{\delta-1} - \left(\frac{r}{R_0}\right)^{-3\beta+\delta-1+\frac{3\beta-1}{\gamma}}\right], \end{aligned} \tag{4.12}$$

where M is the mass of the lifted gas. The work needed to lift the gas from R_0 to R is the integral of the force

$$\begin{aligned} W &= \int_{R_0}^{R} -F_g(r)\,{\rm d}r \\ &= Mg_0R_0 \int_1^X x^{\delta-1}\left(1 - x^{-3\beta+\frac{3\beta-\delta}{\gamma}}\right){\rm d}x, \end{aligned} \tag{4.13}$$

where we changed variables to $x \equiv r/R_0$ and call the lifting radius ratio $X \equiv R/R_0$.

When the gas is lifted, its temperature is lower than the surroundings

$$T_{\rm ad}(x) = T_0 \frac{P(x)}{\rho_{\rm ad}(x)}\frac{\rho_0}{P_0} = T_0\ x^{-3\beta+\delta+\frac{3\beta-\delta}{\gamma}} \tag{4.14}$$

and the thermal energy necessary to themalize the gas when it is lifted to $r = R$ is

$$\begin{aligned} E_{\rm th} &= \frac{1}{\gamma-1}\frac{M}{\mu m_p}k\ (T(X) - T_{\rm ad}(X)) \\ &= \frac{1}{\gamma-1}\frac{M}{\mu m_p}kT_0\left(X^\delta - X^{-3\beta+\delta+\frac{3\beta-\delta}{\gamma}}\right) \\ &= \frac{1}{(3\beta-\delta)(\gamma-1)}Mg_0R_0X^\delta\left(1 - X^{-3\beta+\frac{3\beta-\delta}{\gamma}}\right), \end{aligned} \tag{4.15}$$

where the hydrostatic equilibrium and the ideal gas law imply

$$\frac{kT_0}{\mu m_p} = \frac{g_0 R_0}{3\beta - \delta}. \tag{4.16}$$

The efficiency of the heat pump can then be expressed as

$$\begin{aligned} \xi_{\rm max} &\equiv \frac{E_{\rm th}}{W} \\ &= \frac{1}{(3\beta-\delta)(\gamma-1)} \frac{XF(X)}{\int_1^X F(x)\,{\rm d}x}, \end{aligned} \tag{4.17}$$

where $F(x) \equiv x^{\delta-1}\left(1 - x^{-3\beta+\frac{3\beta-\delta}{\gamma}}\right)$. We plot the efficiency for several cases of δ and β in Fig. 4.7. Note that the efficiency is largest at small X because of the near-zero work needed to lift the gas around its original location. The gravitational energy is invested in lifting the gas upward and will not be recovered if the gas is thermalized before it sinks back. In the case of large lift, i.e. $X \gg 1$, the limiting efficiency becomes

$$\lim_{X\gg 1} \xi_{\rm max} = \frac{\delta}{(3\beta-\delta)(\gamma-1)}. \tag{4.18}$$

For monatomic gas, $\gamma = 5/3$, the limiting efficiency is larger than 100% for large X when

$$\beta < \frac{5}{6}\delta. \tag{4.19}$$

In Fig. 4.7, we can see that the heat pump mechanism operates optimally when the temperature gradient is large (large δ) or when the density gradient is small (small β) such that lifting the gas requires very little work. Although the efficiency is larger at small X, the absolute thermal energy gain is small. We can further consider the energy gain of the mechanism normalized by the initial gravitational energy

$$\begin{aligned} \Delta\epsilon_{\rm max} &\equiv \frac{E_{\rm th} - W}{M g_0 R_0} \\ &= \frac{1}{(3\beta-\delta)(\gamma-1)} XF(X) - \int_1^X F(x)\,{\rm d}x. \end{aligned} \tag{4.20}$$

We show the energy gain for various δ and β in Fig. 4.8. For $\beta < 5\delta/6$, the curves diverge to infinity, i.e. more thermal energy is available for more lift. For $\beta > 5\delta/6$, there is an

optimal lift X that maximize the energy gain. Considering the temperature gradient of the cluster is only positive from the cool core to the hot atmosphere, it is unlikely that this mechanism will get infinite thermal energy from large radial change. Instead, there will be an optimal lift that the energy gain is maximized depending on the profile of the cluster.

Since the AGN expends energy on other aspects not included here (namely, the kinetic and internal energy of the jets/lobes, and kinetic energy of the lifted gas), the true efficiency is $\xi < \xi_{\rm max}$ and the energy gain is $\Delta\epsilon < \Delta\epsilon_{\rm max}$. This method works as long as positive heat exchange is possible, i.e. the temperature gradient being shallower than the adiabatic gradient, $\delta > 3\beta(1-\gamma)$, which is the criterion for convective stability.

For a more realistic background profile like the one used in our simulation of the Perseus cluster (sec Section 4.2), we can integrate the work and calculate the conductive thermal energy numerically, which is shown in Fig. 4.9 for efficiency and Fig. 4.10 for energy gain. Various initial radii are included in the calculation. We can see that a lift of a few tens of kpc, as observed with the simulations, can provide for a high limiting efficiency and a large energy gain. This radius corresponds to the final distance of the bubbles from the cluster center in our simulation, as well as the locations of x-ray bubbles in many observations (Bîrzan et al. 2004; Shin et al. 2016).

In Fig. 4.10, we can see lifting the low-entropy gas can provide up to an additional $\sim$ 3 keV of energy per particle. Thus, moving $10^{10} M_\odot$ can generate additional 10^{59} erg of thermal energy from the heat pump mechanism as we estimate from the simulation in Section 4.3.3.

Now we can find the peak energy gain for different initial radii in Fig. 4.10 and the corresponding change in radius, which is shown in Fig. 4.11. We see that for small initial radius, the peak energy gain is larger and also requires less lifting. For large initial radius, where the temperature profile tends to be isothermal, the $\Delta R_{\rm peak}$ increases linearly, i.e.

constant $X_{\rm peak}$, and the energy gain becomes constant, i.e. constant $g_0 R_0$. Again, we see that the optimal operating range of the heat pump mechanism is to lift the gas from the cool core to the hot atmosphere of the cluster.

For other observed groups and galaxies, the best fit β-model usually gives β in the range between 0.3 and 0.7 (Mulchaey et al. 2003; McCarthy et al. 2004; Dong et al. 2010; O'Sullivan et al. 2017), including the Perseus Cluster modeled in our simulation. Most of their temperature profiles do not follow a simple power law, but increase from the cool core to the outskirts and becomes near isothermal at large radii. Thus, the heat pump operates best across the temperature gradient around the cluster core where the heating is essential for the cluster.

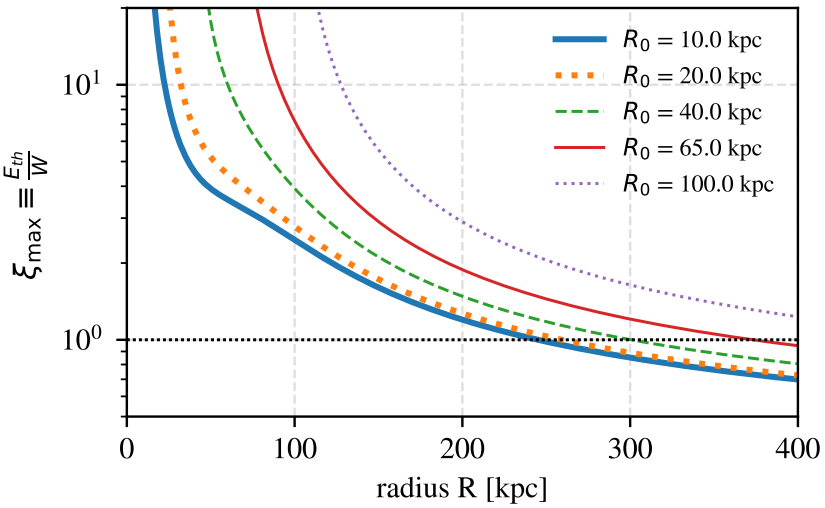

Figure 4.9 : Efficiency for various initial radii R_0 for the ICM profiles used in our simulation that represent the Perseus cluster. Since the temperature tends to isothermal at large radii, the efficiency is not larger than 100% asymptotically. Note that the AGN bubbles rise only up to $\sim$ 100 kpc in our simulation, which falls in the very high efficiency range.

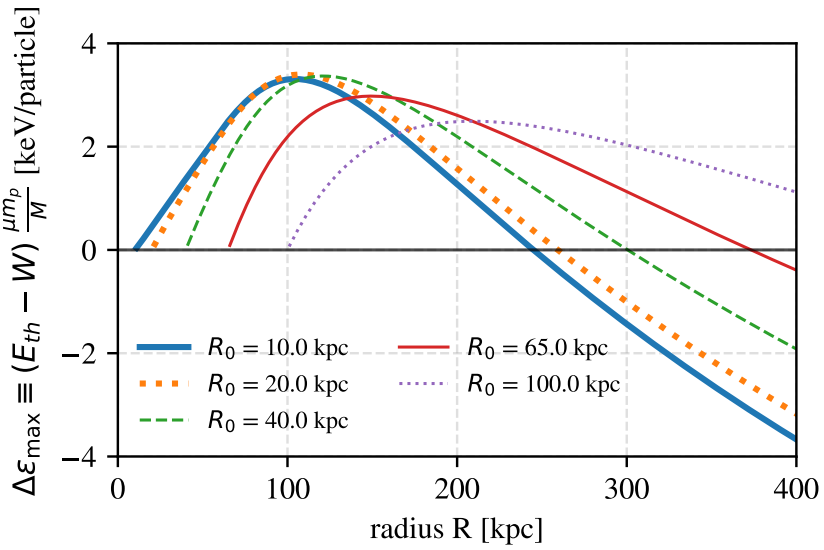

Figure 4.10 : Average energy gain per particle for various initial radii R_0 for the ICM profiles used in our simulation that represent the Perseus cluster. This is the extra thermal energy a particle can get when it is lifted.

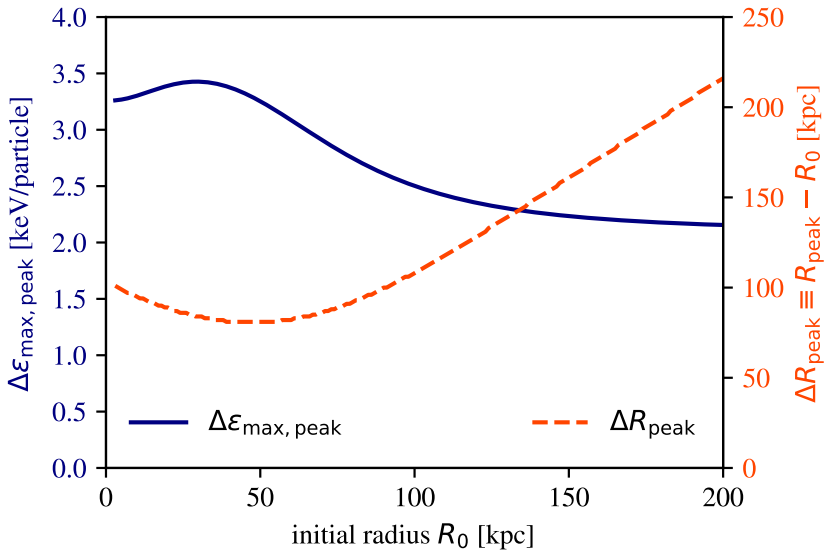

Figure 4.11 : Peak energy gain per particle and the lifting distance needed. This figure shows the peak of the possible energy in Fig. 4.10 and the corresponding change in radius.

4.5 Discussion

4.5.1 The conduction rate and energy budget

In the literature, adiabatic uplift is usually deemed ineffective to offset the cooling because the lifting of gas only decreases the cooling time by a factor of few (see McNamara & Nulsen 2012, for review). However, in our scenario, even though the uplift process is adiabatic, the gas will be heated by the hot atmosphere of the cluster due to the increased conduction coefficient and temperature gradient. The thermalization timescale based on 1% Spitzer value in Fig. 4.6 suggests that the low-entropy gas might not have enough time to be heated during the uplift, but will eventually be heated before sinking. The energy budget estimated from the simulation in Fig. 4.3 provides a rough estimation of the available energy through this mechanism. The actual energy budget depends on various factors, including the conduction rate, the efficiency of lifting, and the cluster profile. We show in this work that this effect can be significant and should not be ignored when analyzing the thermal balance of clusters.

Anisotropic thermal conduction has been widely discussed in the context of galaxy clusters. Kannan et al. (2017) pointed out that anisotropic thermal conduction could enhance the energy coupling between the AGN and the ICM through more effective mixing. In this work, we focus on the additional heating channel between high- and low-entropy cluster gas facilitated by the long-lived rising bubbles, rather than the direct heating from the bubbles themselves.

We caution that the calculation in Section 4.3.4 is likely an overestimate due to the following reasons: (a) Our simulation does not have explicit thermal conduction, and the estimated rate is based on the distribution of the gas without prior heat exchange (except for numerical mixing). Once thermal conduction takes place, the sharp temperature gradient

will quickly smooth out and the rate will drop roughly as $t^{1/2}$. (b) Heat flux might be significantly suppressed by magnetic field geometry and microscopic plasma instabilities in the cluster gas (Roberg-Clark et al. 2016, 2018b). Although we include magnetic fields in the injection of the jets, the ICM is not magnetized in our simulations. Thus, it is impossible to estimate the effect of anisotropic conduction between the low-entropy gas and the hot atmosphere.

However, we argue that these uncertainties do not change our major finding that the heat pump mechanism is able to provide additional energy to the AGN feedback loop. The total energy budget estimated in Section 4.3.3 and the efficiency in Section 4.4 should not change significantly due to the uncertainties in the conduction rate provided that the thermalization can happen before the sinking of the low-entropy gas. As long as the heating timescale is shorter than the free-fall time ($\tau_{\rm heat} < \tau_{\rm ff}$), our mechanism works, which leaves a lot of room even if the conduction coefficient is much smaller than Spitzer. We will leave the investigation of the anisotropic conduction effect and the interplay between the conduction rate and the total energy budget to future work.

Even if the conduction rate at an earlier time is substantial and the gas is thermalized before it reaches the largest radius, the upward motion triggered by the rising bubble can still bring the already thermalized gas to larger radii. Indeed, we show in Section 4.4 that the heat pump operates at very high efficiency around the initial radius (X $\sim$ 1). This is due to the minimal work needed to lift the gas with the same density as the surroundings. Thus, the bubble might be able to bring more gas to large radii if the gas was thermalized before reaching the final location.

The amount of the uplifted low-entropy gas, nevertheless, might change depending on the integrity of the bubble while it rises. Pure hydrodynamic bubbles have been suggested to be quickly disrupted by instabilities (Diehl et al. 2008). Thus, most of the

bubbles associated with x-ray cavities may be supported by magnetic fields or require other mechanisms to suppress the instabilities. Some research suggests that the stability of the bubbles might be affected more by the surrounding magnetic field than by the field inside the bubbles (Ruszkowski et al. 2007; Dursi & Pfrommer 2008). How the amount of lifted low-entropy gas depends on the dynamics of the bubble and the internal or external field, will require further research.

4.5.2 Effect of mixing

Some recent studies identify mixing (between the bubble plasma and the cluster gas) as the primary heating mechanism (Yang & Reynolds 2015; Li et al. 2017). Whether mixing is a major mechanism requires further studies (see Hillel & Soker 2016, 2018). It is important to note, however, that the effect of the thermal conduction is only evident in simulations with high spatial resolution. In resolution-limited simulations, both the hot gas from the bubbles and the low entropy gas lifted in their wake is quickly mixed with the ICM and unrealistic numerical mixing leads to quick dissipation of the bubble and increased heating of low-entropy uplifted gas. The amount of lifted low-entropy gas is likely reduced due to the bubbles being prematurely mixed and dispersed numerically. High resolution is important also because conduction is strongly increased by the corrugated surface of the uplifted gas and turbulence keeps re-arranging the interface between low- and high-temperature gas, regenerating the hot-cold interface and keeping gradients large for large heating rate (see Fig.4.1).

On the other hand, our simulation probably still underestimates the level of turbulent mixing due to numerical viscosity. Such mixing between low-entropy and hot cluster gas, however, would help to bring cold and hot gas into contact and therefore increase the heat transfer rate. This strengthens our argument that the low-entropy gas can be heated before

falling back to the core.

4.5.3 Multiphase filaments

Multiphase filaments in Hα, x-ray, and molecular lines, are often observed in galaxy clusters (see e.g. Fabian et al. 2003; Lim et al. 2012; McNamara et al. 2014). Some observations (Vantyghem et al. 2016; Russell et al. 2016; Vantyghem et al. 2018) and simulations (Revaz et al. 2007; Li & Bryan 2014) suggest that the filaments are formed *in-situ* from the entrained cold gas lifted by the bubbles. Our simulations do not include the formation of the filaments as the entropy reservoir of the uplifted gas in our simulations corresponds to a different ICM phase. The magnetic field in the wake might indeed prevent evaporation by thermal conduction of the Hα filaments (Ruszkowski et al. 2007). However, the existence of the filaments may be suggestive of efficient up-lift. Regardless, there is no way to generally avoid uplift of cold gas by jet-inflated bubbles.

While our results suggest that the conduction rate between the hot atmosphere and the lifted low-entropy gas could be substantial, our simulations do not exclude the formation of the filaments since they involve more physics that were not modeled in our work. The Hα filaments could be a much smaller volume where thermal instability takes place and thus consistent with the stimulated condensation scenario (McNamara et al. 2016). Locally, cooling can become catastrophic in this scenario, as a detailed local balance between heating and cooling is not provided by the heat pump mechanism, which regulates the cluster on a global scale. Rapidly cooling gas clumps will sink to the gravitational center of the cluster, where they are most easily captured by the drag of the rising bubbles.

4.5.4 Implication of the heat pump mechanism

In our simplified simulation, we study the long-term effect of a single AGN outburst. The proper balance between heating and cooling is not the main goal of this work since it is impossible to counteract the cooling of the cluster for 300 Myr with just one episode of AGN activity. It has been a question how the "bursty" AGN events can regulate the constant radiative cooling (Best et al. 2007). The process discussed in this work suggests a solution to this problem by transforming the bursty nature of AGN into a much more gentle heating process. Not only can the AGN heat the ICM during the active phase, but the rising bubbles enable conduction between the hot atmosphere and the uplifted cool gas. It can also help to explain the scatter of the jet power seen in the observations relative to the cluster cooling power since this mechanism does not require a close instantaneous balance between jet power and the cooling rate.

By bringing gas of different entropy into close thermal contact, the AGN essentially acts as a heat pump. The energy used to heat the low-entropy gas is drawn from the thermal base of the outer cluster, not the jet power. In this way, the heating efficiency of AGN can exceed 100%, as slow and subsonic exchange of gas can be done adiabatically. We show that the thermal energy in many cases exceeds the work needed to bring the low-entropy gas to large radii in Section 4.4.

The feedback loop of the heat pump is, like the traditional AGN feedback, governed by the cooling within the cluster core that stimulates the AGN activities. In the short term, other mechanisms may still be required to help counteract the rapid cooling in the core if there were no previous episodes of AGN bubbles. Once the rising bubbles are established, they will be able to remove part of the cooled gas from the core and regulate the cooling in a long timescale and with more energy than injected by the jets itself. This will likely

change the necessary duty cycle to balance the radiative cooling in AGN feedback.

4.6 Conclusions

We consider the idea that AGN jets could act as a "*heat pump*" by inflating buoyant bubbles that lift low-entropy gas from the core into thermal contact with the surrounding hot gas. The increased temperature gradients and conduction coefficient accelerate the thermal exchange between the hot atmosphere and the lifted gas. The AGN in this scenario does not heat the cluster core directly; rather it creates a pipeline which allows the energy exchange between the heat reservoir and the cool core. In this mechanism, the total available energy gained by the cluster core to offset the radiative cooling is not simply limited by the total energy output of the AGN, but also the heat transferred from the hot gas at large radii of the cluster to the uplifted low-entropy gas. Our analysis implies that a 10-Myr active jet could still affect the thermal state of the cluster after 300 Myr. This mechanism has the advantage that bursty AGN activity is transformed into a more gentle and longer-lasting heating process. In this work, we demonstrate that

1. Jet-inflated bubbles can bring a significant amount of low-entropy gas to large radii. The removal of the cool gas from the core is seen mostly in the wake of the rising bubbles. Higher-entropy gas replaces the lifted low-entropy gas. Repeated AGN cycles can thus likely induce sufficient circulation to affect gas not aligned with the jet axis.

2. The energy budget that can be drawn from the heat reservoir to the low-entropy gas is comparable to the energy input from the jet. This energy budget reaches a maximum when the bubbles are already mostly disrupted.

3. The large thermal conduction rate a later times suggests low-entropy gas can be

thermalized before sinking back even at 1% of Spitzer conduction rate. Uncertainties and open questions regarding the nature of thermal transport in the intracluster plasma motivate further work to explore this proposed mechanism.

4. The efficiency of the heat pump, defined as the ratio between the thermal energy transferred and the work needed to lift the low-entropy gas, could be greater than 100% in many cases. Even if the efficiency is not larger than 100% asymptotically, the energy gain will still be positive for moderate lift and will work in concert with any other forms of dissipation of jet energy.

We want to bring attention to the heat exchange between the uplifted gas and the hot atmosphere through this exploratory work inspired by the long-term evolution of our simplified numerical experiment. In addition to heating the core itself, the AGN could act as a facilitator in cool-core systems and exchange energy from the hot atmosphere. To investigate this heat-pump mechanism rigorously, we will need the simulations to include effects like radiative cooling and anisotropic thermal conduction and also consider the integrity of the bubbles. Our preliminary analysis nonetheless indicates that this process can provide another avenue in the already hotly debated cooling flow problem.

YC and SH would like to acknowledge support from NASA through the Astrophysics Theory Program grant NNX17AJ98G. This work used the Extreme Science and Engineering Discovery Environment (XSEDE) Stampede at the Texas Advanced Computing Center at The University of Texas at Austin and the HPC Cluster at the Center for High Throughput Computing at the University of Wisconsin-Madison. Support for this research was provided by the Office of the Vice Chancellor for Research and Graduate Education at the University of Wisconsin-Madison with funding from the Wisconsin Alumni Research Foundation. A part of this work was presented in IAU Symposium 342: "*Perseus in Sicily: from black*

hole to cluster outskirts" and was included in the Proceedings.

References

Best, P. N., Von Der Linden, A., Kauffmann, G., Heckman, T. M., & Kaiser, C. R. 2007, MNRAS, 379, 894

Bîrzan, L., Rafferty, D. A., McNamara, B. R., Wise, M. W., & Nulsen, P. E. J. 2004, ApJ, 607, 800

Churazov, E., Bruggen, M., Kaiser, C. R., Bohringer, H., & Forman, W. 2001, ApJ, 554, 261

Churazov, E., Forman, W., & Jones, C. 2000, A&A, 356, 788

Diehl, S., Li, H., Fryer, C., & Rafferty, D. 2008, ApJ, 687, 173

Dolag, K., Jubelgas, M., Springel, V., Borgani, S., & Rasia, E. 2004, ApJ, 606, L97

Dong, R., Rasmussen, J., & Mulchaey, J. S. 2010, ApJ, 712, 883

Duan, X., & Guo, F. 2018, ApJ, 861, 106

Dubey, A., Antypas, K., Ganapathy, M. K., et al. 2009, Parallel Computing, 35, 512

Dubey, A., Daley, C., Zuhone, J., et al. 2012, ApJS, 201, 27

Dursi, L. J., & Pfrommer, C. 2008, ApJ, 677, 993

Ehlert, K., Weinberger, R., Pfrommer, C., Pakmor, R., & Springel, V. 2018, MNRAS, 481, 2878

Enßlin, T. A., Pfrommer, C., Miniati, F., & Subramanian, K. 2011, A&A, 527, A99

Fabian, A. C. 1994, ARAA, 32, 277

—. 2012, ARAA, 50, 455

Fabian, A. C., Sanders, J. S., Crawford, C. S., et al. 2003, MNRAS, 344, L48

Fabian, A. C., Sanders, J. S., Taylor, G. B., et al. 2006, MNRAS, 366, 417

Fabian, A. C., Walker, S. A., Russell, H. R., et al. 2017, MNRAS, 464, L1

Fabian, A. C., Sanders, J. S., Allen, S. W., et al. 2011, MNRAS, 418, 2154

Forman, W., Jones, C., Churazov, E., et al. 2007, ApJ, 665, 1057

Fryxell, B., Olson, K., Ricker, P., et al. 2000, ApJS, 131, 273

Gendron-Marsolais, M., Kraft, R. P., Bogdan, A., et al. 2017, ApJ, 848, 26

Hardcastle, M. J., Williams, W. L., Best, P. N., et al. 2019, A&A, 622, A12

Heinz, S., Briiggen, M., Young, A., & Levesque, E. 2006, MNRAS, 373, L65

Hillel, S., & Soker, N. 2016, MNRAS, 455, 2139

—. 2018, Research in Astronomy and Astrophysics, 18, 081

Kannan, R., Vogelsberger, M., Pfrommer, C., et al. 2017, ApJ, 837, L18

Lee, D. 2013, Journal of Computational Physics, 243, 269

Li, Y., & Bryan, G. L. 2014, ApJ, 789, 153

Li, Y., Ruszkowski, M., & Bryan, G. L. 2017, ApJ, 847, 106

Lim, J., Ohyama, Y., Chi-Hung, Y., Dinh-V-Trung, & Shiang-Yu, W. 2012, ApJ, 744, 112

McCarthy, I. G., Balogh, M. L., Babul, A., Poole, G. B., & Horner, D. J. 2004, ApJ, 613, 811

McNamara, B., & Nulsen, P. 2007, ARAA, 45, 117

McNamara, B. R., & Nulsen, P. E. J. 2012, New Journal of Physics, 14, 055023

McNamara, B. R., Russell, H. R., Nulsen, P. E. J., et al. 2016, ApJ, 830, 79

—. 2014, ApJ, 785, 44

Morsony, B. J., Heinz, S., Brüggen, M., & Ruszkowski, M. 2010, MNRAS, 407, 1277

Mulchaey, J. S., Davis, D. S., Mushotzky, R. F., & Burstein, D. 2003, ApJS, 145, 39

Narayan, R., & Medvedev, M. V. 2001, ApJ, 562, L129

O'Neill, S. M., & Jones, T. W. 2010, ApJ, 710, 180

O'Sullivan, E., Ponman, T. J., Kolokythas, K., et al. 2017, MNRAS, 472, 1482

Peterson, J. R., & Fabian, A. C. 2006, Physics Reports, 427, 1

Peterson, J. R., Kahn, S. M., Paerels, F. B. S., et al. 2003, ApJ, 590, 207

Pope, E. C. D., Babul, A., Pavlovski, G., Bower, R. G., & Dotter, A. 2010, MNRAS, 406, 2023

Rafferty, D. A., McNamara, B. R., Nulsen, P. E. J., & Wise, M. W. 2006, ApJ, 652, 216

Revaz, Y., Combes, F., & Salomé, P. 2007, A&A, 477, L33

Roberg-Clark, G. T., Drake, J. F., Reynolds, C. S., & Swisdak, M. 2016, ApJ, 830, L9

—. 2018a, Physical Review Letters, 120, 035101

Roberg-Clark, G. T., Drake, J. F., Swisdak, M., & Reynolds, C. S. 2018b, ApJ, 867, 154

Russell, H. R., McNamara, B. R., Fabian, A. C., et al. 2016, MNRAS, 458, 3134

Ruszkowski, M., Enßlin, T. A., Brüggen, M., Heinz, S., & Pfrommer, C. 2007, MNRAS, 378, 662

Scheuer, P. A. G. 1982, In: Extragalactic radio sources; Proceedings of the Symposium, 163

Shin, J., Woo, J.-H., & Mulchaey, J. S. 2016, ApJS, 227, 31

Spitzer, L. 1962, Physics of Fully Ionized Gases, 2nd edn. (Interscience)

Su, Y., Nulsen, P. E. J., Kraft, R. P., et al. 2017, ApJ, 847, 94

Turk, M. J., Smith, B. D., Oishi, J. S., et al. 2010, MNRAS, 423, 3018

Vantyghem, A. N., McNamara, B. R., Russell, H. R., et al. 2016, ApJ, 832, 148

—. 2018, ApJ, 863, 193

Voigt, L. M., & Fabian, A. C. 2004, MNRAS, 347, 1130

Weinberger, R., Ehlert, K., Pfrommer, C., Pakmor, R., & Springel, V. 2017, MNRAS, 470, 4530

Wise, M. W., McNamara, B. R., Nulsen, P. E. J., Houck, J. C., & David, L. P. 2007, ApJ, 659, 1153

Yang, H. Y. K., & Reynolds, C. S. 2015, ApJ, 818, 181

—. 2016, ApJ, 829, arXiv:1605.01725

Zhang, C., Churazov, E., & Schekochihin, A. A. 2018, MNRAS, 478, 4785

Zhuravleva, I., Churazov, E., Schekochihin, A. A., et al. 2014, Nature, 515, 85

Zhuravleva, I., Churazov, E., Arévalo, P., et al. 2015, MNRAS, 450, 4184

Chapter 5

Summary and Conclusions

In this thesis, we use numerical simulations to explore the interaction between the extragalactic jets and their environments.

In Chapter 2, we present a series of high-resolution MHD simulations of AGN jets with different injecting field topology. Pure toroidal, pure poloidal, and helical magnetic fields inside the jets are simulated. We demonstrate that the coexistence of poloidal and toroidal magnetic fields greatly increase the stability of the jets. The toroidal magnetic fields collimate the jet fluid by imposing hoop stress and enable faster propagation of the jet heads. However, the jets are prone to kink instability if only toroidal fields exist. The presence of poloidal fields suppresses the development of kink instability. We find that toroidal and helical jets generate more elongated cocoons and the cavities inflated by the jets are further away from the central engine compared to pure poloidal and hydro jets.

After the jet fluid hits the heavy cluster medium, turbulent motions in the lobes, as well as the precession of the jets, lead to highly tangled magnetic topology in the lobes. No organized large-scale field structures develop in the lobes.

We show a reversal of the spectral index gradient after the jet shuts off due to the reciprocal motions of the young and old plasma in the rotating bubble. We find that the histogram of the polarization position angle can be a good indicator if the magnetic topology of the jet is pure poloidal. The polarization-inferred magnetic fields are more likely to be aligned with the jet-axis in the poloidal case. However, this feature vanishes as the line-of-sight changes toward the jet-axis. We also find that higher frequencies have higher polarization fractions in all cases due to smaller filling factors and thus lower depolarization.

In Chapter 3, we extend the simulations to spam a parameter space of 3 different jet powers and 4 different environments. We discuss the improvement of the techniques to model the cooling of synchrotron emitting plasma by identifying shocks in the numerical

simulation.

We show that the morphology of the radio lobes is affected by the combination of jet powers and environments. The radio emission from the lobes inflated by the jets of the same power appears vastly dissimilar in different environments. For the jets propagating within the dense environments, the radio lobes appear to be more rounded and have large circumference in the equatorial plane. Once the jets advance beyond the uniform-density core, the heads of the lobes expand quickly and the radio lobes appear like classical FR-II sources.

The radio luminosity of jets is empirically measured to be proportional to the jet power. In this study, we reproduce the relationship from simulations and further reveal how this correlation depends on environment and jet active time. The simulation products will be used to verify and improve the current techniques in determination of the ages of the radio galaxies.

Lastly, in Chapter 4, we explore the idea that AGN jets could act as a "*heat pump*" by inflating buoyant bubbles that lift low-entropy gas from the core into thermal contact with the surrounding hot gas. The AGN opens a pipeline to allow the energy exchange between the heat reservoir and the cool core. In this mechanism, the total available energy gained by the cluster core is not limited by the total energy output of the AGN, but also the heat transferred from the hot gas at large radii of the cluster to the uplifted low-entropy gas. Our analysis implies that a 10-Myr active jet could still affect the thermal state of the cluster after 300 Myr. This mechanism has the advantage that bursty AGN activity is transformed into a more gentle and longer-lasting heating process.

The energy budget that can be drawn from the heat reservoir to the low-entropy gas is comparable to the energy input from the jet. This energy budget reaches a maximum when the bubbles are already mostly disrupted. The large thermal conduction rate a later

time suggests low-entropy gas can be thermalized before sinking back even at a conservative 1% of Spitzer conduction rate.

The efficiency of the heat pump could be greater than 100% in many cases. Even if the efficiency is not larger than 100% asymptotically, the energy gain will still be positive for moderate lift and will work in concert with any other forms of dissipation of jet energy.

We hope that this study will motivate further in-depth research on the interaction between AGN and their hosts. Many questions remain to be answered with upcoming facilities of high-resolution and sensitive radio observatories, as well as in the growing efficiency of computing resources. For example, how the magnetic fields in the environments have an effect on the propagation of the jets, the rising bubbles, and the conduction rate between low-entropy and hot cluster gas. The galaxy groups and clusters are usually not in an equilibrium state. How the dynamics of the group and cluster medium affect the AGN jets, and how the jets change the state of the group and cluster medium are worth further investigation.

Appendix A

Derivation of electron transport equation and synchrotron emissivity

A.1 Transport Equation for the Synchrotron Emitting Electrons

Here we summarized the solution of the electron population transport equation, which is based on the work of Bicknell & Melrose (1982); Coleman & Bicknell (1988).

For each numerical ensemble, the electron distribution function $f(\gamma, t)\,\mathrm{d}\gamma$ is the number of electrons with in the energy band $(\gamma, \gamma + \mathrm{d}\gamma)$, where γ is the Lorentz factor and is a proxy for the energy of the electron. The total number densityv is the integration between minimum and maximum energy

$$n(t) = \int_{\gamma_{\min}}^{\gamma_{\max}} f(\gamma, t)\,\mathrm{d}\gamma. \tag{A.1}$$

where $n(t)$ is the number density at the location of the ensemble.

The evolution of the distribution function can be solved by the transport equation. We need to consider the kinetic equation for the electron distribution function. This is a conservation equation for electron numbers in phase space of the form

$$\frac{\partial f}{\partial t} + \nabla_6 \cdot \vec{F} = 0 \tag{A.2}$$

Assuming that our particle distribution is homogenrous and isotropic and consider the equation in the local rest frame of the plasma. Then we can simplify by considering energy instead of momentum and drop all space dependence to write f as a function of time t and particle energy γ only. We restrict this discussion to the ultra-relativistic limit. The total number density n is the integration between minimum and maximum energy

$$n(t) = \int_{\gamma_{\min}}^{\gamma_{\max}} f(\gamma, t)\, \mathrm{d}\gamma. \tag{A.3}$$

The particle flux in real space is $\vec{v}f$. We can write the particle flux in energy space as

$$F_\gamma = \dot{\gamma} f(\gamma, t) \tag{A.4}$$

and the divergence of that flux as

$$\nabla_6 \cdot \vec{F} = (\nabla \cdot \vec{v})\, f + \frac{\partial}{\partial \gamma}\left(\dot{\gamma} f\right) = -\frac{\dot{n}}{n} f + \frac{\partial}{\partial \gamma}\left(\dot{\gamma} f\right) \tag{A.5}$$

where we have used particle number conservation

$$\frac{\partial n}{\partial t} = \dot{n} = -n \nabla \cdot \vec{v} \tag{A.6}$$

The energy change rate can be divided into adiabatic and synchrotron plus inverse-Compton terms.

$$\dot{\gamma} = \dot{\gamma}_{\mathrm{ad}} + \dot{\gamma}_{\mathrm{sync+IC}} \tag{A.7}$$

The adiabatic cooling and heating term corresponding to the expansion and compression can be derived from the first law of thermodynamics

$$\dot{\gamma}_{\mathrm{ad}} = \frac{1}{3} \frac{\gamma}{n} \frac{\mathrm{d}n}{\mathrm{d}t} = \frac{\gamma}{3} \frac{\dot{n}}{n}. \tag{A.8}$$

Assuming efficient scattering of the electrons such that the pitch angle distribution is uniform and average over all pitch angles, the loss of electron energy due to synchrotron

radiation and inverse-Compton scattering can be written as

$$\dot{\gamma}_{\rm sync+IC} = -\frac{4\sigma_T \beta^2 \gamma^2}{3 m_e c}(u_B + u_{\rm rad}), \tag{A.9}$$

where σ_T is the Thomson cross section, $\beta = v/c \simeq 1$, m_e is the mass of the electron, u_B is the energy density of the magnetic fields, and $u_{\rm rad}$ is the energy density of the radiation field. In this work, we assume $u_B \gg u_{\rm rad}$ and ignore the inverse-Compton cooling, which can be justified by the strong magnetic fields in the emitting volume. We have now

$$\dot{\gamma}_{\rm sync+IC} \sim \dot{\gamma}_{\rm sync} = -A\gamma^2, \tag{A.10}$$

in which

$$A = \frac{4\sigma_T}{3 m_e c} u_B \tag{A.11}$$

Now we can write down the kinetic equation

$$\frac{\partial f}{\partial t} - \frac{\dot{n}}{n} f + \frac{\partial}{\partial \gamma}\left(\frac{\gamma}{3}\frac{\dot{n}}{n} f - A\gamma^2 f\right) = 0. \tag{A.12}$$

To simplify and solve this equation, we need to make some substitutions. First, we make a coordinate transformation from (γ, t) to $(\hat{\gamma}, t')$, where

$$\hat{\gamma} \equiv \left(\frac{n_0}{n}\right)^{1/3} \gamma, \quad t' \equiv t, \tag{A.13}$$

$n_0 \equiv n(t_0)$ is the density at some initial time t_0 when the particle distribution is known. Note that $\hat{\gamma}$ and t' are independent variables in phase space.

It is clear that $\hat{\gamma}$ is an adiabatic invariant and the evolution equation for $\hat{\gamma}$ is

$$\frac{{\rm d}\hat{\gamma}}{{\rm d}t} = -\frac{1}{3}\left(\frac{n_0}{n}\right)^{1/3}\frac{\dot{n}}{n}\gamma + \left(\frac{n_0}{n}\right)^{1/3}(\dot{\gamma}_{\rm ad} + \dot{\gamma}_{\rm sync}) \tag{A.14a}$$

$$= \left(\frac{n_0}{n}\right)^{1/3}\dot{\gamma}_{\rm sync} = -\left(\frac{n}{n_0}\right)^{1/3} A\hat{\gamma}^2 \tag{A.14b}$$

which we can readily integrate:

$$\frac{1}{\hat{\gamma}_0} - \frac{1}{\hat{\gamma}} = \int_{t_0}^{t} {\rm d}t' A(t') \left(\frac{n(t')}{n_0}\right)^{1/3} \tag{A.15}$$

or

$$\hat{\gamma} = \frac{\gamma_0}{1 + \gamma_0 \int_{t_0}^{t} \mathrm{d}t' A \left(\frac{n}{n_0}\right)^{1/3}}, \tag{A.16}$$

where we used $\hat{\gamma}_0 = \gamma_0$. Correspondingly, we can relate the lorentz factor γ at some time t to the corresponding lorentz factor at $t = t_0$:

$$\gamma_0 = \left(\frac{n_0}{n}\right)^{1/3} \frac{\gamma}{1 - \gamma \int_{t_0}^{t} \mathrm{d}t' A \left(\frac{n}{n_0}\right)^{1/3}} \tag{A.17}$$

To make the coordinate transformation, we will use

$$\frac{\partial t'}{\partial t} = 1 \tag{A.18}$$

$$\frac{\partial \hat{\gamma}}{\partial \gamma} = \left(\frac{n_0}{n}\right)^{1/3} \tag{A.19}$$

$$\frac{\partial t'}{\partial \gamma} = 0 \tag{A.20}$$

$$\frac{\partial \hat{\gamma}}{\partial t} = -\frac{\gamma}{3}\left(\frac{n_0}{n}\right)^{1/3} \frac{\dot{n}}{n} = -\frac{\hat{\gamma}}{3}\frac{\dot{n}}{n} \tag{A.21}$$

and the chain rule

$$\frac{\partial}{\partial t} = \frac{\partial t'}{\partial t}\frac{\partial}{\partial t'} + \frac{\partial \hat{\gamma}}{\partial t}\frac{\partial}{\partial \hat{\gamma}} = \frac{\partial}{\partial t'} - \frac{\hat{\gamma}}{3}\frac{\dot{n}}{n}\frac{\partial}{\partial \hat{\gamma}} \tag{A.22}$$

$$\frac{\partial}{\partial \gamma} = \frac{\partial \hat{\gamma}}{\partial \gamma}\frac{\partial}{\partial \hat{\gamma}} + \frac{\partial t'}{\partial \gamma}\frac{\partial}{\partial t'} = \left(\frac{n_0}{n}\right)^{1/3}\frac{\partial}{\partial \hat{\gamma}} \tag{A.23}$$

Applying the coordinate transformation to Eq. A.12, we have

$$\begin{aligned} &\frac{\partial f}{\partial t'} - \frac{\hat{\gamma}}{3}\frac{\dot{n}}{n}\frac{\partial f}{\partial \hat{\gamma}} - \frac{\dot{n}}{n}f + \left(\frac{n_0}{n}\right)^{1/3}\frac{\partial}{\partial \hat{\gamma}}\left[\frac{\gamma}{3}\frac{\dot{n}}{n}f - A\left(\frac{n}{n_0}\right)^{2/3}\hat{\gamma}^2 f\right] \\ =&\frac{\partial f}{\partial t'} - \frac{2}{3}\frac{\dot{n}}{n}f - A\left(\frac{n}{n_0}\right)^{1/3}\frac{\partial(\hat{\gamma}^2 f)}{\partial \hat{\gamma}} = 0. \end{aligned} \tag{A.24}$$

We further substitute

$$\tilde{f} \equiv \left(\frac{n_0}{n}\right)^{2/3} f \tag{A.25}$$

to eliminate the second term from the equation

$$\begin{aligned} \frac{\partial f}{\partial t'} - \frac{2}{3}\frac{\dot{n}}{n}f =& \frac{\partial}{\partial t'}\left[\left(\frac{n}{n_0}\right)^{2/3}\tilde{f}\right] - \frac{2}{3}\frac{\dot{n}}{n}\left(\frac{n}{n_0}\right)^{2/3}\tilde{f} \\ =& \left(\frac{n}{n_0}\right)^{2/3}\frac{\partial \tilde{f}}{\partial t'}. \end{aligned} \tag{A.26}$$

The transport equation is now

$$\left(\frac{n}{n_0}\right)^{2/3}\left[\frac{\partial\tilde{f}}{\partial t'}-A\left(\frac{n}{n_0}\right)^{1/3}\frac{\partial(\hat{\gamma}^2\tilde{f})}{\partial\hat{\gamma}}\right]=0. \tag{A.27}$$

Multiplying by $\hat{\gamma}^2\left(\frac{n_0}{n}\right)^{2/3}$, we finally arrive at

$$\begin{aligned}&\frac{\partial(\hat{\gamma}^2\tilde{f})}{\partial t'}-A\left(\frac{n}{n_0}\right)^{1/3}\hat{\gamma}^2\frac{\partial(\hat{\gamma}^2\tilde{f})}{\partial\hat{\gamma}}\\ =&\frac{\partial(\hat{\gamma}^2\tilde{f})}{\partial t'}-\frac{\mathrm{d}\hat{\gamma}}{\mathrm{d}t'}\frac{\partial(\hat{\gamma}^2\tilde{f})}{\partial\hat{\gamma}}\\ =&\frac{\mathrm{d}}{\mathrm{d}t}(\hat{\gamma}^2\tilde{f})=0.\end{aligned} \tag{A.28}$$

That is, the function $\hat{\gamma}^2\tilde{f}$ is constant along the characteristic given by $\hat{\gamma}(\gamma_0,t)$ in Eq. (A.16).

We can thus write the evolution of the distribution function as

$$f(\gamma,t)=\left[\frac{n(t)}{n_0}\right]^{2/3}\frac{\gamma_0^2}{[\hat{\gamma}(t)]^2}f(\gamma_0(\hat{\gamma}(t)) \tag{A.29}$$

where we used $\hat{\gamma}_0=\gamma_0$ and the definitions of $\hat{\gamma}$ and $\tilde{f}$.

Suppose we want to model the evolution of a powerlaw of relativistic electrons injected at a shock. Equation (A.29) allows us to describe how the function evolves: The highest energy electrons will cool the fastest, generating a sharp cutoff at Lorentz factor

$$\gamma_{\mathrm{cut}}=\left(\frac{n}{n_0}\right)^{1/3}\frac{\gamma_0}{1+\gamma_0\frac{4\sigma_{\mathrm{T}}}{3m_{\mathrm{T}}c}\int_{t_0}^{t}dt'u_{\mathrm{B}}\left(\frac{n}{n_0}\right)^{1/3}} \tag{A.30}$$

with

$$\lim_{\gamma_0\to\infty}\gamma_{\mathrm{cut}}=\left(\frac{n}{n_0}\right)^{1/3}\frac{1}{\frac{4\sigma_{\mathrm{T}}}{3m_{\mathrm{e}}c}\int_{t_0}^{t}dt'u_{\mathrm{B}}\left(\frac{n}{n_0}\right)^{1/3}} \tag{A.31}$$

$$\propto\left(B^2\delta t\right)^{-1} \tag{A.32}$$

Generally, a powerlaw spectrum extending to large γ will develop a cut off at high energies. At low energies, the spectrum will change little, because the particles cool very little. The shape near the cutoff will depend on the slope of the powerlaw.

We can see that there is a special case for $\tilde{f} \propto \hat{\gamma}^p$ and $p = -2$, in which case the shape of the powerlaw is invariant, since the factor $\hat{\gamma}^2$ cancels out the factor of $\hat{\gamma}^{-2}$ in f. The spectrum will have a sharp cutoff at $\gamma_{\rm cut}$. For steeper powerlaws, the cutoff will develop a round convex shape, while for shallower $p > -2$, it will develop a bump.

A.2 Synchrotron Emissivity

We follow the calculation of synchrotron emissivity in Rybicki & Lightman (1979) and Longair (2011), from which the important steps are summarized here. For a single electron in magnetic field B, the power emitted through synchrotron radiation perpendicular and parallel to the magnetic field per frequency are

$$p_\perp(\nu) = \frac{\sqrt{3}e^3 B \sin\alpha}{2c^2 m_e}\left[F(x) + G(x)\right], \tag{A.33}$$

$$p_\parallel(\nu) = \frac{\sqrt{3}e^3 B \sin\alpha}{2c^2 m_e}\left[F(x) - G(x)\right], \tag{A.34}$$

where α is the pitch angle of the electron relative to the magnetic field,

$$F(x) \equiv x \int_x^\infty K_{\frac{5}{3}}(\xi)\,\mathrm{d}\xi \tag{A.35a}$$

$$G(x) \equiv x\, K_{\frac{2}{3}}(x), \tag{A.35b}$$

in which K_a is the modified Bessel function of the second kind of order a and

$$x \equiv \frac{\nu}{\nu_c(\gamma)}. \tag{A.36}$$

ν_c is the characteristic frequency which can be written as

$$\nu_c(\gamma) = \frac{3\gamma^2 eB\sin\alpha}{4\pi m_e c}. \tag{A.37}$$

The total power emitted by an electron is

$$p_{\rm tot}(\nu) = p_\perp + p_\parallel = \frac{\sqrt{3}e^3 B\sin\alpha}{c^2 m_e} F(x). \tag{A.38}$$

This is the total energy emitted per time per frequency by the electron with pitch angle α. The radiation is concentrated in a small solid angle ring $\Delta\Omega = 2\pi \sin\alpha\, \Delta\alpha$. The average intensity (energy per time per frequency per solid angle) of this electron can be calculated by

$$j(\nu) = \frac{p_{\rm tot}(\nu)}{\Delta\Omega} = \frac{p_{\rm tot}(\nu)}{2\pi \sin\alpha\, \Delta\alpha}. \tag{A.39}$$

To get the total emissivity, we need to integrate over all electrons. We assume the electrons have a power-law energy distribution

$$N(\gamma)\, {\rm d}\gamma = N_0 \gamma^{-2}\, {\rm d}\gamma. \tag{A.40}$$

When the angle between the magnetic fields and the observer's line-of-sight is α, we consider only the electrons with pitch angle α since the observer only sees the radiation from those electrons. Assuming uniform distribution of the moving direction, the number density of the electrons moving at pitch angle α is

$$\begin{aligned} N(\gamma, \alpha)\, {\rm d}\gamma \Delta\alpha &= \frac{1}{4\pi} 2\pi \sin\alpha\, N_0 \gamma^{-2}\, {\rm d}\gamma \Delta\alpha \\ &= \frac{1}{2} \sin\alpha\, N_0 \gamma^{-2}\, {\rm d}\gamma \Delta\alpha. \end{aligned} \tag{A.41}$$

The total emissivity of a cell is

$$\begin{aligned} J(\nu, \alpha) &= \int_{\gamma_{\rm min}}^{\gamma_{\rm max}} j(\nu) N(\gamma, \alpha)\, {\rm d}\gamma \\ &= \frac{N_0}{4\pi} \int_{\gamma_{\rm min}}^{\gamma_{\rm max}} p(\nu) \gamma^{-2}\, {\rm d}\gamma. \end{aligned} \tag{A.42}$$

By substituting $p(\nu)$ in Equation A.38 and changing variable from γ to x (Equation A.36 and A.37), we have

$$J(\nu, \alpha) = \frac{3(B\sin\alpha)^{\frac{3}{2}} e^{\frac{7}{2}} N_0}{8\sqrt{\pi} c^{\frac{5}{2}} m_e^{\frac{3}{2}}} \nu^{-\frac{1}{2}} \cdot \int_{x_{\rm min}}^{x_{\rm max}} x^{-\frac{1}{2}} 2F(x)\, {\rm d}x. \tag{A.43}$$

Note that

$$x_{\rm max} = \frac{\nu}{\nu_c(\gamma_{\rm min})} \quad \text{and} \quad x_{\rm min} = \frac{\nu}{\nu_c(\gamma_{\rm max})}.$$

We approximate the integral by an exponential function, assuming $\nu_c(\gamma_{\min}) \ll \nu$ such that $x_{\max} \to \infty$

$$\int_{x_{\min}}^{\infty} x^{-\frac{1}{2}} 2F(x)\,\mathrm{d}x \approx C_0 e^{-x_{\min}} = C_0 e^{-\frac{\nu}{\nu_c(\gamma_{\max})}}, \tag{A.44}$$

where $C_0 = 2 \cdot \frac{2^{\mu+1}}{\mu+2}\Gamma(\frac{\mu}{2}+\frac{7}{3})\Gamma(\frac{\mu}{2}+\frac{2}{3}) \approx 4.1648$ for $\mu = -\frac{1}{2}$. The normalization of the electron number density N_0 is estimated by the `pressure` variable in the MHD simulation. We assume that the pressure of the radio lobes comes primarily from the relativistic electrons.

$$\begin{aligned} P = \frac{1}{3}u &= \frac{1}{3}\int_{\gamma_{\min}}^{\gamma_{\max}} N(\gamma)\gamma m_e c^2\,\mathrm{d}\gamma \\ &= \frac{N_0 m_e c^2}{3}\int_{\gamma_{\min}}^{\gamma_{\max}} \gamma^{-1}\,\mathrm{d}\gamma \\ &= \frac{1}{3}N_0 m_e c^2 \ln(\frac{\gamma_{\max}}{\gamma_{\min}}) \end{aligned} \tag{A.45}$$

Here we assume $\gamma_{\min} \approx 10$. We can then express N_0 in terms of pressure

$$N_0 = \frac{3P}{m_e c^2 \ln(\frac{\gamma_{\max}}{\gamma_{\min}})} \tag{A.46}$$

Putting Equation A.44 and A.46 into Equation A.43, we have

$$\begin{aligned} J(\nu,\alpha) = P(B\sin\alpha)^{\frac{3}{2}} \\ \cdot \left[\frac{10e^{\frac{7}{2}}C_0}{8\sqrt{\pi}c^{\frac{9}{2}}m_e^{\frac{5}{2}}\ln(\frac{\gamma_{\max}}{\gamma_{\min}})}\nu^{-\frac{1}{2}}e^{\left(-\frac{\nu}{\nu_c(\gamma_{\max})}\right)}\right]. \end{aligned} \tag{A.47}$$

Similarly, we can calculate the polarized emission from a single electron

$$p_{\mathrm{pol}}(\nu) = p_\perp - p_\parallel = \frac{\sqrt{3}e^3 B\sin\alpha}{c^2 m_e}G(x). \tag{A.48}$$

The ratio between the polarized and the total emission for electrons with a power-law energy distribution can be shown as

$$\Pi = \frac{\int \gamma^{-p} p_{\mathrm{pol}}(\nu)\,\mathrm{d}\gamma}{\int \gamma^{-p} p_{\mathrm{tot}}(\nu)\,\mathrm{d}\gamma} = \frac{p+1}{p+\frac{7}{3}}. \tag{A.49}$$

Using this fraction, the Stokes q and u emissivity in each cell can bew written as

$$q(\nu, \alpha) = -J(\nu, \alpha)\, \Pi \cdot \cos(2\theta) \tag{A.50a}$$

$$u(\nu, \alpha) = -J(\nu, \alpha)\, \Pi \cdot \sin(2\theta), \tag{A.50b}$$

where θ is the angle between the magnetic fields and the horizontal axis of the observation. The minus sign accounts for that the emission perpendicular to the magnetic field is larger than the parallel component. Thus, the major axis of the polarization ellipse is shifted by 90° from the magnetic field. The observed Stokes Q and U are then the integration along the line-of-sight

$$Q(\nu, \alpha) = \int q(\nu, \alpha)\, \mathrm{d}l \tag{A.51a}$$

$$U(\nu, \alpha) = \int u(\nu, \alpha)\, \mathrm{d}l. \tag{A.51b}$$

References

Bicknell, G. V., & Melrose, D. B. 1982, ApJ, 262, 511

Coleman, C. S., & Bicknell, G. V. 1988, MNRAS, 230, 497

Longair, M. S. 2011, High Energy Astrophysics, 3rd edn. (Cambridge, UK: Cambridge University Press)

Rybicki, G. B., & Lightman, A. P. 1979, Radiative Processes in Astrophysics (Weinheim, Germany: Wiley-VCH)